DOI: 10.1515/sspjce-2019-0013

Comparing various influences on adhesive contact with friction

Roman Vodička

Technical University of Košice
Civil Engineering Faculty, Institute of Construction Technology and Management
e-mail: roman.vodicka@tuke.sk

Abstract

A general computational model covering many types of frictional contact interfaces between visco-elastic bodies is considered for some cases physically relevant in numerical analysis of contact in civil engineering structures. The relations between mechanical quantities and internal parameters of the model are illustrated in a couple of simplified examples including cohesive contact combined with Coulomb friction and/or interface plasticity. The computations are implemented a semi-implicit time discretisation, quadratic programming algorithms, and the boundary-element method.

Key words: interface crack, interface damage, interface plasticity, Coulomb friction

1 Introduction

Problems of contact form a very important and well-developed part of solid mechanics. They have been intensively studied for several decades from various aspects: analytical, computational, or modelling. There is also a huge number of engineering structures which should be considered as contact problems. Therefore, analysing such structures and proposing sustainable computational models for them seems to be of a high significance.

We focus on those models which together with contact incorporate adhesion (or cohesion) and friction in the interface. Such models are motivated by theory of damage, sometimes combined with plasticity [1][2]. The roles of pertinent internal variables are replaced by interface damage variable and interface plastic slip. For contact problems, there were developed various approaches to cope with such phenomena [3][4][5][6][7][8][9], including those of the present author [9][11][12][13].

All the phenomena as interface damage, plastic slip or friction (and others) can be considered in a computational model, see [14], in distinct ways. First, the interface damage parameter controlling the stiffness of the adhesive in a contact zone, provoking after its degradation an interface crack, may guarantee various stress-strain diagrams in a sense of cohesive zone models (CZM) [11][13]. Then, if the plastic slip is considered, a double response of the interface after leaving an elastic regime is possible: either the plastic slip starts evolving first and only

afterwards damage occurs, e.g. because of increasing stress due to hardening, or first damage occurs and only afterwards the plastic slip evolves due to decrease of the yield stress because of damage [8][15][16]. Naturally, both options can be combined, too. Friction is conventionally implemented through the Coulomb friction coefficient, which additionally may be damage dependent [7][14]. Nevertheless, if tangential displacement gap is proportional to the plastic slip then friction may be introduced by the activation threshold for its evolving. To distinguish delamination and interface cracks in opening or shearing modes, there may also be two possibilities: either by the plastic slip as in [8][9][16] or by setting fracture energy to depend on interface displacement gap as in [11][13][17][18].

The general model covering all described options is outlined in Section 2. Some aspects of the numerical analysis are sketched in Section 2.2. Finally, a simplified structure with an adhesive interface is introduced in Section 4 and presents modifications of the proposed general model and its basic mechanical relations. The computations are implemented by a MATLAB code.

2 A model of interface failure

Let us consider an elastic body defined by a (planar) domain $\Omega \subset \mathrm{R}^2$ with a bounded Lipschitz boundary Γ. Let $\mathbf{n}$ denote the unit outward normal vector defined at the smooth part of Γ. A split into two non-overlapping subdomains Ω^A and Ω^B whose respective boundaries are Γ^η $\eta = A, B$ will be considered hereinafter for the sake of simplicity, is shown in Figure 1.

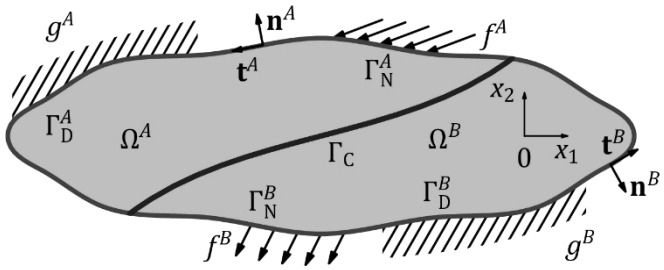

Figure 1: Model for adhesive contact with friction between two subdomains.

The common part of both boundaries, called interface, is denoted Γ_{c}. The boundary conditions can be prescribed either by displacements $u^\eta = g^\eta$ on a part of the outer boundary Γ_{D}^η, or by boundary forces, by giving tractions $p^\eta = f^\eta$ on the other part of boundary denoted Γ_{N}^η.

The interface Γ_{c} is represented by a (negligibly) thin adhesive layer which, however, has its own normal and tangential elastic stiffnesses κ_n and κ_t, respectively. It is considered that a crack can appear along the interface Γ_{c}. During this process, the layer of adhesive is damaged, which is modelled by a scalar damage variable ζ varying between one and zero: values one and zero, respectively, correspond to undamaged and fully damaged adhesive, meant as an interface crack. Additionally, a plastic tangential slip variable π is considered along the interface, which may distinguish opening mode and shearing mode for arising cracks in view of additional energy dissipated in shearing mode. Similarly, friction may take part in shearing cracks as the separated surfaces of the interface may slide on each other. Naturally, this process also dissipates some energy.

2.1 Governing relations

The governing relations for the model are expressed in terms of energy. The energy state includes the free energy represented here by the elastic stored energy E of the domain and of the interface which may be considered as follows:

$$E(\tau;u,\pi,\zeta)=\int_{\Omega}\frac{1}{2}Ce(u):e(u)\mathrm{d}x+\int_{\Gamma_c}\frac{1}{2}\kappa(\zeta)[\![u]\!]^2+\frac{1}{2}\kappa_{\mathrm{g}}([\![u]\!]_n^-)^2+\frac{1}{2}\kappa_{\mathrm{H}}\pi^2\mathrm{d}s \qquad (1)$$

for an admissible displacement field u, in the sense that it satisfies the displacement boundary conditions on Γ_{D}, and admissible damage parameter ζ, i.e. with values lying in the interval $[0,1]$. Otherwise, it is considered that the value of E is infinite and thus unreachable. The introduced parameters include stiffness matrix C of the bulk material, damage dependent stiffness κ of the adhesive layer and the compressive stiffness κ_{g} to replace standard Signiorini contact condition of non-overlapping of the contacting bodies by a normal stiffness penalisation energy term.

Next, if there are some external forces, their energy should be added to the system, too. In Figure 1 we considered forces applied at the boundary Γ_{N}, their energy includes the functional

$$F(\tau;u)=-\int_{\Gamma_{\mathrm{N}}}f(\tau)\cdot u\,\mathrm{d}s. \qquad (2)$$

Finally, the described non-linear processes cause some energy to be dissipated from the structure. It can be expressed by the following form of a pseudo-functional of dissipative forces:

$$R\left(u,\zeta;\dot{u},\dot{\pi},\dot{\zeta}\right)=\int_{\Omega}\frac{1}{2}De(\dot{u}):e(\dot{u})\mathrm{d}x+\int_{\Gamma_c}G\left(\dot{\zeta}\right)+\sigma_{\mathrm{y}}(\zeta)|\dot{\pi}|+\mu(\zeta)\kappa_{\mathrm{g}}|[\![u]\!]_n^-||[\![\dot{u}]\!]_t|\mathrm{d}s. \qquad (3)$$

The functional includes energy dissipated due to a new crack appearance expressed by the term G, then energy dissipated due to plastic slip evolution, which includes a damage dependent yield stress σ_{y}, and the last interface term expresses dissipation due to frictional forces, containing damage dependent friction coefficient μ. The normal stress of the Coulomb friction model is expressed in terms of normal compressive stiffness correspondingly to the term appearing in the elastic energy in Eq. (1). For regularising the friction in the numerical solution and for making model more general, dissipation due to viscosity of the domain material is considered, too, using a simple Kelvin-Voigt model which includes tensor of viscous parameters D. It is also necessary to guarantee a unidirectional character of the process. This can be expressed by setting the potential R to infinity, provided that the conditions $\dot{\zeta}\leq 0$, is not satisfied.

The relations which govern the state evolution can be written in a form of nonlinear variational inclusions with initial conditions (corresponding to an undamaged state)

$$\begin{aligned}\partial_u E(\tau;u,\pi,\zeta)+\partial_{\dot{u}} R\left(u,\zeta;\dot{u},\dot{\pi},\dot{\zeta}\right)+\partial_u F(\tau;u)\ni 0, \quad & u|_{\tau=0}=u_0,\\ \partial_\pi E(\tau;u,\pi,\zeta)+\partial_{\dot{\pi}} R\left(u,\zeta;\dot{u},\dot{\pi},\dot{\zeta}\right)\ni 0, \quad & \pi|_{\tau=0}=\pi_0,\\ \partial_\zeta E(\tau;u,\pi,\zeta)+\partial_{\dot{\zeta}} R\left(u,\zeta;\dot{u},\dot{\pi},\dot{\zeta}\right)\ni 0, \quad & \zeta|_{\tau=0}=1,\end{aligned} \tag{4}$$

where ∂ generally denotes a partial subdifferential as the functionals does not have to be smooth, e.g. R may jump from zero to infinity. For smooth functionals, subdifferentials can be replaced by Gateaux differentials and the inclusions by equations.

2.2 Notes on the numerical implementation of the model

Both, a time stepping algorithm and a spatial discretisation are required for the numerical solution of Eq. (3). The latter is implemented by a standard symmetric Galerkin boundary element approach using linear elements as described e.g. in [19][20] and will not be discussed here. It requires, however, a special treatment of viscosity for the boundary elements to be used as in the purely elastic state. The details can be found in [21].

The time discretisation by a staggered scheme, relies on separately quadratic character of the proposed energy functional Eq. (1) with respect to deformation variables (including the plastic slip), and the damage variable. Such a separating of variables then guarantees a variational character of the solved problem.

For the solution, we choose a fixed time step $\Delta\tau$ for a fixed time range $[0,T]$ such that the solution is obtained at the instants $t^k=k\Delta\tau$ for $k=1,2,\dots T/\Delta\tau$ and is denoted u^k for displacements, π^k for the plastic slip, and ζ^k for the damage variable. In order to obtain the staggered numerical scheme from Eq. (3), the derivatives in the rate variables are approximated by the finite differences e.g. $\dot{\pi}\approx\frac{\pi^k-\pi^{k-1}}{\Delta\tau}$ – the differentiation with respect to the rate is accordingly replaced by differentiation with respect to π^k. Such replacements provide Eq. (3) in the following form:

$$\begin{aligned}\partial_{u^k} E(\tau^k;u^k,\pi^k,\zeta^{k-1})+\Delta\tau\partial_{u^k} R\left(u^{k-1},\zeta^{k-1};\tfrac{u^k-u^{k-1}}{\Delta\tau},0,0\right)+\partial_u F(\tau^k;u^k)\ni 0,\\ \partial_{\pi^k} E(\tau^k;u^k,\pi^k,\zeta^{k-1})+\Delta\tau\partial_{\pi^k} R\left(u^{k-1},\zeta^{k-1};0,\tfrac{\pi^k-\pi^{k-1}}{\Delta\tau},0\right)\ni 0,\\ \partial_{\zeta^k} E(\tau^k;u^k,\pi^k,\zeta^k)+\Delta\tau\partial_{\zeta^k} R\left(u^{k-1},\zeta^{k-1};0,0,\tfrac{\zeta^k-\zeta^{k-1}}{\Delta\tau}\right)\ni 0,\end{aligned} \tag{5}$$

with initial conditions: $u^0=u_0$, $\pi^0=\pi_0$, $\zeta^0=1$.

The separation of variables in the staggered algorithm then provides two minimisations at each time step: the first one with respect to the displacements and plastic slip of the functional

$$H_1^k(u,\pi)=E(\tau^k;u,\pi,\zeta^{k-1})+\Delta\tau R\left(u^{k-1},\zeta^{k-1};\tfrac{u-u^{k-1}}{\Delta\tau},\tfrac{\pi-\pi^{k-1}}{\Delta\tau},0\right)+F(\tau^k,u) \tag{6}$$

renders (u^k,π^k) as its minimiser (the constraint for u is hidden in the definition of E), and the second minimisation with the constraint $0\le\zeta\le\zeta^{k-1}$ (the lower bound is hidden in the definition of E, the upper bound comes from R) of the functional

$$H_2^k(\zeta) = E(\tau^k; u^k, \pi^k, \zeta) + \Delta\tau R\left(0{,}0; 0{,}0, \frac{\zeta - \zeta^{k-1}}{\Delta\tau}\right) \tag{7}$$

provides ζ^k as the constrained minimiser. These two minimisations are solved repeatedly for $k = 1,2, \ldots T/\Delta\tau$. If both functionals are quadratic, a quadratic programming algorithm can be used in the numerical solution, see e.g. [22], otherwise the quadratic programming algorithm can be used sequentially [23].

3 An example

As it has already been mentioned, the model can be used in several ways. We try to present those relevant in engineering analysis of structures with interfaces. In what follows, the example presents a basic geometry consisting of two squares as shown in Figure 2. Both blocks are made of the same homogeneous isotropic material with Young's modulus $E = 200$ GPa and Poisson's ratio $\nu = 0.3$. As shown by the boundary conditions, the left domain is fixed along its left face and the right face of the right domain is exposed to the prescribed displacements field whose time constant normal component is equal to $g_n = -0.143$ mm (causing the pressure state so that the blocks remain touching each other), while the tangential displacement is applied at a constant velocity so that $g_t(\tau) = v\tau$, with $v = 1$ mm/s.

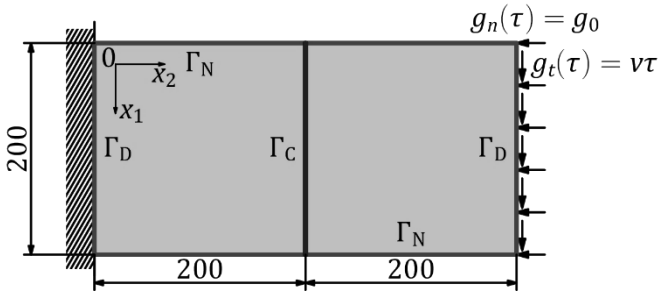

Figure 2: Geometry and loading of the solved example.

3.1 Cohesive damage with friction

First, we show how the present model can combine the interface damage corresponding to standardly used cohesive zone contact with friction. The actual state of damage in the adhesive can affect the frictional response in the contact zone. One way of considering such a phenomenon is to prescribe the damage dependent friction coefficient so that for an undamaged interface the friction is not considered, and for fully damaged interface the prescribed friction μ_0 is given. A similar idea appeared in [24], and recently in [25] a power function was used to describe dependence of the friction coefficient on the damage parameter. Therefore, we use a power function to present a friction coefficient which appears significant only for damaged interface, namely: $\mu(\zeta) = \mu_0(1-\zeta)^q$ with $\mu_0 = 0.022$ and two options for the power: $q = 1$ or $q = 4$. The damage of the interface is generally represented by the dependence of $\kappa(\zeta)$ in (3.1d) on ζ. The function $\kappa(\zeta)$ can be appropriately chosen leading to essentially any known cohesive zone model (CZM) as described in [11][13]. For example, the exponential Ortiz-Pandolfi model can be obtained by the function

$$\kappa(\zeta) = \kappa_0 \exp\left(-\gamma_\rho^{-1}(\zeta)\right) \tag{8}$$

where γ_ρ^{-1} is the upper incomplete gamma function, i.e. $\gamma_\rho\ (x) = \int_x^{+\infty} t^{\rho-1}\mathrm{e}^{-t}\mathrm{d}t$. In the solved example we use the values: κ_0= 10 GPa/m, $\rho = 3$.

Alternatively, the bilinear cohesive zone model can be obtained by the function

$$\kappa(\zeta) = \kappa_0 \frac{\beta\zeta}{1+\beta-\zeta} \tag{9}$$

used with the same initial stiffness κ_0 and $\beta = 0.106$, which provides the same value of maximal stress in the cohesive zone as obtained by Eq. (8). An extension of the degradation function in Eq. (9) to multilinear cohesive zone models is also possible as described in [13].

In the present example, only the tangential stiffness component is damaged, because the normal loading is compressive, so that constant high value normal stiffness κ_g from Eq. (1) is activated, here $\kappa_\mathrm{g} =$ 3.85 TPa/m.

The damage is considered rate independent and naturally unidirectional with decreasing ζ. Therefore, the term G from Eq. (3) can be expressed as $G(\dot{\zeta}) = -G_\mathrm{c}\dot{\zeta}$ for $\dot{\zeta} \leq 0$ (otherwise it may be considered infinite) and for given fracture energy $G_\mathrm{c} = 1$ kJ/m^2.

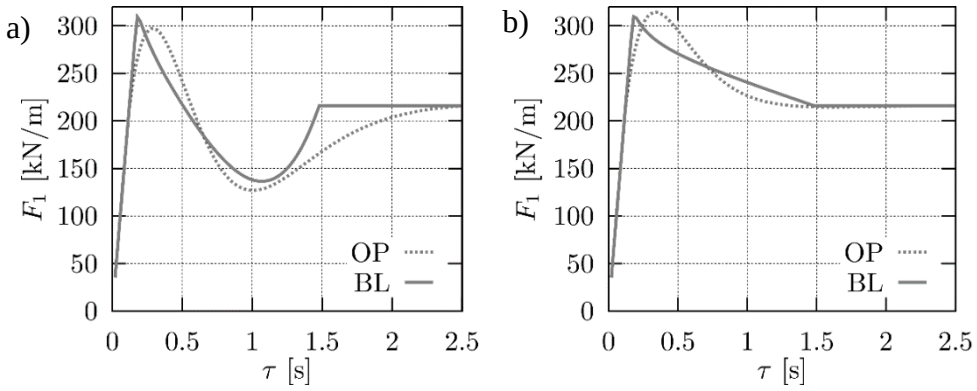

Figure 3: Time dependence of the tangential reaction at the upper face for the Ortiz-Pandolfi (OP), see Eq. (8), and the bilinear (BL), see Eq. (9), CZM and for the friction function μ with: a) $q = 4$, b) $q = 1$.

The global response of the model to the given load can be seen in Figure 3 where F_1 is the total reaction in the direction of the x_1 axis calculated along the rightmost face of the structure. Both aforementioned cohesive zone models and both choices of friction exponent q introduced in the friction-damage relation above are compared. It can be observed that the larger value of q ($q = 4$) causes a putt-off of the frictional behaviour, because $\mu(\zeta)$ for ζ close to one is significantly smaller in comparison to the case $q = 1$. If the bilinear cohesive zone model is used in combination with the linear friction-damage relation ($q = 1$), the combination of the two linear functions causes also (almost) piecewise linear evolution of F_1 as seen in Figure 3b.

The qualitative relation of the stress-strain cohesive law expressed in terms of tangential displacement gap (denoted here u_t) and tangential traction p_t, and damage evolution can be seen in Figure 4 for the same combination of parameters as used for Figure 3. The graphs

demonstrate the relation evaluated at the midpoint of the interface. Intentionally, no values of the quantities are shown, only characteristic shapes of the distributions are compared. As all the data are relative to the maximal obtained value (denoted by the subscript max), including zeta, which is actually 1 in its maximum, the ranges in any case are between 0 and 1.

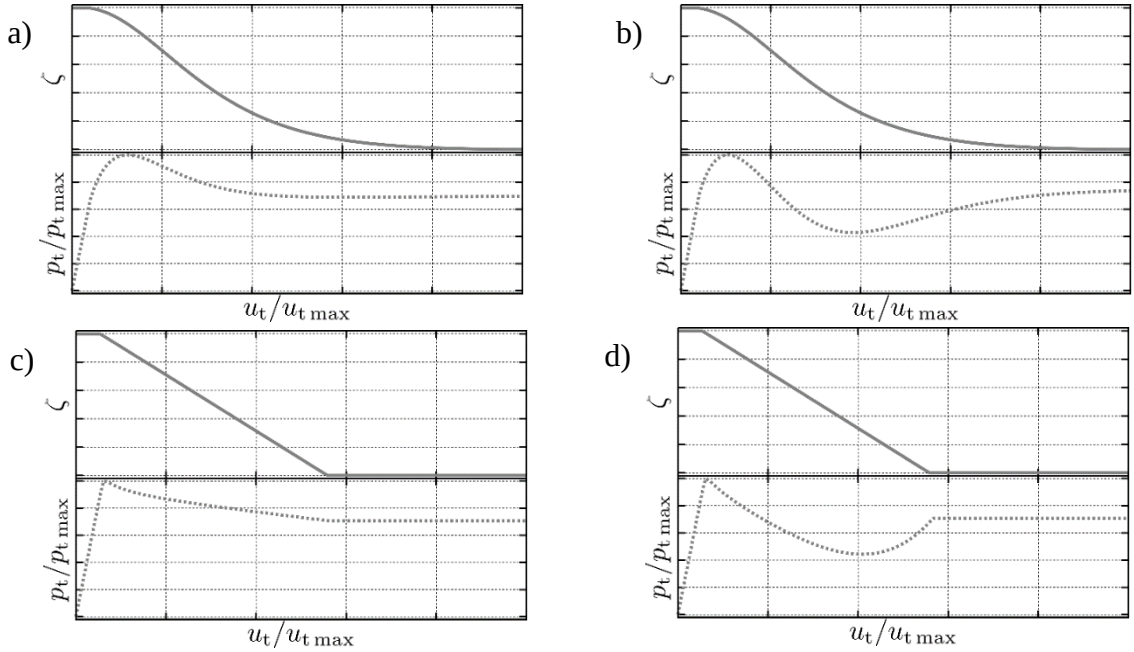

Figure 4: The relation between the damage variable and tangential stress in the middle of the interface in the case of interface damage with friction (without plastic slip): a) OP CZM, friction with $q = 1$, b) OP CZM, friction with $q = 4$, c) BL CZM, friction with $q = 1$, d) BL CZM, friction with $q = 4$.

The graphs in Figure 4ab belong to the case of the Ortiz-Pandolfi model. The stress-strain relation initially behaves accordingly. Nevertheless, the damage parameter decreases during the loading so that the influence of friction becomes significant, and the tangential stress behaviour, shown in the graphs, changes to simulate the frictional response. So that it starts approaching the value pertinent to frictional stress caused by given constant normal pressure. The differences in the tangential stress are caused by different friction parameter q, where its larger value postpones the effect of friction so that the stress-strain relation copies that of the Ortiz-Pandolfi model in a wider range.

The used bilinear cohesive model provides graphs in Figure 4cd. The bilinear nature of the stress-strain relation in the case of the linear dependence of friction on damage ζ is kept, as discussed above for the total reaction F_1. The friction model with $q = 1$ does not spoil linearity because the friction coefficient $\mu(\zeta)$ depends linearly on ζ, and ζ after initiation of damage also depends linearly on the displacement jump. Of course, the combination of the CZM with the other friction model does not keep this property as seen in Figure 4d.

In all the cases, when ζ reaches zero, only friction remains at the interface producing the tangential stress shown.

3.2 Plastic slip and friction

An additional phenomenon considered in this example is the plastic slip along the interface. The functions describing the damage evolution on the interface or the friction-damage dependence are the same as in the previous example. As we have mentioned above, two possible scenarios can be expected.

First, we set the yield stress to the value $\sigma_{\mathrm{y}} = 1.25$ MPa and we use the kinematic hardening with $\kappa_{\mathrm{H}} = 0.5$ GPa/m. The combination of damage and plastic slip provides in this case initiation of damage prior to plastic slip triggering, if the cohesive zone model allows increasing of the stress when damage evolves (as in the case of the Ortíz-Pandolfi model). Otherwise, the plasticity is initiated first and then, after reaching pertinent stress value, the damage process starts.

The total reaction force F_1 obtained along the rightmost face can be seen in Figure 5. In the case of Ortiz-Pandolfi model in Figure 5a, ζ starts to evolve before plastic slip evolves and the part of the plastic slip variation is not linear. Here, we show also results for the frictionless case ($\mu = 0$) to see the influence of the friction on the calculated reaction in detail. There is no tangential force appearing between the block when the interface is totally broken.

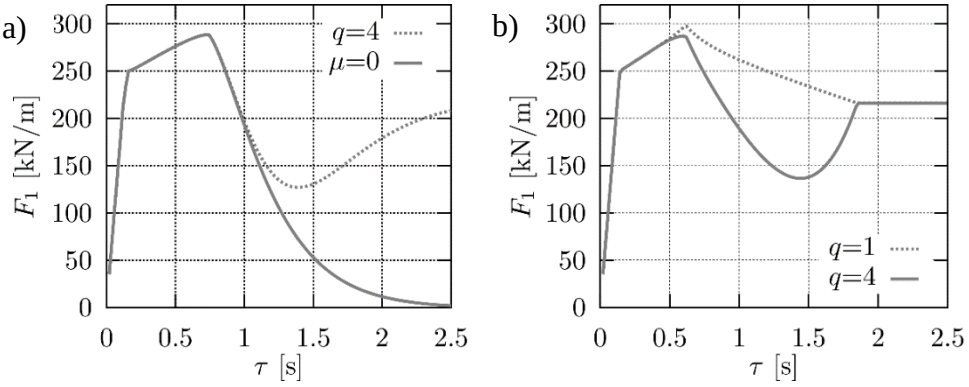

Figure 5: Time dependence of the tangential reaction at the upper face at the presence of plastic slip with constant yield stress $\sigma_{\mathrm{y}} = 1.25$ MPa and with kinematic hardening: a) OP CZM either for friction with $q = 4$ or without friction $\mu = 0$, and b) BL CZM, friction with q in the key.

On the contrary, the graphs in Figure 5b correspond to the use of the bilinear cohesive zone model, they differ in the friction function used. The difference from the case of no plastic slip in Figure 3 is in the intermediate part where the plastic slip evolves, because plasticity is initiated before the stress conditions could trigger damage.

The differences in the evolution of the plastic slip in relation to both cohesive zone models and both friction options can also be seen in Figure 6 with qualitative plots of the stress (in terms of the tangential traction p_t), damage and plastic-slip vs. jump of tangential displacement u_t. The graphs are again plotted for the midpoint of the interface.

When we look at the results with the Ortiz-Pandolfi model in Figure 6ab, we can observe the mutuality in the evolution of damage and plastic slip. The damage starts first, then after reaching the yield stress plastic slip is triggered. In this phase both evolve due to plastic hardening. When

the maximal cohesive stress is reached, the plastic slip stops increasing. The rest of the stress-strain relation is modified due to presence or absence of friction.

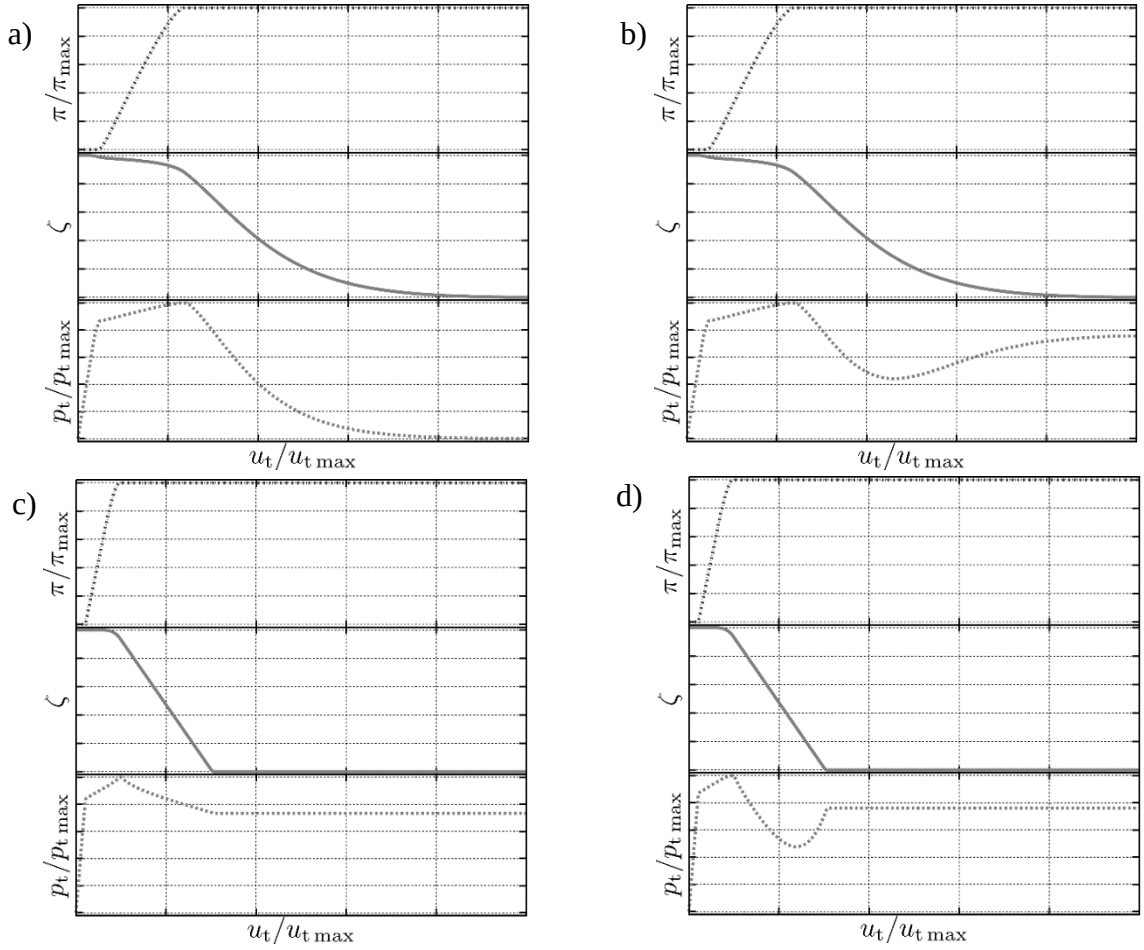

Figure 6: The relation between plastic slip, damage and tangential stress in the middle of the interface as functions of invoked displacement gap: a) OP CZM, no friction, b) OP CZM, friction with $q = 4$, c) BL CZM, friction with $q = 1$, d) BL CZM, friction with $q = 4$.

In the bilinear cohesive model in Figure 7cd, first the yield stress is reached and only afterward the interface is damaged. The evolutions of plastic slip and damage are separated. Nevertheless, after the complete damage, the tangential stress due to friction remains as in the other cohesive zone model. The stress-strain relations are different due to various friction models used.

Alternatively, the coupling of damage and plastic slip can be set up in another way. The dependence of the yield stress σ_y on the actual damage state can lead to initiating the plastic slip after some damage evolved. In such a case, the damage stops varying unless plastic hardening is considered. Such a case can be obtained if, e.g. in the second Eq. (4) combined with Eq. (1) and Eq. (3) (without friction), we try to eliminate the dependence on ζ by choosing

$$\sigma_y(\zeta) = \frac{\kappa_s(\zeta)}{\kappa_{s0}}\sigma_{y0} \text{ with } \sigma_{y0} = 5\text{MPa}. \tag{10}$$

The choice of σ_{y0} provides the tangential stress upon evolving plastic slip with frozen damage state at the same level as obtained by the friction for the current μ_0 and the prescribed normal load. This combination of parameters provides $\sigma_{y0}=\kappa_{t0}[\![u]\!]_t$ at the moment of the plastic slip initiation, which substituted into the stress relation for the cohesive relation derived in [11] provides the actual yield stress at the frozen level of damage as

$$\sigma_y = \sigma_{y0}\exp\left(1-\sigma_{y0}\sqrt{\frac{\alpha}{G_c\kappa_{s0}}}\right). \tag{11}$$

The total reaction force F_1 obtained again along the rightmost face can be seen in Figure 7 for the Ortiz-Pandolfi cohesive zone model. We compared the evolution of the force in the present case to the case with no plastic slip but with friction plotted also in Figure 3a. When the damage variable ζ decreases so that the yield stress is sufficiently decreased, too, plastic slip starts to evolve. This stops damage variation because no hardening is considered so that the stress remains constant. Let us remind that the coincidence of the tangential reaction due to friction and the yield stress is only due to particular choice of the values in this example.

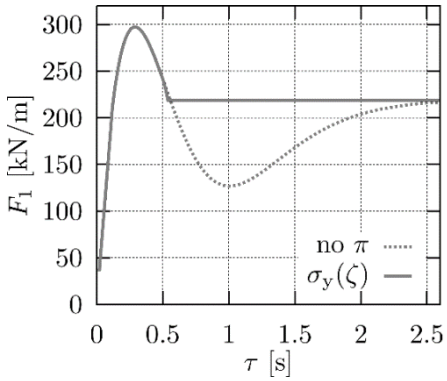

Figure 7: Time dependence of the tangential reaction applied at the upper face in the presence of plastic slip with damage dependent yield stress $\sigma_y(\zeta)$ according to Eq. (10) and without hardening. The damage obeys OP CZM and the actual yield stress is adjusted so that the tangential stress is approximately the same as for the problem without the plastic slip shown also in Figure 3a.

The behaviour of the interface variables can be seen better in Figure 8, plotted for the midpoint of the interface. The stress-jump of tangential displacement law, unlike that in Figure 4b, is frozen at the appropriate yield stress. Similarly, the damage evolution is stopped at the pertinent level. The plastic slip, however, keeps increasing with increasing prescribed displacements given by the Dirichlet boundary conditions.

4 Conclusion

An energy-based model of adhesive contact for initiation and growth of interface cracks under quasi-static conditions has been considered. The general model provides a kind of sensitivity to the crack mode, i.e. whether the interface is broken in the opening mode, shearing mode or generally a combination of both modes. The model also provides additional dissipation which appears due to present friction. It is also relevant only for interface cracks in the shearing mode

when the crack surfaces slide on each other. The variability of the model parameters can be used to adjust calculated results in relation to experimental observations.

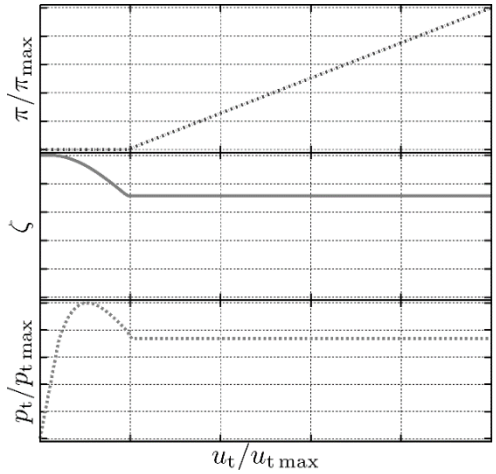

Figure 8: The relation between plastic slip, damage and tangential stress in the middle of the interface in the presence of plastic slip with damage dependent yield stress $\sigma_y(\zeta)$ and without hardening.

The numerical analysis has been performed for an abstract example which resulted to the crack initiation and growth in shearing mode. The results confirm the expected behaviour of the proposed model and positively assess its applicability to problems with initiation and evolution of interface cracks.

Acknowledgements

The author acknowledges support from the grants VEGA 1/0199/20 and 1/0374/19.

References

[1] Lemaitre J, Desmorat R (2005) *Engineering damage mechanics*. Springer, Berlin.

[2] Besson J, Cailletaud G, Chaboche J, Forest S (2010) *Non-linear mechanics of materials.* Springer, Dordrecht.

[3] Roubíček, T., Kružík, M., Zeman, J. (2012). Delamination and adhesive contact models and their mathematical analysis and numerical treatment. In V. Mantič, editor, *Mathematical Methods and Models in Composites,* chapter 9, pages 349–400. Imperial College Press, 2014.

[4] Bourdin, B., Francfort, A., Marigo, J.J. (2008). *The Variational Approach to Fracture*, Berlin: Springer.

[5] Raous, M., Cangémi, L., Cocu. M. (1999) A consistent model coupling adhesion, friction, and unilateral contact. *Comput. Methods Appl. Mech. Engrg.,* 177:383–399.

[6] Sofonea, M., Han, W., Shillor, M. (2006) *Analysis and approximation of contact problems with adhesion or damage*. Chapman & Hall/CRC, Boca Raton, FL.

[7] Del Piero, G., Raous, M. (2010) A unified model for adhesive interfaces with damage, viscosity and friction. *Eur. J. Mech. A/Solids*, 29:496–507.

[8] Kružík M, Panagiotopoulos C, Roubíček T (2015) Quasistatic adhesive contact delaminating in mixed mode and its numerical treatment. *Math Mech Solids* 20:582–599.

[9] Wriggers. P. (2006) *Computational contact mechanics* (2nd edition). Springer, Berlin, 2006.

[10] Vodička, R., Mantič, V., Roubíček, T. (2014) Energetic versus maximally dissipative local solutions of a quasi-static rate-independent mixed-mode delamination model. *Meccanica*, 49:2933–296.

[11] Vodička, R. (2016) A quasi-static interface damage model with cohesive cracks: SQP–SGBEM implementation. Eng. Anal. Bound. Elem., 62:123–140.

[12] Vodička, R., Mantič, V., Roubíček, T. (2017) Quasistatic normal-compliance contact problem of visco-elastic bodies with Coulomb friction implemented by QP and SGBEM. *Journal of Computational and Applied Mathematics*, 315:249–272.

[13] Vodička, R. Mantič, V. (2017) An energy-based formulation of a quasi-static interface damage model with a multilinear cohesive law. *Disc. Cont. Dynam. Syst. - S*, 10:1539–1561.

[14] Roubíček, T. (2019) A general thermodynamical model for adhesive frictional contacts between viscoelastic or poro-viscoelastic bodies at small strains. *Interfaces and Free Boundaries* 21: 169-198.

[15] Rossi, R., Roubíček, T. (2013) Adhesive contact delaminating at mixed mode, its thermodynamics and analysis. *Interfaces and Free Boundaries*, 14:1–37.

[16] Roubíček, T., Mantič, V., Panagiotopoulos, C.G. (2013) Quasistatic mixed-mode delamination model. *Discr. Cont. Dynam. Systems Ser. S*, 6:591–610.

[17] Banks-Sills, L., Ashkenazi, D. (2000). A note on fracture criteria for interface fracture. *Int. J. Fract.* 103, 177–188.

[18] Hutchinson, J.W., Suo, Z. (1992). Mixed mode cracking in layered materials. *Advances in Applied Mechanics*, 29, 63–191.

[19] Sutradhar, A., Paulino, G.H., Gray, L.J. (2008) *The symmetric Galerkin boundary element method.* Springer-Verlag, Berlin.

[20] Vodička, R., Mantič, V., París, F. (2007) Symmetric variational formulation of BIE for domain decomposition problems in elasticity - an SGBEM approach for nonconforming discretizations of curved interfaces. *CMES – Comp. Model. Eng*., 17:173–203.

[21] Panagiotopoulos, C.G., Mantič, V., Roubíček, T. (2014) A simple and efficient BEM implementation of quasistatic linear visco-elasticity. *Int. J. of Solids and Structures*, 51:2261–2271.

[22] Dostál, Z. (2009) *Optimal Quadratic Programming Algorithms*, Springer Optimization and Its Applications, 23. Berlin: Springer.

[23] Nocedal, J., Wright, S. (2006) *Numerical Optimization*. Springer.

[24] Cocou, M., Schryve, M., Raous, M. (2010) A dynamic unilateral contact problem with adhesion and friction in viscoelasticity. *Z. Angew. Math. Phys*., 61:721–743.

[25] Kšiňan, J., Vodička, R. (2016) An SGBEM implementation of contact models coupling the interface damage and Coulomb friction in fibre-matrix composites. *Engineering Fracture Mechanics*, 168:76–92.

DOI: 10.1515/sspjce-2019-0014

Characterization of sandstones of eastern Slovakia

Pavol Jaroš, Marián Vertaľ

Technical University of Košice, Slovakia
Faculty of Civil Engineering, Institute of Architectural Engineering
email: pavol.jaros@tuke.sk, marian.vertal@tuke.sk

Abstract

The main building material in the past was stone. Geological composition influenced the choice and type of building stone, which was used for the construction of the buildings. In eastern Slovakia sandstone was used in large quantities for its good compressive properties, good workability and aesthetic appearance. Sandstones were used for decorative but mainly construction purposes. The most common problem in historical stone structures is missing waterproofing insulation. Transmission and storage parameters of heat and water of historical materials are needed to assess the moisture condition of buildings and to correctly design measures. In this article are presented researches of sandstones properties abroad and locations of selected sandstones of eastern Slovakia, which were used for construction of historical buildings.

Key words: historical building, sandstone, hygrothermal properties, water absorption coefficient

1 Introduction

At present, great emphasis is placed on reducing the energy performance of buildings. In order to achieve the energy and climate objectives of the European Union, it is necessary to reduce the energy burden on new and existing building [1]. The construction industry is one of the largest energy consumers, uses a large amount of energy and releases a significant amount of greenhouse gases. European countries have succeeded in reducing the energy consumption of new buildings by more than 50 % [2]. When designing new buildings, there is only a small investment needed to be low-energy. However, reducing the energy performance of existing buildings is much more difficult and demanding [3]. Renovation and modernization of historical buildings has an important role to play in reducing greenhouse gas emissions [2]. To design the correct measures it is necessary to know the material properties of the materials used in historical constructions. In eastern Slovakia, sandstone was used in large quantities for construction of buildings. It was used for its good workability,

compressive strength and aesthetic appearance. The used sandstone's transmission and storage parameters of the heat and water are necessary for correct assessment. The thermal and hygric properties of sandstones determine the thermal and moisture behaviour of the building. Only a few scientists in the world have studied these properties of natural sandstones [4].

2 Hygrothermal properties of sandstones in world

In locations of the Czech Republic Koči el al. worked on hygric, thermal and mechanical properties of three sandstones from Kocbeře, Libnava and Záměl [5].

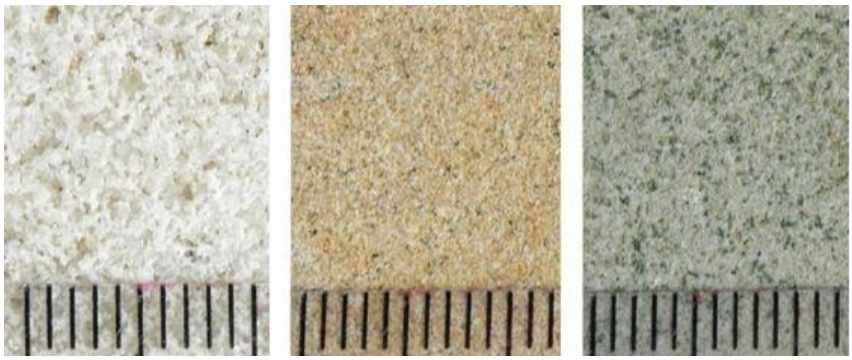

Figure 1: Appearance of measured sandstones from localities Kocbeře, Libnava, Záměl, (Czech republic) [15]

Sandstones from locality Kocbeře and Libnava are fine-grained and sandstone from locality Záměl is medium-grained. All sandstones have high content of quartz. Properties such as bulk density, open porosity, thermal conductivity coefficient, specific heat capacity, diffusion resistance factor and water absorption coefficient are shown Table 1 [5].

Locality	ρ (kg/ m^3)	θ_{por} (m^3/ m^3)	λ (W/m.K)	c (J/kg.K)	u (-)	A_w (kg/m^2.s$^{0.5}$)
Kocbeře	2227.7	0.161	3.53	754	12.7	-
Libnava	2191.0	0.179	2.71	721	11.6	-
Záměl	2075.9	0.228	2.10	694	11.8	-

Table 1: Hygrothermal properties of sandstones of Czech Republic [5]

Martin Krus focused on studying the basic properties of four types of sandstones and their influence on thermal and moisture behaviour in Germany. He studied properties of German sandstones such as Baumberger, Obernkirchner, Ruthener and Sander, which are shown in Table 2 [6].

Locality	ρ (kg/ m^3)	θ_{por} (m^3/ m^3)	λ (W/m.K)	c (J/kg.K)	u (-)	A_w (kg/m^2.s$^{0.5}$)
Baumberger	1980	0.230	-	-	20	0.044
Obernkirchner	2150	0.140	-	-	32	0.046
Ruthener	1950	0.240	-	-	17	0.300
Sander	2120	0.170	1.60	850	33	0.020

Table 2: Hygrothermal properties of sandstones in Germany [6]

The influence of anisotropy on the thermal and hygric properties of four German sandstones was investigated by Jianhua Zao and Rudolf Plagge. The sandstones studied were Arholzen, Karlshafen, Sander, Schleerither. Sandstone Arholzen and Karlshafen are fine-grained and red colored, while Karlshafen is little bit darker. Sander is brownish to olive green and has fine to medium large grains. Sandstone Schleerither is fine-grained and has a gray-green coloration [4].

Figure 2: Sandstones in Germany from left Arholzen, Karshafen, Sander, Schleerither [4]

The measured thermal and hygric properties of sandstones are shown in Table 3.

Locality	Orientation	ρ (kg/ m^3)	θ_{por} (m^3/ m^3)	λ (W/m.K)	c (J/kg.K)	u_{dry} (-)	A_w (kg/m^2.s$^{0.5}$)
Arholzen	Perpendicular	2276.1	0.149	2.54	788	97.6	0.017
	Parallel			2.54	828	61.8	0.020
	Anisotropy (%)	-	-	0	4.8	36.7	15
Karlshafen	Perpendicular	2415.7	0.099	3.28	796	178.5	0.006
	Parallel			3.50	792	118.5	0.009
	Anisotropy (%)	-	-	6.3	0.5	33.6	33.3
Sander	Perpendicular	2032.4	0.233	1.41	717	25.9	0.056
	Parallel			1.41	678	24.2	0.087
	Anisotropy (%)	-	-	-	5.4	6.6	35.6
Schleerither	Perpendicular	2261.9	0.162	1.97	774	25.5	0.024
	Parallel			2.07	773	24	0.030
	Anisotropy (%)	-	-	4.8	0.1	5.9	20

Table 3: Influence of anisotropy [4]

These values show us that anisotropy does not have a major influence on the thermal properties of selected sandstones. Sander and Schleerither diffusion resistance factor's values have only low grain dependence. However, the difference in the diffuse resistance factor of Arholzen and Karlshafen is more than 30 %. High dependence on grain direction is also shown by the values of the water absorption coefficient, the lowest Arholzen sandstone, the highest Sander sandstone.

The properties of two Canadian sandstones were studied by Mukhopadhyaya et al., which were used for wall cladding [7]. Nepean sandstone was used for the renovation of the Parliament building in Ottawa, the construction of churches, town halls and Prime Ministers building [11]. Sandstone Saint-Canut from Laurentides is white-gray and is used for the production of tiles [7]. The measured hygrothermal properties are shown in Table 4.

Locality	ρ (kg/ m^3)	θ_{por} (m^3/ m^3)	λ (W/m.K)	c (J/kg.K)	u (-)	A_w (kg/m^2.$s^{0.5}$)
Nepean	2380	-	0.99	-	-	0.003
St. Canut	2495	-	1.04	-	-	0.007

Table 4: Hygrothermal properties of Canadian sandstones [7]

Figure 3 left: Sandstone Nepean [16], right : Sandstone St. Canut [17]

3 Sandstone of eastern Slovakia used in building construction

3.1 Sandstone as a building material in the past

Sandstone belongs to the group of sedimentary rocks. They arise from the process of weathering and disintegration of rocks into sandy grains. The resulting incoherent rocks are solidified by the process of diagnosis, which results in the formation of reinforced sandstones [8].

Sandstone deposits in the territory of the Slovak Republic are predominantly found in flysch zone in the areas of Kysuce, Orava and northeastern Slovakia. At the beginning of the 13th century, after the advent of the Gothic art style, sandstone was the main building material. This artistic style had strict requirements for the choice of building stone. Sandstone due to its good compressive strength, good workability and aesthetic appearance was a suitable material for the construction of buildings in the Gothic style. By the end of the 19th century, 336 quarries for sandstone mining were registered in the territory of eastern Slovakia [9].

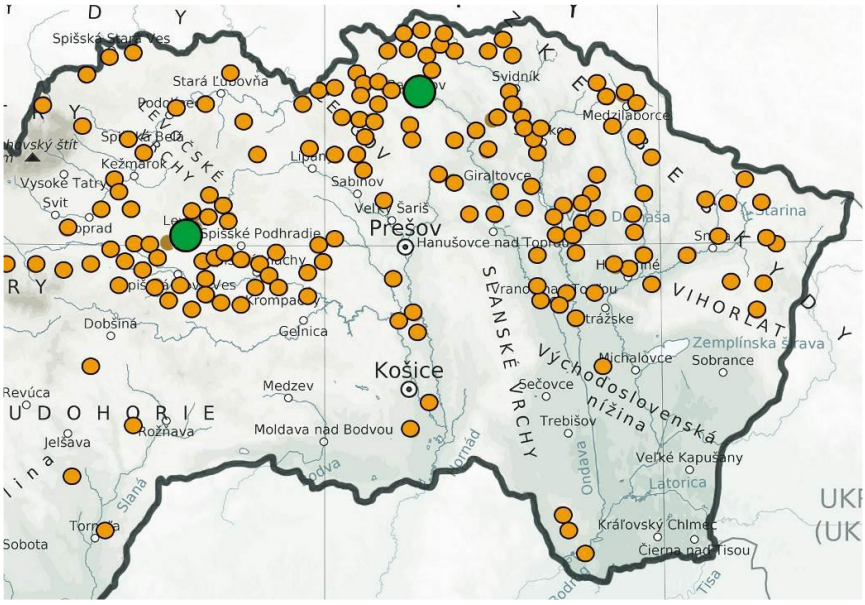

Figure 4: Localization of sandstone quarries in eastern Slovakia [9]

Major towns in which sandstone was mined include Stará Ľubovňa, Kežmarok, Levoča, Spišská Nová Ves and Bardejov. At present all historical quarries are abandoned and dilapidated. The only bearing used for sandstone mining is in Spišské Tomášovce near Spišská Nová Ves. Sandstone was used for all kinds of building such as town halls, churches, mansions, town houses, etc. It was also used for decorative purposes due to its good workability. Portals, ledges, epitaphs, railings, etc. were made from them.

3.2 Sandstone from Kežmarok

Kežmarok is one of the oldest historical towns in the Slovak republic. Like others, its construction began after the onset of the gothic style. The territory of the city falls under the flysch zone. On the north-east side, there is an abandoned sandstone quarry. At present, the quarry is overgrown with greenery, hardly accessible. Sandstone has light to gray color and with grain size from 0,063 to 2 it belongs to fine-grained.

Figure 5 left: Historic quarry Kežmarok, photo [18], right : photo Jaroš, 2019)

In the Middle Ages, sandstone was used for local construction purposes. Construction masters used sandstone for construction of churches, town houses, etc. It was used in large quantities to create entrance portals, which can be seen in the main square. This light colored sandstone was used in the construction of the Basilica of the Holy Cross from 1444, the historic bell tower, the church of the Visitation of the Virgin Mary from 1772, but also for smaller chapels.

Figure 6 left: sandstone Kežmarok, right : entrance portal, Museum of housing Culture, (photos Jaroš, 2019)

During the interior reconstruction, sandstone was also discovered in the masonry of the Museum of Housing Culture at the Main Square in Kežmarok. There is also an entrance portal made of this light colored sandstone.

3.3 Sandstone from Stará Ľubovňa – Kremná

North of the town Stará Ľubovňa there is an abandoned quarry for the mining of sandstone Stará Ľubovňa – Kremná. This sandstone, like sandstone from Kežmarok, falls under the flysch zone. It has a light, gray and yellow-brown color. Grain sizes from 0.002-2 are classified as fine-grained.

Figure 7 left: quarry Stará Ľubovňa – Kremná, right : sandstone Stará Ľubovňa, (photos Jaroš, 2019)

In the past, it was used for local construction purposes. It was used as a building stone but also for decorative and aesthetic purposes. Fractions of this sandstone were found in the Stará Ľubovňa castle (13th century), and also in the masonry of st. Michael's Roman Catholic Church (end of 13th century).

Figure 8 left : masonry of church St. Nicholas, right : portal in the castle of Stará Ľubovňa, (photos Jaroš, 2019)

3.4 Sandstone from Spišská Nová Ves – Spišské Tomášovce

West of the town of Spišská Nová Ves there is an active quarry for the mining of sandstone Spišské Tomášovce. This sandstone, like others, belongs to the flysch zone. It has a light to gray color. Grain sizes from 0.002 to 2 are fine grains. Currently, there continues an active mining. It is used for production of aggregates for civil engineering and civil engineering purposes. Crushed aggregate is not suitable for concrete purposes, because it contains pyrite.

Figure 9: Quarry for mining of sandstone Spišské Tomášovce (photo Jaroš, 2019)

According to research of engineering geologists from Comenius University in Bratislava, the sandstone of Spišské Tomášovce is not suitable for restoration of historical buildings in terms of block dimensions (min. 600 mm), but it is suitable for its compressive strength. It also shows good frost resistance **Chyba! Nenašiel sa žiaden zdroj odkazov.**.

4 Heat and water transfer parameters – water absorption coefficient, capillary water content

4.1 Preparation of samples for measurement

One of the transmission parameters of water which is important for HAM simulation, is the water absorption coefficient and capillary water content. These parameters are determined by a one-dimensional water transport experiment. Prism or cylinder - shaped samples are stored in a reservoir of water. To prevent one dimensional transport of water it is necessary to insulate the sides with waterproof and vapor-proof material. It is important to insulate the sides so that water does not rise in the space between the sample and the insulating material. The top base is also resistant to vapor transmission, but there are holes for expelling the air pushed out of the pores [12].

The measuring instrument shall include a device for maintaining a constant water level, a balance accurate to 0,01g, an over with air ventilation (70°C), a length measuring device, an air-conditioned room capable of maintaining the temperature at ± 20°C [14]. Area of samples according to [13] should be minimal 50 cm^2. According to [14] the dimensions of the base shall be either 70x70 mm or 50x50 mm with a height of 70 mm or 50 mm. Samples may be untreated after cutting. Before measurement, the samples must be dried in a desiccator at a temperature ± 70°C [14]. The specimens are made from homogeneous batches using an electric saw with a stone blade. Base dimensions 50x50 mm with a height of 70 mm.

Figure 10: Preparation of sandstone samples

Figure 11: Samples of sandstones top view : from the left: Kežmarok, Stará Ľubovňa - Kremná, Spišské Tomášovce

Figure 12: Samples of sandstones – front view : Kežmarok, Stará Ľubovňa – Kremná, Spišské Tomášovce

A measuring set was constructed for measurement of water absorption coefficient and capillary water content. The device consists of an analytical balance, holder for holding the sample in water, container with distil water and timer. The instrument is connected to a computer for automatically recording weight gain over time.

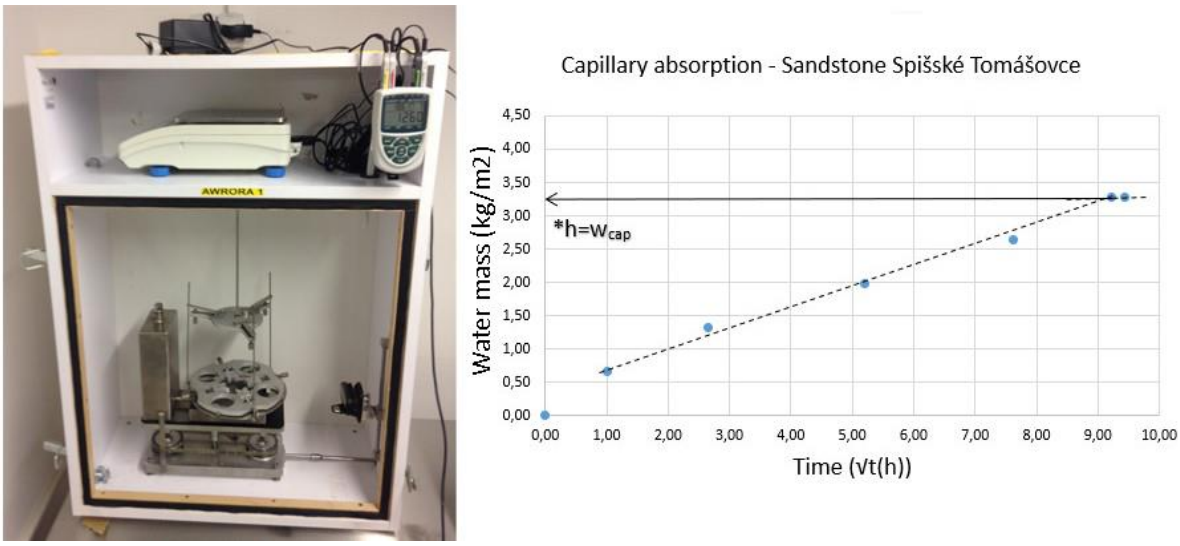

Figure 13 left: measuring set (AWRORA), right : water absorption course

The water absorption coefficient can be determined by following equation:

$$A_{cap} = \frac{m_{wet} - m_{dry}}{\sqrt{t}} \quad (1)$$

where A_{cap} is water absorption coefficient $(kg/m^2.s^{0,5})$, m_{wet} is water mass (kg/m^2) per area S (m^2), m_{dry} is weight of dry sample (kg/m^2) per area S (m^2), t is time.

The capillary water content can be determined by following equation:

$$w_{cap} = \frac{m_{wet} - m_{dry}}{A} . \frac{1}{H} \quad (2)$$

where w_{cap} is capillary water content (kg/m^3), m_{wet} is water mass (kg/m^2) per area S (m^2), m_{dry} is weight of dry sample (kg/m^2) per area S (m^2), t is time, H is the height of the sample (m).

5 Conclusion

There are only a few research works, which deal with complex heat, air and water transport in sandstones. Transmission parameters were studied by scientist in Canada, Germany and Czech Republic. There were a large number of quarries for sandstone mining in the territory of eastern Slovakia. Sandstone samples were collected from selected historical quarries and found in historical buildings and monuments. Samples were taken from the collected homogeneous sandstones for measuring the water transfer parameter, namely the water

absorption coefficient and capillary water content, which are one of the important parameters that allow modelling complex heat, air and water transport in buildings. The samples are prepared for one-dimensional transport of water experiment, which indicates capillary moisture transport ability of porous materials.

Acknowledgements

This work was supported by the VEGA: 1/0674/18 Theoretical and experimental analysis of architectural-structural shapes and fragments of building envelope structures designed for harsh conditions.

References

[1] Ma, Z. *et al.* (2012). Existing building retrofits: Methodology and state-of-the-art. *Energy and Buildings*. Elsevier B.V. 55. pp. 889–902. doi: 10.1016/j.enbuild.2012.08.018.

[2] Asadi, E. *et al.* (2014). Multi-objective optimization for building retrofit: A model using genetic algorithm and artificial neural network and an application. *Energy and Buildings*. Elsevier B.V. 81. pp. 444–456. doi: 10.1016/j.enbuild.2014.06.009.

[3] Hendron, R. *et al.* (2013). *Advanced Energy Retrofit Guide (AERG): Practical Ways to Improve Energy Performance; Healthcare Facilities (Book)*. Golden, CO (United States). doi: 10.2172/1096100.

[4] Zhao, J. and Plagge, R. (2015). Characterization of hygrothermal properties of sandstones - Impact of anisotropy on their thermal and moisture behaviors. *Energy and Buildings*. Elsevier B.V. 107. pp. 479–494. doi: 10.1016/j.enbuild.2015.08.033.

[5] Kočí, V. *et al.* (2014). Service life assessment of historical building envelopes constructed using different types of sandstone: A computational analysis based on experimental input data. *Scientific World Journal*. doi: 10.1155/2014/802509.

[6] Krus, M. (1996). *Moisture transport and storage coefficients of porous mineral building materials: Theoretical Principles and New Test Methods*. Fraunhofer IRB Verlag. Stuttgart.

[7] Zhao, J. and Plagge, R. (2015). Characterization of hygrothermal properties of sandstones - Impact of anisotropy on their thermal and moisture behaviors. *Energy and Buildings*. Elsevier B.V. 107. pp. 479–494. doi: 10.1016/j.enbuild.2015.08.033.

[8] Čabalová, D. and Šamalíková, M. (1992). *Inžinierska geológia*. Bratislava: Alfa.

[9] Čabalová, D. (2013). *Krása kameňa v živote človeka*. Bratislava: Veda.

[10] Laho, M. *et al.* (2009). Výber stavebného kameňa pre rekonštrukciu historických objektov. *Acta Geol. Slovaca (AGEOS)*. 1. pp. 9–14.

[11] Deachman, B. (2018). Q is for Quarry: Forgotten, overgrown quarry provided the building blocks of Ottawa', *Ottawa citizen*.

[12] Vertaľ, M. and Ďurica, P. (2013). *Prenosové parametre vody vo vybraných stavebných materiáloch*. Košice: Technická univerzita v Košiciach, Stavebná Fakulta.

[13] STN EN ISO 15148. (2002). Tepelno-vlhkostné vlastnosti stavebných materiálov a výrobkov. Stanovenie koeficientu nasiakavosti pri čiastočnom ponorení.

[14] STN EN 1926. (2002). Skúšky prírodného kameňa. Stanovenie súčiniteľa nasiakavosti kapilaritou.

[15] Kočí, V. *et al.* (2014). Service life assessment of historical building envelopes constructed using different types of sandstone: A computational analysis based on experimental input data. *Scientific World Journal*. online: https://www.hindawi.com/journals/tswj/2014/802509/fig1/

[16] Gall, Q. Section through Nepean formation sandstone and overlying March formation dolostone and sandstone. online: http://www.stunley.com/ogg/site_2centrum.htm

[17] Énergie et Ressources naturelles. Saint-Canut-Sainte-Scholastique. online: https://mern.gouv.qc.ca/english/mines/industry/architectural/architectural-quarrying-history-sandstone-saintcanut.jsp

[18] Bednarik, M. Laho, M. Holzer R. Historic quarries. online: http://saxa.chc.sbg.ac.at/img/quarries/478_2.jpg

DOI: 10.1515/sspjce-2019-0015

Experimental determination of the efficiency of the solar collector integrated into the light transparent building facade

Vasyl Zhelykh[1], Peter Kapalo[2], Stepan Shapoval[1], Iryna Venhryn[1], Khrystyna Kozak[1]

1 National University "Lviv Polytechnic", Institute of Building and Environmental Engineering, Department 'Heat and Gas Supply and Ventilation', Lviv, Ukraine
e-mail: iryna.i.venhryn@lpnu.ua
[2] Technical University of Košice, Faculty of Civil Engineering, Institute of Architectural Engineering
e-mail: peter.kapalo@tuke.sk

Abstract

One of the most promising energy sources is solar energy, which is confirmed by the growth in the development of renewable energy for European countries. The main goal of research is to design and implement the latest energy systems for passive buildings using renewable energy. In this paper is documented the optimal operation stages of the solar heat supply system were investigated with recommendations for further development of the design and construction of passive buildings in Ukraine South.

Key words: solar collector, building, facade, solar heating system, thermal energy

1. Introduction

Solar radiation is an inexhaustible source of renewable clean energy. The flow of solar radiation coming to the earth's surface is uneven. The amount of solar radiation entering on the earth's surface ranges from ≈3000 MJ to ≈8000 MJ per 1 m^2. Taking into account this range of solar energy input, installations that convert solar radiation into thermal or electrical energy are used. Such installations are solar collectors. Previous studies have found that the amount of solar energy entering on the territory of Ukraine is generally sufficient for its use [1]. This amount of solar radiation is greater for the territory of Europe.
Solar energy could be used efficiently in the immediate vicinity of the consumer, that is, without transmitting energy over a significant distance [2]. For the needs of the consumer's heat supply must be used heat supply system. However, if the system contains a solar collector, it can be considered as a solar heat supply system (SHSS). In addition, to receiving solar radiation from space to the surface of the solar collector, it is recommended to take into account the albedo of solar radiation [3, 4]. The albedo of solar radiation depends on the

nature of the area and its geographical latitude, where the solar collector is located. In paper [5] was obtained albedo data for various surfaces based on NASA operational data from June 11 to June 26, 2006. For example, the average albedo values for the latitudes of Ukraine are higher than the planetary value around 30% and make up 38%.
Solar collectors could work both independently and as part of traditional energy facilities in heating and air conditioning systems, for additional supply to boilers and so on. However, it is necessary to choose the mode of operation of the solar collector depending on its location in the SHSS. The traditional design of the flat solar collector consists of an insulating material, circulation pipelines, and a heat-receiving surface (absorber). Such designs of solar collectors allow to get a heat carrier with a temperature up to 70 °C.
A new direction in designing of solar collectors can be considered their integration into building fences.
The argument for integrating solar collectors into the building structure was presented at a conference in Germany [6]. It was established that solar collectors with proper design are no less effective than heat pumps. They also stressed the need to take measures to reduce the cost of the system by selecting solar collectors in building structures during the design and construction of facades and roofs which confirms the need for further research.
Today, energy-efficient architectural construction in combination with solar heat supply systems is increasingly being considered [7]. For instance, the use of renewable energy in relation to glass and solar architecture. A more detailed analysis of solar houses is carried out in the literature [8, 9]. It is advisable to take into account the technical and economic indicators of the construction of a new building with different parameters of hardness around it [10]. The building spot, in particular the building seal, helps to reduce the specific heat loss of the house. In particular, those homes that have interior space are more energy-efficient [7].
In Poland, a law on thermoregulation was adopted, the main objectives of which were to increase the normative indicators of annual heat consumption of buildings and increase the requirements for indicators of heat transfer coefficients of building fencing elements [11].
The main goal of research in a scientific and technical project [12, 13, 21] are to design and implement the latest energy systems for passive buildings using renewable energy. The optimal operation stages of the solar heat supply system were investigated with recommendations for further development of the design and construction of passive buildings. It is also worth paying attention to labour [14], which describes the principles of designing energy efficient buildings in the Ukraine South.

2. Objectives the Formulation of the Problem

Many papers believe that the energy sector should play a central role in any transition to low carbon consumption since it is the single largest source of carbon emissions. Data shows that demand for electricity increased by 3.7%, which is one of the highest growth rates in the last 20 years. In terms of offers, the increase in electricity production was driven by renewable energy sources, which grew by 14.5%, providing about a third of the growth. For European countries in the statistics described in [15] data on the development of renewable energy from 2010 to 2018 in millions of tons of oil equivalent are provided. On the basis of these data, the development of renewable energy was predicted to 2030 and the possibility of reaching 300 million tons of oil equivalent for the renewable energy was established (Fig. 1). The sharp

growth of this type of energy in Europe is due primarily to the deterioration of installations that operate from traditional energy as a result of energy efficiency programs that are developed by European governments.

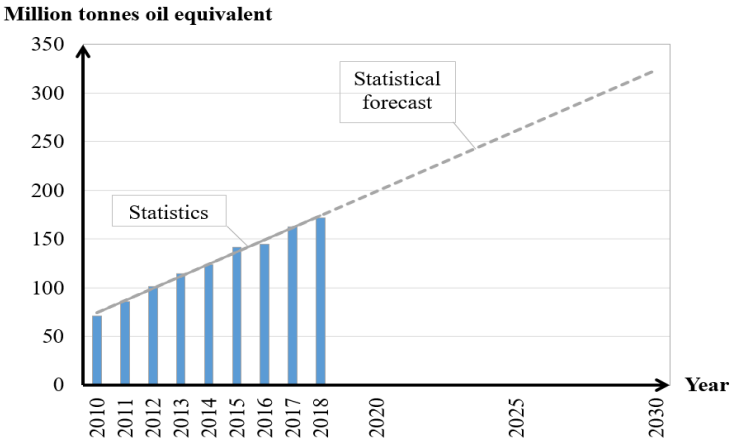

Figure 1: Development of renewable energy in Europe with a forecast until 2030 (according to information of the British Petroleum).

For example, labor [16] emphasizes the problem of energy consumption in Ukraine in the field of construction. In mathematical modelling of the thermal regime of houses, a systematic approach prevails in which the house is considered as a single energy system consisting of interdependent elements. As a result, the paper presents functional equations for optimizing the shape of a General body that is located in an arbitrary radiation thermal field. In addition, the improvement of structures with mathematical modelling of heat exchange in heat exchangers of ventilation systems of energy-saving buildings was carried out [17].
Taking into account the development trend of renewable energy in Ukraine and the need for its development in the field of construction, there are works that offer designs of solar collectors combined with the exterior fences of the building. For example, the work of a wall solar collector on labor [18], with a frame housing, which is installed on a transparent (glass) surface, mounted in the external fence of the building. Or the construction of a solar wall, where the solar collector for the needs of heat supply is integrated into the wall of the building.
However, such structures are not provided for buildings with an increased area of the glass facade.

3. The Main Material

Taking into account the development of renewable energy in Ukraine and the construction of glass facades, it was proposed to combine the solar collector with the glass facade of the building while integrating it into the glass fence. Studies of the proposed installation were carried out for the mode of natural circulation of the heat carrier and for the intensity of simulated solar radiation of 300 W/m^2.
The experimental solar heat supply system worked according to the following scheme: the heat carrier enters the storage tank; when opening and setting up the shut-off and adjustment

valves, the water enters the solar collector, is heated by solar energy and moves back to the storage tank according to the principle of natural convection (Fig. 2).
The main, invariable, conditions of research were:
1 – the system, before each study, was filled with a fresh portion of water;
2 – air was being removed from the system;
3 – the intensity of the solar energy flow was measured using a pyranometer;
4 – the temperature of the heat carrier was measured by mercury thermometers at three points in the system (at the outlet of the solar collector, at the inlet to the collector, and in the storage tank);
5 – the ambient temperature and its speed were measured by a thermoelectro anemometer TESTO 405 – V1.

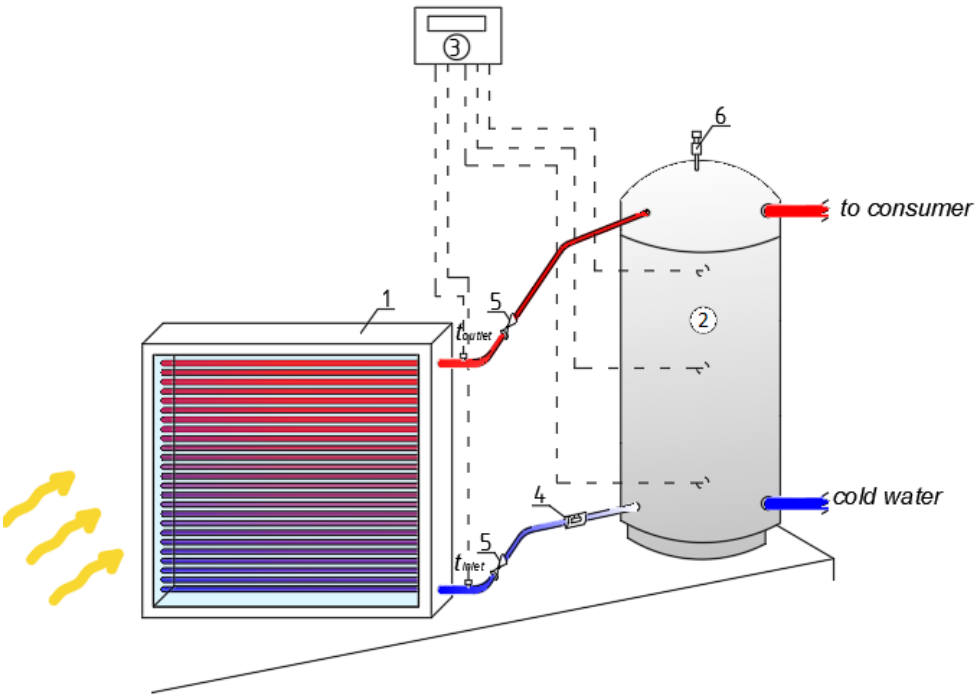

Figure 2: Experimental solar heating system in which solar collector is combined with the glass facade of the building, where 1 – the solar collector 2 – the storage tank of the heat energy 3 – display of gathering information from the temperature sensors, 4 – the check valve 5 – shut-off and control valves, 6 – panel security of the system solar heating

The temperature change of the carrier heat at the inlet and outlet from the solar collector is shown in Fig. 3. In addition, in Fig. 3 shows data on changes in the ambient temperature. It was found that the intensity of the simulated solar radiation flow 300 W/m^2, the temperature at the outlet of the solar collector reached 41 °C, which is about 50% higher than the temperature at the inlet to it.

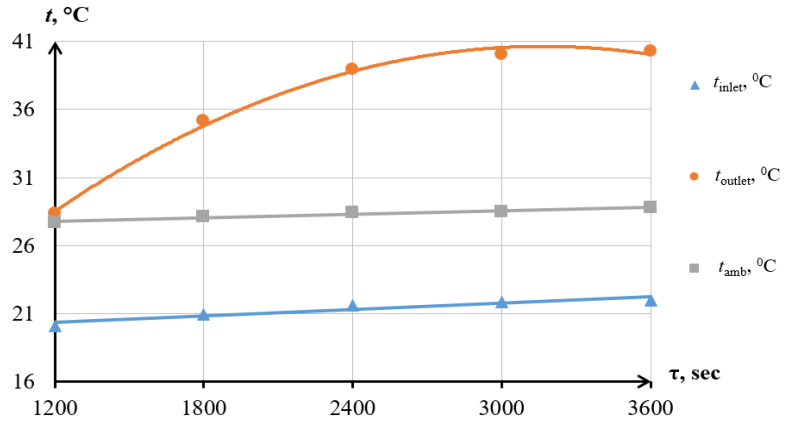

Figure 3: Determining the temperature change of the heat carrier during the experiment at the inlet and outlet of the solar collector, which is combined with the glass facade of the building

In Fig. 4 data on changes in the temperature of the heat carrier in the thermal energy storage tank during experimental studies are presented. It could be seen that the temperature of the heat carrier in the solar heat transfer system in the mode of natural circulation of the heat carrier on average reached 20.5°C.

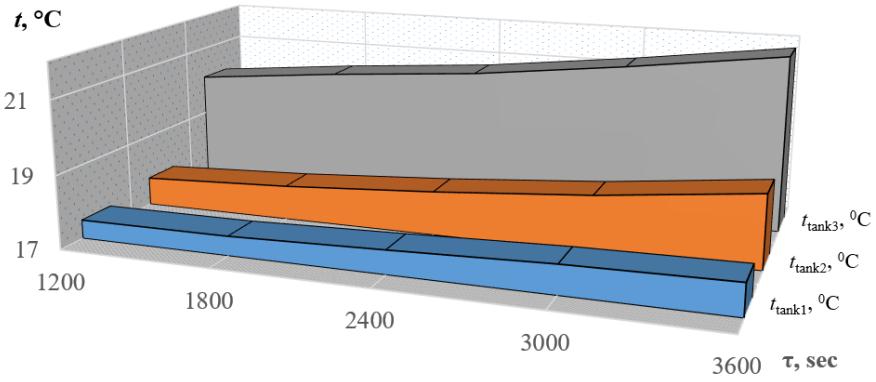

Figure 4: Investigation of changes in the temperature of the heat carrier during experimental studies in the heat energy storage tank

The amount of heat energy from solar radiation entering on the solar collector is a function of the intensity and time (1):

$$Q = f(I, \tau) \tag{1}$$

where: Q – the amount of heat energy from solar radiation entering on the collector, kJ/m^2; I – intensity of solar energy entering on the solar collector plane, W/m^2; τ – time of the experiment, sec.

The change in the average specific maximum heat energy stored in the storage tank is graphically shown in Fig. 5. Moreover, the data of thermal energy that was received with the

intensity of simulated solar radiation to the surface of the solar collector with accumulation are given. Averaging the results obtained, it can be established that the difference between the obtained parameters is ≈57%.

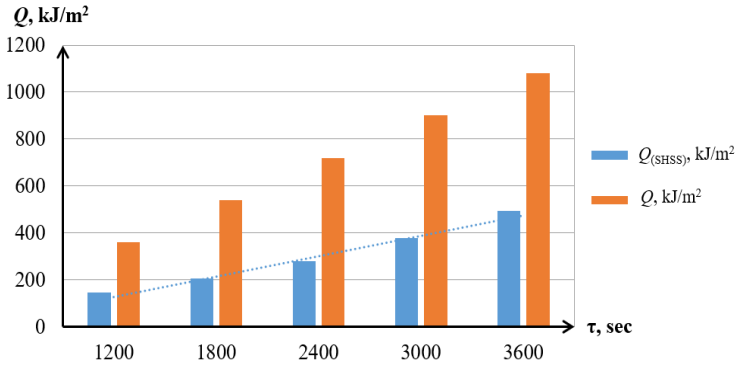

Figure 5: Changes in the thermal energy stored in the storage tank Q(SHSS) and the amount of simulated solar radiation received on the surface of the solar collector in time with accumulation Q.

Analyzing the efficiency of a solar heat supply system (SHSS) with a solar collector in the mode of natural circulation of the heat carrier, the efficiency coefficient reached an average of 46%. It is worth noting that the change in the thermal efficiency of the solar heat supply system ŋSHSS with a solar collector takes an increasing trend (Fig. 6).

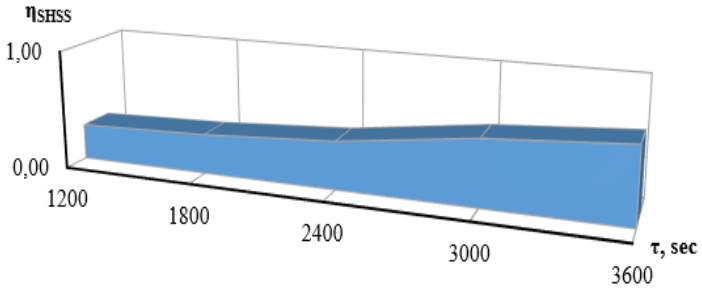

Figure 6: Establishing the efficiency of the solar heat supply system during the experiment with the collector integrated into the glass facade of the building

Therefore, the experimental model of the combined solar heat supply system in the mode of natural circulation of the heat carrier is effective for providing a building with a low-temperature carrier. The heat of the carrier is heated for an hour by an average of 15 °C.

4. Conclusions

It is established that for European countries the capacity of installations using renewable energy sources may exceed 300 million tons of oil equivalent by 2030. One of the most promising energy sources is solar energy, which is confirmed by the growth in the development of renewable energy for European countries. Since the territory of Europe has sufficient potential for renewable energy sources, this is a prerequisite for the widespread

introduction of solar collectors in the solar energy industry.
Experimentally determined thermal parameters of solar heating designed for the solar collector provided an opportunity to develop methods of engineering calculation, allowing even at the stage of implementation of the solar collector install, what would be the temperature of the heat carrier in the solar heating for its intended use. The heat of the carrier is heated for an hour by an average of 15 °C. According to engineering calculations of the solar heat supply system, it becomes possible to choose the most optimal mode of operation with the solar collector integrated into the translucent facade of the building based on the variable intensity of simulated solar radiation.
It is investigated that the amount of specific heat energy accumulated in the heat storage tank takes an increasing trend with the highest average maximum value of ≈490 kJ/m^2. The efficiency of the solar heat supply system with the developed solar collector integrated into the glass facade of the building is on average 46%.

Acknowledgements
This article was elaborated in the framework of the project VEGA 1/0697/17.

References

[1] Shapoval S., Venhryn I. (2014) *Prospects for using solar energy in Ukraine*. Young scientist, 7(2), 21-24. (in Ukrainian)

[2] Bockris J., Veziroglu T., Smith D. (2006) *Solar hydrogen energy*. The power to save the Earth. Macdonald Optima, London, 168. (in Ukrainian)

[3] Shapoval S. (2016) *The efficiency of combined solar collectors for energy efficient buildings*. Budownictwo o Zoptymalizowanym Potencjale Energetycznym 2(18), 81-86. (in English)

[4] Shapoval S. (2017) *Economic efficiency of application of solar window*. Czasopismo inzynierii ladowej, srodowiska i architektury journal of civil engineering, Environment and architecture, (2/II/17), 123-132. (in English)

[5] Lahutin O., Shmakov I., Nikulin Yu. (2008) *Albedo of the underlying surface according to the MODIS/Terra Spectroradiometer*. Sixth all-Russian open annual conference " Modern problems of remote sensing of the Earth from space», 12. (in Russian)

[6] Rekstad J., Meir M., Murtnes E., Dursun A. (2015) A comparison of the energy consumption in two passive houses, one with a solar heating system and one with an air–water heat pump. Energy and Buildings, 96, 149–161. (in English)

[7] Kazakov H. (2009) *Architecture of energy-saving solar houses*. Lviv Polytechnic, 84. (in Ukrainian)

[8] Kazakov H. (2012) *Solar houses: typological classification*. Bulletin of the National University "Lviv Polytechnic", 728, 235-240. (in Ukrainian)

[9] Shapoval, S., Zhelykh, V., Venhryn, I., Kozak, K., & Krygul, R. (2019). *Theoretical and experimental analysis of solar enclosure as part of energy-efficient house*. Eastern-European Journal of Enterprise Technologies, 2(8-98), 38-45. doi:10.15587/1729-4061.2019.160882 (in English)

[10] Hromova U. (2012) Environmental problems as prerequisites for the development of energy-saving technologies. Poultry Market. (in Russian)

[11] Pashchenko N. (2013) *Energy-efficient and energy-saving policy of Poland*. Reports of participants. Charitable foundation Havrylyshyna B., 8. (in Ukrainian)

[12] Basok B., Fareniuk H. (2014) Conceptual foundations for creating an experimental passive-type house (with a total area of 300 square meters). Building construction, 81, 233-243. (in Ukrainian)

[13] Basok B., Bozhko K., Bieliaieva T. (2014) Polyvalent heat supply system for an experimental house of passive type (300 m2) based on the use of renewable and alternative energy sources. Science and innovation. Institute of technical Thermophysics of the national Academy of Sciences of Ukraine, 6(10), 34-51. (in Ukrainian)

[14] Dvoretskyi A. (2013) *Design features of energy-efficient buildings in the South of Ukraine*. Construction, Materials science, Engineering, 68, 125-129. (in Russian)

[15] BP Statistical Review of World Energy 2019. (2019). *Centre for Energy Economics Research and Policy*, Heriot-Watt University, 61. (in English)

[16] Serheichuk O. (2008) Geometric modeling of physical processes when optimizing the shape of energy-efficient houses (Doctoral dissertation), Kyiv, 425. (in Ukrainian)

[17] Horobets V., Masiuk M. (2016) Development of a new design and mathematical modeling of heat and mass transfer processes for heat exchangers of ventilation systems of an energy-saving house. Energy and automation, 1, 90-98. (in Ukrainian)

[18] Chulkov D. (2007). *Patent of Ukraine 26650*. Kyiv: State Patent Office of Ukraine. (in Ukrainian)

[19] Shapoval, S. (2017). *Patent of Ukraine 113688*. Kyiv: State Patent Office of Ukraine. (in Ukrainian)

[20] Shapoval, S., Zhelykh, V., Spodyniuk, N., Dzeryn, O., & Gulai, B. (2019). The effectiveness to use the distribution manifold in the construction of the solar wall for the conditions of circulation. Pollack Periodica, 14(2), 143-154.

[21] Lukáč, P., Horbaj, P. (2015) Some notes to design of heating and hot water supply system like a power of low-temperature heating utilization in combination with solar collectors in housing and municipal sphere. Cassotherm 2015. TU v Košiciach, 321-331. ISBN 978-80-553-2438-8.

DOI: 10.1515/sspjce-2019-0016

Assessment of the economic value of irrigation water considering achieve main crops self-sufficiency: Case study Sharkia Governorate, Egypt

Hazem Eldeeb[1], Martina Zelenakova[2]*

[1] Water and Water Structures Eng. Department., Faculty of Engineering, Zagazig University, Zagazig 44519, Egypt, email: heldeeb@zu.edu.eg
[2] Department of Environmental Eng., Faculty of Civil Eng., Technical University of Kosice, Kosice 04200, Slovakia, email: martina.zelenakova@tuke.sk
* Correspondence: martina.zelenakova@tuke.sk; Tel.: +421-905-985-765

Abstract

The water shortage issue may put a spotlight over most of the Middle East region and push many nations to re-planning the water resources in various respects. Providing data on water's economic value assists policymakers make informed decisions regarding water distribution. Additionally, addressing the increasing demand for all uses and building the sustainable future of agricultural and water policies. The purpose of this article is to explore and evaluate the economic value of irrigation water in Sharkia Governorate, regarded one of Egypt's largest provinces. It also examines how to maximize the economic value of irrigation water, taking into account the self-sufficiency of main crops. Furthermore, consideration has been given to the political demands for the allocation, management and control of water resources. The simulation software Operational, Planning and Distribution Model (OPDM) was used to simulate through the studied province the accessible water distribution and crop yield. Moreover, it is used to judge the impact of irrigation water utilization and to check gross income. Furthermore, from a technical and economic point of perspective, the distinct suggestions were contrasted. The research evaluates the present crop pattern for wheat and cotton attaining a peak economic value of 1.23 EGP/m^3 and 0.98 EGP/m^3 of irrigation water for wheat and cotton respectively. Moreover, it reaches 0.41 EGP/m^3 for rice which considered one of the highest plants in water consumption. Finally, these findings may highlight some strategic crops future development.

Key words: economic value, irrigation water, water resources management, cropping pattern, Sharkia Governorate.

1 Introduction

Water is not a product or business asset, this is a resource that should be valued by mankind. Egypt's water resources are becoming insufficient. Surface water resources from the River Nile are generally totally explored, with full development of accessible revealed groundwater sources. Egypt is dealt with increasing water needs via a steadily growing inhabitants, higher

living standards and agriculture initiatives and regulations [1]. Agriculture is typically a river basin's hugest water-consuming enterprise, so its climatological-risk water-use plan is related to sustainable water resource productivity throughout the region [2].
More than a million individuals a year are presently growing the population in Egypt. Improved agency and management processes of water adequacy, assignment and use are mostly recommended important procedures to creating appropriate use of the water available. For most places, the key constraint is the ability to produce visionary water management strategy, together with the required legislation and administration to promote it.
This will no longer be feasible for Egypt to reach its boundaries of accessible water and Egypt will have to face variable supply circumstances. The ideal use of water is therefore one of the ways in which this issue can be addressed; the financial or economic value of water is one of the most significant variables to be concentrated. Government policies are aimed for reducing the consumption of agricultural water and rationalizing water consumption taking into account social and environmental issues.
Agriculture consumes the largest quantity of water available in Egypt, with its share slightly below 85% of complete water demand. The agricultural sector in the Egyptian economy contributes approximately 13.22% to gross national product and propositions approximately 34% of total jobs. Municipal water demand was estimated at 9.0 billion cubic meters (BCM), with roughly 95% of the Egyptian population relying on water distribution networks, Ministry of Water Resources and Irrigation [3,4].
The value of water represents the financial, cultural and environmental values of society [5]. Water's economic or financial value depends on both the customer and the use. Since it is scarce and can be used in distinct ways, water can have a strong economic value. Knowledge of the economic value of water encourages policymakers to make knowledgeable water decisions development, distribution and use in facing its increasing scarcity when increasing requirements for all uses are made [6]. To sum up, precise estimates of the economic value of water are needed for the rational distribution of water shortages across places, uses, customers and timeframes [6].
The present study's primary goal is to scrutinize the financial results of irrigation water and improve the environmental and social efficiency of irrigation water at Sharkia Governorate, one of Egypt's largest provinces.

2 Literature review

The River Nile is Egypt's primary water source, with an assigned annual flow of 55.5 BCM/year under the 1959 Nile water agreement. It is estimated that internal renewable surface water resources are 0.5 BCM/year. This gives up to 56 BCM /year of complete real renewable surface water resources. It is estimated that internal renewable groundwater resources are 1.3 billion BCM/year.
The overlap between surface water and groundwater is regarded negligible, making the country's complete real renewable water resources 57.3 BCM/year [7]. There are countless earlier water resource management studies in Egypt. A short research was provided on cost recovery in water systems [8]. In addition, the water valuation research was introduced, moreover, a demand management tool was submitted in Egypt [5]. Additionally, there are many water policy integration research in Egypt [7,9]. Water value should represent society's

financial, environmental and cultural values [5]. While there is infinite supply of water, it is economically free. Obviously, water economic value estimates are crucial if scarce water is to be allocated efficiently and equitably [6].
Water is a tremendous resource. This implies that its economic value tends to be relatively small per unit weight or quantity. Its transport therefore needs a high cost per volume unit and is unless a high marginal value can be attained, it is often not economically viable over lengthy distances. The abstraction, storage and any transportation expenditures tend to be exceptional compared to the small economic value of using an extra water unit. This can generate water values particular to the location [10].
Increasing the development of water based on food consumption and optimizing the allocation of water resources were studied [11]. In addition, an optimization model was developed in terms of plant water productivity and a mathematical model was developed to maximize income per unit of water based on optimum crop pattern [11].
Digital Water Resources Management (WRM) depictions have become increasingly accessible in the form of digital models (DMs) over the past twenty years. It is quicker to use computers and extract information from digital models, providing more reproducible readings than traditional manual methods. A try to quantify the potential for runoff in all India's basins using remote sensing data [12] was used. The SCS technique has been used. Complex map of hydrological soil cover has been acquired by incorporating map of land use and map of soil type. In addition, GIS was used as an instrument to assess the potential of surface water [13].
This article analyzes the water policy planning of the region and suggests highlighting the features of this planning attempt in the governorate of Sharkia. Including irrigation and drainage processes, an extensive water resources map was prepared. Furthermore, consideration was given to the political demands for the allocation, management and control of water resources.
The Operational, Planning and Distribution Model (OPDM) was used throughout the studied province to simulate the accessible distribution of water and crop yield. Furthermore, the gross income has been researched. Such an assessment is important because there are currently very restricted and mainly undocumented knowledge of Egyptian water economic value.
Many suggestions have been explored to show the model's use and to show the current water resource management scenario. Finally, the current water financial values are described and assessed for the primary crops.

3 Collected data utilized

On the basis of information supplied by the Ministry of Irrigation and Water Resources (MIWR); Irrigation Sector (IS), Ministry of Agriculture and Land Reclamation (MALR), the possible distinct conditions were created.
The information includes the present crop pattern, water requirements for each crop, complete cost of each crop being cultivated. The costs include preparation of land, seeds, fertilizers, irrigation or agricultural services, pest control, harvesting, transportation of crops and the costs of public expenditure and total income per feddan for each crop.

4 Model description

The Operational, Planning and Distribution Model, OPDM, is one of the most advanced software developed in complicated canal and drainage networks to simulate water distribution and crop yield reaction. Based on the given plant patterns and weather data, the OPDM is used to assess plant water requirements.
The modeled water quantities are transmitted through a primary main canal scheme, groundwater aquifers, downstream streams, and open drains.

4.1 Theoretical approach

The OPDM model is used in this paper to calculate theoretically different parameters affect the irrigation water consumption. These parameters include wind speed, leaching factor and salinity as follows [14]:

- *Wind speed*

$$U_2 = 4.852U_z/\ln(z - 0.08/0.015) \quad (1)$$

Where: U_2 is the wind speed at 2.0 m (m/s); and U_z is the recorded velocity (m/s) at z (m) above ground surface.

- *The leaching factor*

$$LF = EC_{iw}/EC_{dw} = D_{dw}/D_{iw} \quad (2)$$

Where: LF is the leaching factor (from 0 to 1.0); EC_{iw} is the irrigation water electrical conductivity (dS/m); EC_{dw} is the drainage water electrical conductivity, or deep percolation, water (dS/m); D_{dw} is the depth of drainage water (m); and D_{iw} is the depth of infiltrated water from the soil surface (m).

- *The deficit yield reduction*

$$Y_{rel} = 100\prod_{i=1}^{n}(ET_a/ET_p)_i^{\lambda_i} \quad (3)$$

Where: Y_{rel} is the relative yield (%); ET_a is actual transpiration (mm/day); ET_p is the maximum potential transpiration; λ is a fitted exponent (a calibrated value); and the subscript i refers to the growth stage (the OPDM uses five growth stages, so, n = 5).

- *The salinity output, plant development stage, soil fertility, soil water content and salinity content impact on crop yield is modeled through the approximate equation:*

$$Y_{rel} = 100 - B_s(EC_e - A_s) \quad (4)$$

Where: Y_{rel} is the relative yield (%); A_s is the threshold salinity (dS/m); B_s is the rate at which relative crop yield declines with increasing salinity, beyond A_s (% per dS/m); and EC_e is the salinity of the soil water extract (dS/m).

The Penman-Monteith equation's distinct types apply to the combined technique. The combined technique generates some of the most complicated and comparatively precise ET_o formulas. The Penman-Monteith equation is:

$$ET_o = \frac{0.408\Delta(R_n - G) + \frac{890\gamma U_2(e_a - e_d)}{T+273}}{\Delta + \gamma(1 + 0.339U_2)} \quad (5)$$

4.2 Current economic value of water

In this article, the economic value means economically the quantity of crop productivity (the net income of some grown region; in our case Sharkia Governorate) over the quantity of agricultural water resources for each plant.
An important indicator, which is the average value per unit of water used, can be considered the economic value. Productivity, however, is a performance measure defined as the yield and entry proportion. For the entire scheme or a single component, production can be evaluated. Two production indices could account for all or one of the outputs of the production system [15]:

- *Total production:* the proportion of the complete production over the complete input;
- *Partial production:* the proportion of the complete production over of one or more items within system.

Water's economic value is a partial production variable that estimates how water is converted into economic value by the processes. It can be acknowledged as its overall concept:

Economic value = Output Derived from Water Use (Net income)/Water Input

It is possible to organize and present economic value in several distinct ways. Typically, however, they can include two separate parts: total income and total expenses. The measures needed to evaluate these segments in detail are as follows:

- *Total Income (TI)*

Estimating complete output is the first stage in estimating total income. Total output includes the primary crop yields, by item, and the related rates.

$$TI_i = P_i \times D_i \quad (6)$$

Where: P_i = crop price (i) (EGP/Ton); D_i = crop production (i) (Ton).

- *Total cost (TC)*

Total cost includes preparing of soil, crops, fertilizers, irrigation, agricultural facilities, pest control, harvesting, storage of crops, and costs of government expenditures. The variable cost calculated by the related rates multiplying the amounts of each entry.

$$TC_i = C_i \times Q_i \quad (7)$$

Where: C_i = crop cost (i) (EGP /Ton); Q_i = crop production (i) (Ton).

- *Net Income (NI)*

Net income calculated as the difference between total income; total complete cost.

$$NI_i = TI_i - TC_i \quad (8)$$

Where: TI_i = Total crop income (i) (EGP); TC_i = Total cost of crop (i) (EGP).

- *Water input (WI)*

The water input can be considered as quantity per cubic meter. Input of water is the water requirements for crops multiplying by the area planted.

$$WI_i = W_i \times A_i \quad (9)$$

Where: W_i = crop water duty (i) (m^3/Feddan); Ai = crop planted are (i) (Feddan).

- *Economic value of water (EV)*

The present research calculates the economic value of irrigation water by implementing value-added technique:

$$EV_i = NI_i/WI_i \quad (10)$$

Where: EV_i = crop net revenue (i) (EGP); WI_i = crop water requirements (i) (m^3).

5 The case study

5.1 General information

The irrigation area at the Governorate of Sharkia is chosen as the case study. The boundaries of Egypt governorates are presented in Figure (1-a) while the case study, Sharkia governorate, is shown in Figure (1-b).

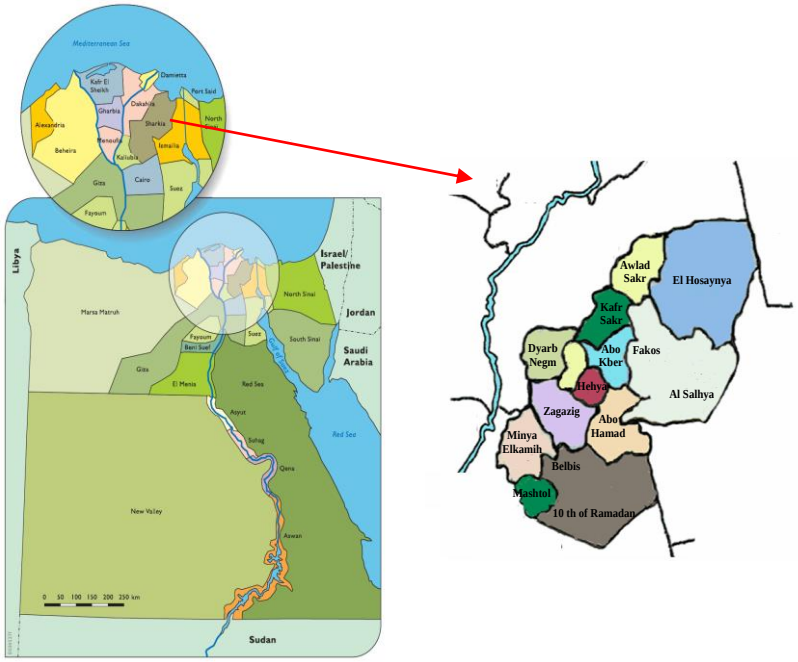

(a) (b)

Figure 1: The boundaries (a) Egypt governorates [4] (b) Sharkia governorate

The project area is located at latitude 32.5° N and 30° longitudinal at an elevation of 10m above the mean sea level. The speed of wind used to calculate the evapo – transpiration is the

speed at 2m above ground. A network of irrigation channels feeds the region. In addition, the surplus water is discharged through open drain network. Some water, together with surface water, is drawn from an aquifer and used for irrigation.

5.2 Canals and drains alignment

Sharkia Governorate's waterways network is composed of open diches, shown in Figure 2 as presented in OPDM model. The project area is about 972642 Feddan, it is divided into three departments (East Sharkia, West Sharkia and Salhya), as presented in Table 1.

Table 1: Sharkia Governorate departments, canals and drains

Department	Divisions	Area (Feddan)	Canals length (km)	Drains length (km)
East Sharkia	5	211233	789	361
West Sharkia	5	303851	1144	798
Salhya	7	457558	700	212
Total	17	972642	2633	1371

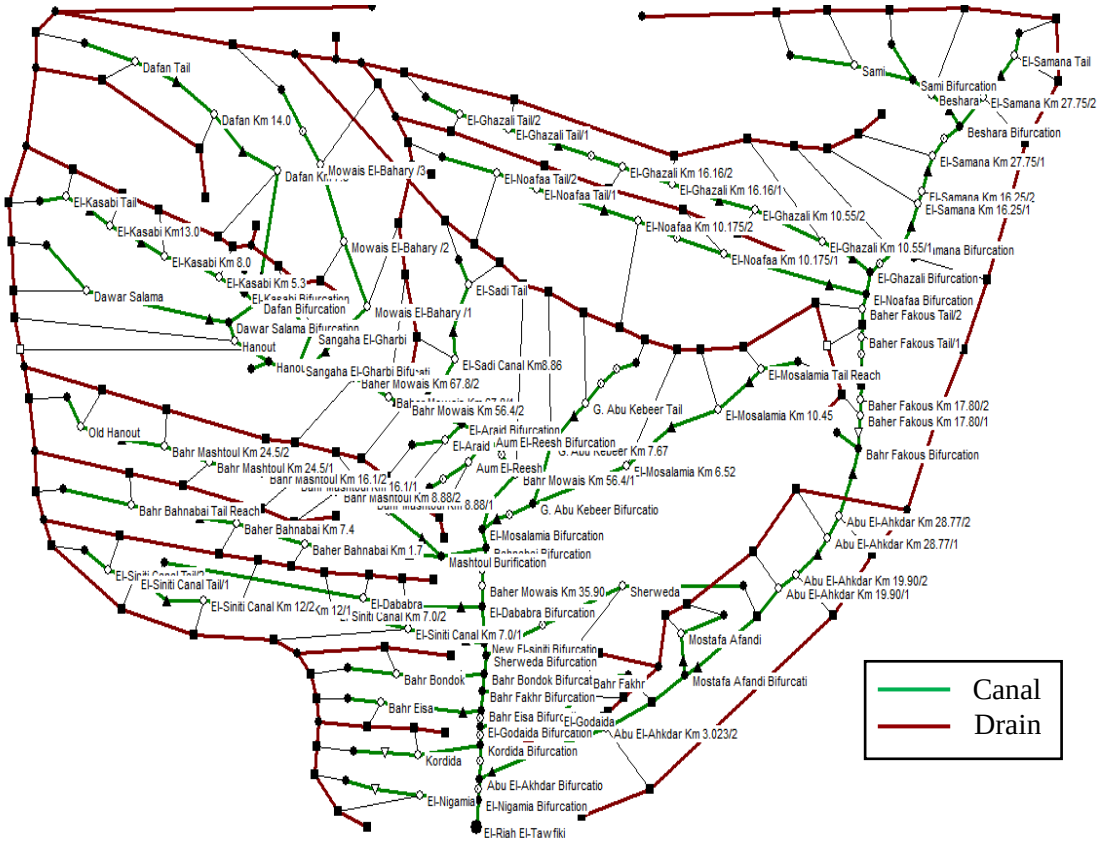

Figure 2: A schematic view of canals and drains in Sharkia governorate

The cropping pattern is simulated including the following crops (wheat, clover, cotton, rice, maize, beans, gardens, vegetables and medical plants).

The cropping pattern indicates the yearly sequence and spatial arrangements of crops. Furthermore, the cropping pattern reflects the comparative status of specific crop importance to the total cultivated areas.

5.3 Current water resources

The present water resources in the governorate of Sharkia are displayed including the parameters of surface and groundwater as shown in Table 2. The main source of surface water is El-Riah El-Tawfiki canal. Furthermore, the groundwater sources are governmental and non- governmental wells.

Table 2: Water resources quantity and quality

Variables	Quantity
Surface water quantity (m^3/sec)	138.9
Surface water salinity (ds/m)	0.85
Groundwater quantity (Mm^3/year)	500
Groundwater salinity (ds/m)	0.85

6 Analysis of the results

Running the simulation process, the following, Figure 3, shows evapotranspiration calculated from simulation model per crop type. It is obvious that maize and rice are the largest irrigation water consumption as they reach 465 and 410 Mm^3 with percentages 21.7% and 19.1% of the total water consumption respectively during the year of research. Moreover, the percentages of water consumption of the other crops reach 16.3%, 13.2%, 10.3%, 9.7% and 9.7% for clover, cotton, wheat, vegetables and others respectively.

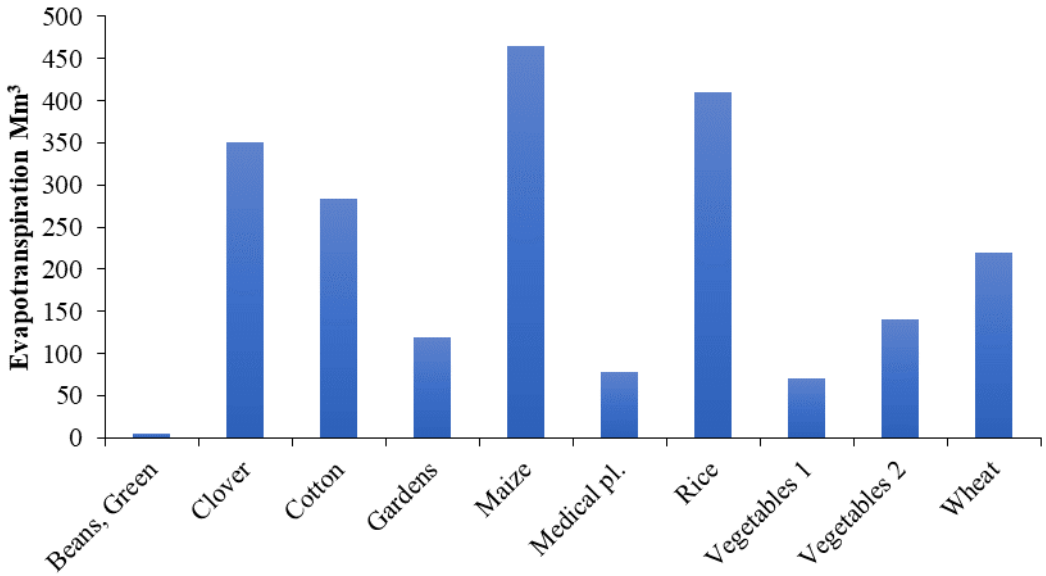

Figure 3: The evapotranspiration Mm^3 by crop type

Table 3 shows the total gross income by crop type. The total gross income of Sharkia Governorate is 942.955 Million EGP. Moreover, wheat and cotton are the greatest crops in gross income by about 31.4% and 29.3% of the total income respectively. Furthermore, the gross incomes for maize and rice are 1.7% and 17.4% of the total income respectively. Thus, the highest water consumption crops, maize and rice, are not the greatest income crops.

Table 3: The gross income by crop type

Crops	Gross Income (million EGP)
Beans, Green	0.62
Clover	92.99
Cotton	276.12
Gardens	26.51
Maize	16.16
Medical pl.	7.72
Rice	164.82
Vegetables 1	8.72
Vegetables 2	62.27
Wheat	295.74

7 The economic value of water

In this paper the net income expressed as the total crop price subtracts the cost of production. The economic value of irrigation water at Sharkia governorate for each crop could be represented in Table 4. Furthermore, the previous analysis and the current table indicate that wheat and cotton are the highest crops in the economic value of irrigation water as it reaches 1.23 EGP/m^3 for wheat and 0.98 EGP/m^3 for cotton.

Table 4: Economic value of irrigation water

Crops	Economic value (EGP/m^3)
Beans, Green	0.21
Clover	0.27
Cotton	0.98
Gardens	0.19
Maize	0.03
Medical pl.	0.10
Rice	0.41
Vegetables 1	0.13
Vegetables 2	0.42
Wheat	1.23

Figure 4 describes the economic value of crop irrigation water arranged from highest to lowest, wheat is the highest with 1.23 EGP/m^3 of irrigation water while maize is the lowest with 0.03 EGP/m^3 although it is the highest water consumption crop.

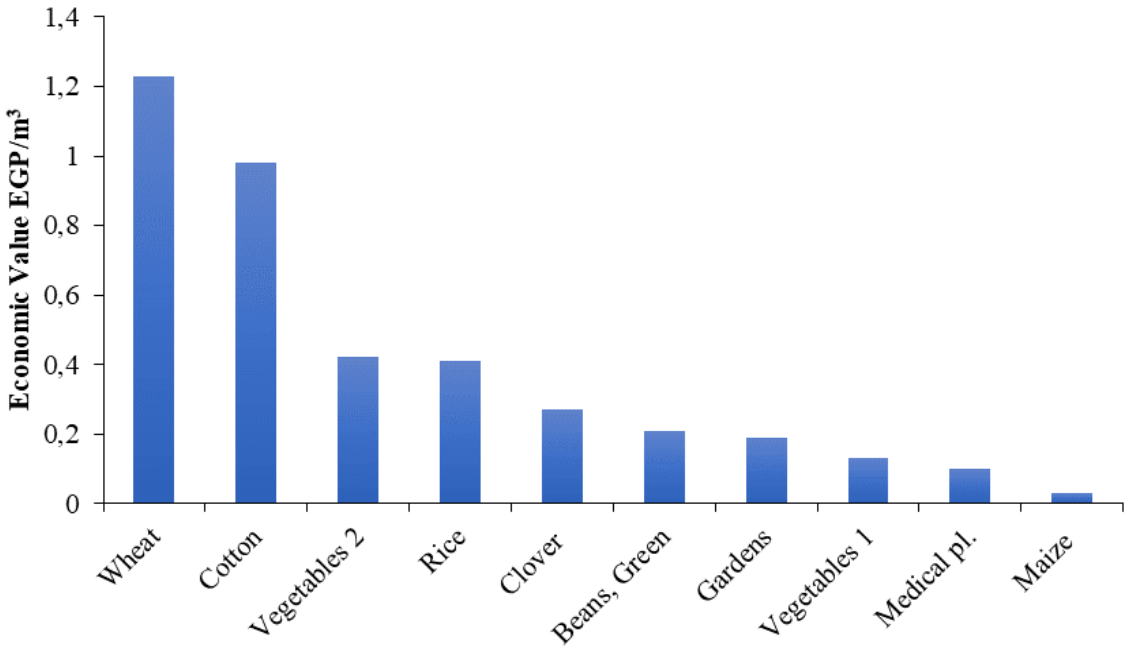

Figure 4: The economic value EGP/m^3 by crop type

From the figure it could also observed that the economic value of irrigation water for maize is 0.03 EGP/m^3, and for rice is 0.41EGP/m^3.

8 Conclusion

The present paper's primary goal is to scrutinize the financial outcomes of irrigation water. Moreover, the political requirements for distribution, managing and dominance of the water resources have been taken into consideration. Water's economic value helps policymakers making informed decisions about water supply. Operational, Planning and Distribution Model (OPDM) has been used to monitor the water distribution and crop yield. Moreover, simulations of surface and groundwater under the current quantities and qualities are conducted, also their reflective impact on gross income are investigated. Furthermore, the study assesses the current cropping pattern for the government. It is obvious that maize and rice are the largest irrigation water consumption as they reach 465 and 410 Mm^3 with percentages 21.7% and 19.1% of the total water consumption during the year of research. Moreover, wheat and cotton are the greatest crops in gross income by about 31.4% and 29.3% of the total income. It is concluded that maximum economic values of irrigation water are 1.23 EGP/m^3 and 0.98 EGP/m^3 for wheat and cotton respectively. Furthermore, the gross

incomes for maize and rice are 1.7% and 17.4% of the total income respectively. Thus, the highest water consumption crops, maize and rice, are not the greatest income crops. Finally, these results may highlight the future production of some strategic crops.

Acknowledgements

The authors expressed their sincere gratitude for the available facilities of the Department of Water and Water Structures Engineering, Faculty of Engineering, Zagazig University.

References

[1] Ayman, A., Graham E. & Mohsen A. (2013). Water use at Luxor, Egypt: consumption analysis and future demand forecasting. *Environ Earth Sci*, DOI 10.1007/s12665-013-3021-8.

[2] Zhang J., Bai M., Zhou S. & Zhao M. (2018). Agricultural Water Use Sustainability Assessment in the Tarim River Basin under Climatic Risks. *Water*, No. 10, 170; doi:10.3390/w10020170.

[3] MWRI (2013). Adaptation to Climate Change in the Nile Delta through Integrated Coastal Zone Management. Ministry of Water Resources and Irrigation.

[4] MWRI (2005). National Water Resources Plan for Egypt 2017. Available at http://extwprlegs1.fao.org/docs/pdf/egy147082.pdf, accessed [10-11-2018].

[5] El-Atfy H. & Kotb T. (2004). Water Valuing: a Tool for Demand Management in Egypt. Workshop on Water Demand Management in Egypt, Framework of the 38th Meeting of the Advisory Panel Project on Water Management, Nigmegen, The Netherlands.

[6] Ward A. & Michelsen A. (2002). The economic value of water in agriculture: concepts and policy applications. *Water Policy*; 4:423–46.

[7] NWRP (2003). National Water Resources Plan (2003) Facing the Challenge. Outline of a Draft Strategy, NWRP Discussion Paper No. 3, Egypt.

[8] Abdel-Aziz Y. (2002). Cost Recovery in Water Systems, Workshop on Financing and Cost Recovery of Agriculture Water Systems. Advisory Panel Project on Water Management, Haarlem, the Netherlands.

[9] Shalaby A., Sadek T., Kotb T. & Mostafa M. (2003). Inter-ministerial Water Policy Integration. *Water Policy Advisory Unit*, Report No. 71, Ministry of Water Resources and Irrigation, Egypt.

[10] Young R. (1996). Measuring economic benefits for water investments and policies. 1–119. Washington: World Bank Technical Paper 338. https://doi.org/10.1596/0-8213-3745-9.

[11] Nimah M. (2004). Maximizing irrigation scheme water productivity based on optimum cropping pattern. *Nat Water Res Center J*.

[12] Mohan Z., Ray S. S. & Panigrahy S. (2005). Analysis of runoff pattern for all major basins of India derived using remote sensing data. *Current science*, Vol. 88, No. 8, 25.

[13] Anandan P. S. & Venkatesh G. (2005). Surface water estimation using GIS. Proceedings of the National seminar innovative techniques for sustainable development of water resources, March 24-25.

[14] USU (1996). Operation and planning distribution model (OPDM). Soft User's Guide, Ver. 2.02, Department of Biology and Irrigation Engineering, Utah State University (USU), Logan, UT.

[15] Hosni H., El-gafy I. K., Ibrahim A. H. & Abowarda A. S. (2014). Maximizing the economic value of irrigation water and achieving self sufficiency of main crops. *Ain Shams Engineering Journal*, No. 5, 1005–1017.

DOI: 10.1515/sspjce-2019-0017

Assessment of two different methods of calculating a heating demand

Peter Turcsányi, Anna Sedláková

Technical University of Košice, Slovakia
Civil Engineering Faculty, Institute of Architectural and Indoor Engineering
e-mail: peter.turcsanyi@tuke.sk, anna.sedlakova@tuke.sk,

Abstract

Phenomenon of today´s era is lowering overall energy performance and greenhouse gas emissions. European Union and its members came from an "uncontrollable" fossil fuel usage to an era of dependence reduction from fossil fuel usage. EU industry is now in era of utilizing renewable energy sources. Construction industry is responsible for 40% of total energy performance of EU; hence the great emphasis on energy effective design on new buildings as well as importance on energy effective renovation of already constructed buildings. Effort on lowering total energy performance in construction industry has signed on research on new project solutions, new insulation materials and new building services technologies which are maximizing energy gain from renewable energy sources. Simulation software and different engines are more than helpful tool when predicting building thermal behaviour. That is why simulation software is used more often in the process of designing energy efficient buildings or in the process of energy performance optimization of existing buildings. simulation and analytics itself, is dealing with simulation of chosen buildings (family houses) on heating demand based on the newest knowledge of constructions and materials. Results of heating demands of different family houses were confronted against heating demands calculated according national standards – using non-variable conditions. Next, the differences between two calculation approaches were characterized in percentages.

Key words: heating demand, simulation software, family house

1 Introduction

This paper assesses two different family houses on the heating demand using dynamic simulation software tool DesignBuilder v4 and using calculation according national directives and standards (with permanent weather condition). Non-dynamic calculation using national directives and standards is still used more frequently than dynamic simulations. The benefit of using dynamic simulation when calculating heating demand is, that dynamic simulation is the closest method to observe real life behavior of the family house. Currently, there are more than 400 applications that can be applied to analyzing building energy and thermal simulation [1]. Optimization of energy use is up to date theme, and many publications are being written about it such as [5][6][8][7][9].

The purpose of this paper is to determine the difference between two different methods of calculating heating demand of the two assessed family houses. The results of this determination can be used in a design phase of the future projects.

2 Climate and location

Two family houses are located in Košice – Slovakia. Both houses are two-stories family houses that represent a typical type of residential buildings built in this area. Buildings are based on concrete footing foundation.

2.1 Family house A

Figure 1: Family house A

The family houses envelope was designed from materials with high thermal capacity insulated from outside with a thick layer of polystyrene (ETICS system) to minimize the heat loses during the heating period as well as to prevent the heat infiltration during the summer period. Roof structure creates unconditioned space between insulated ceiling and top of the roof. Transparent parts of the building envelopes were designed to meet the national standards and energy criteria.

Table 1: Thermo-technical parameters of the family house A

Shape factor (A/V ratio)	0.78 1/m
Volume of building space	726.18 m^3
Total heat transfer surface	569.48 m^2
Total floor area	222.09 m^2
Wall U-Value	0.168 W/(m^2.K)
Insulated ceiling U-Value	0.119 W/(m^2.K)
Ground floor R-Value	5.302 (m^2.K)/W
Wood-aluminum U-Value Internorm HF 350	0.60 – 0.95W/(m^2.K)

2.2 Family house B

Figure 2: Family house B

The family houses B envelope was designed from the same materials with high thermal capacity insulated from outside with a thick layer of polystyrene (ETICS system) to minimize the heat loses during the heating period as well as to prevent the heat infiltration during the summer period.

Table 2: Thermo-technical parameter of the family house B

Shape factor (A/V ratio)	0.62 1/m
Volume of building space	921.98 m^3
Total heat transfer surface	569.48 m^2
Total floor area	232.14 m^2
Wall U-Value	0,148 W/(m^2.K)
Insulated ceiling U-Value	0.123 W/(m^2.K)
Ground floor R-Value	4.38 (m^2.K)/W
Rehau geneo plastic window	0.75 – 0.95W/(m^2.K)

2.3 Climate and weather conditions

Dynamic conditions according to [2], used in dynamic simulation software DesignBuilder v4 to calculate heating demand:

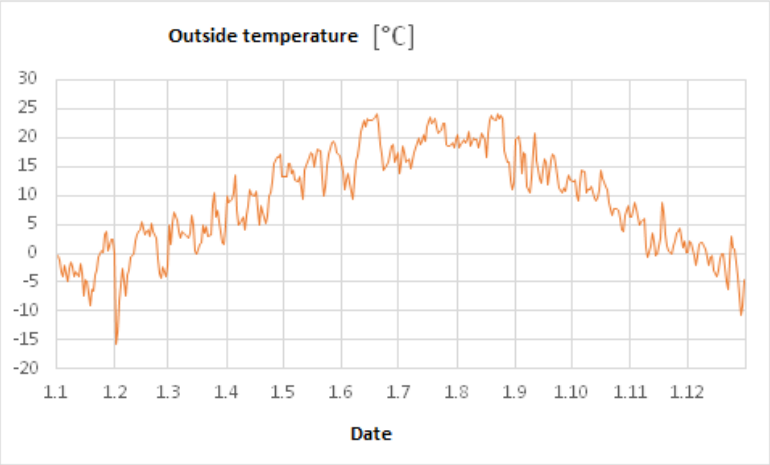

Figure 3: Outside temperature during simulated year

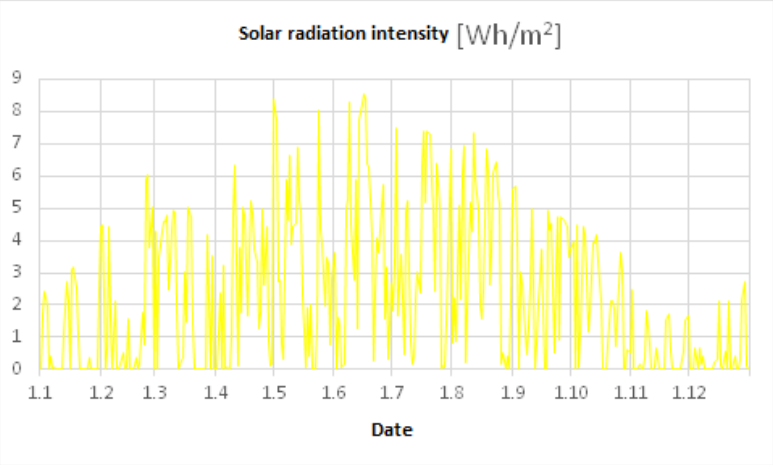

Figure 4: Solar radiation intensity during calculated year

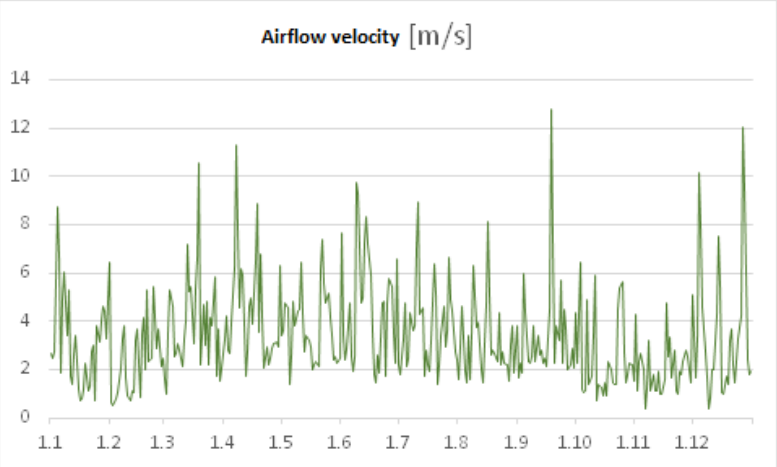

Figure 5: Airflow velocity during calculated year

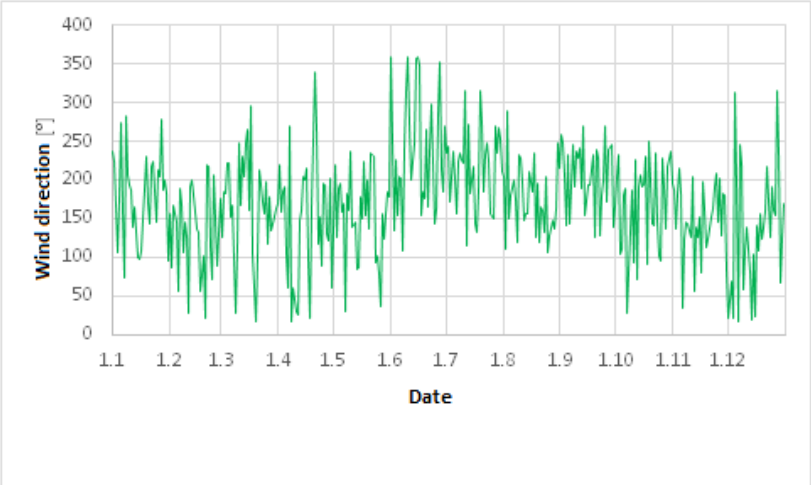

Figure 6: Wind direction data used in simulation

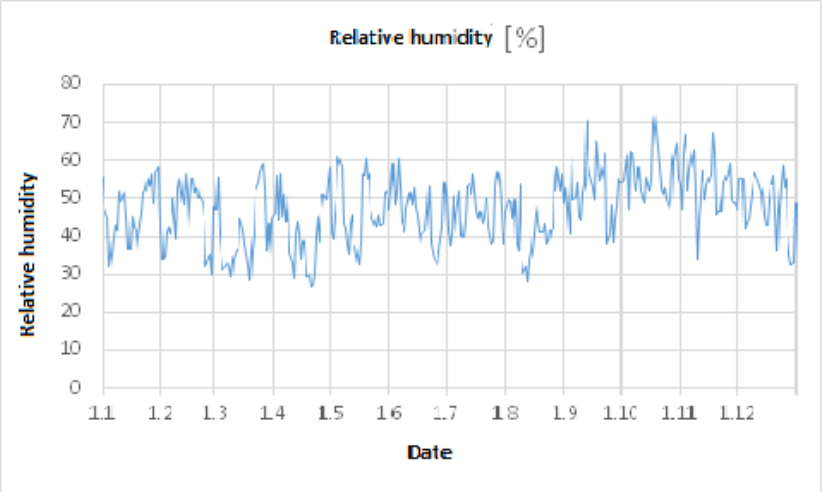

Figure 7: Relative humidity

Non-dynamic conditions used in the heating demand calculation according to national standard STN 730540:2012 Part 1-3 [4] and STN EN ISO 13 790 on Energy Performance of the Buildings [3]:

Interior temperature θ_{int}= 20°C
Interior relative humidity ϕi = 50%
Outside temperature θ_e= -13°C (mean outside /throughout the year/ temperature 3,86 °C)
Outside relative humidity ϕe = 84%

3 Results

Results of heating demand calculated using dynamic simulation software and calculated using national standards and directives (non-dynamic conditions) are displayed in the graphs and tables below.

3.1 Family house A

Simplified model of the family house A was put into the dynamic simulation software interface DesignBuilder v4.

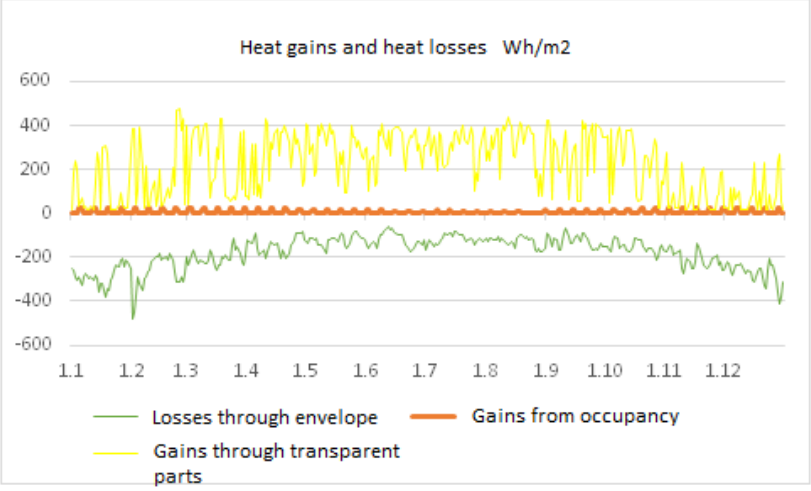

Figure 8: Heat gains and heat losses_family house A

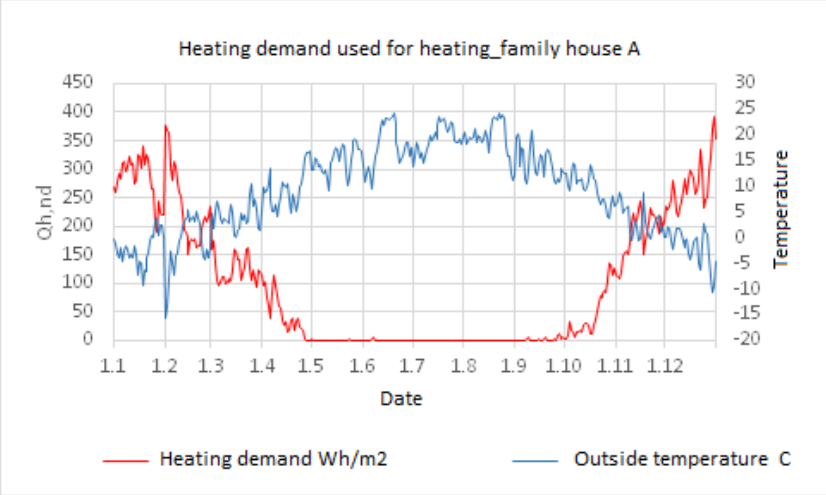

Figure 9: Heating demand throughout the simulated year_family house A

Calculation of heating demand according national standards and directives – monthly method:

Table 3: Calculated heating demand – monthly method – family house A

$Q_{h,nd,1}$
43,78 kWh/m^2.a

3.1.1 Partial conclusion

Model of the family house A was put into the dynamic simulation software DesignBuilder v4 interface with the parameters according Tab. 1.

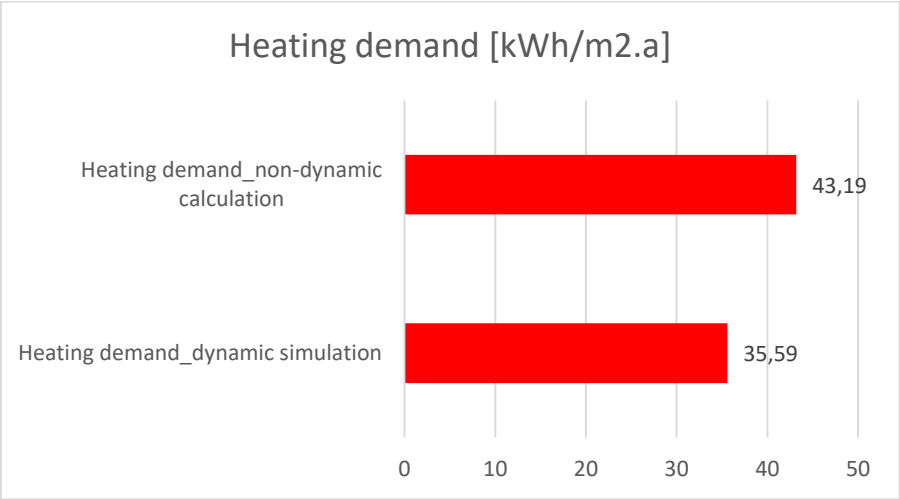

Figure 10: Difference between heating demand calculated with dynamic simulation tool and non-dynamic calculation_family house A

Yearly heating demand of the family house A, calculated according to national standards and directives with the monthly method, is 43,78 kWh/m^2.a. On the other hand, calculated heating demand using dynamic simulation software DesignBuilder v4 is 35,59 kWh/m^2.a.
As it can be seen from Fig. 10, the difference between two different types of heating demand calculation is 7,6 kWh/m^2.a, which represents the difference of 23%.

3.2 Family house B

Simplified model of the family house B was put into the dynamic simulation software interface DesignBuilder v4.

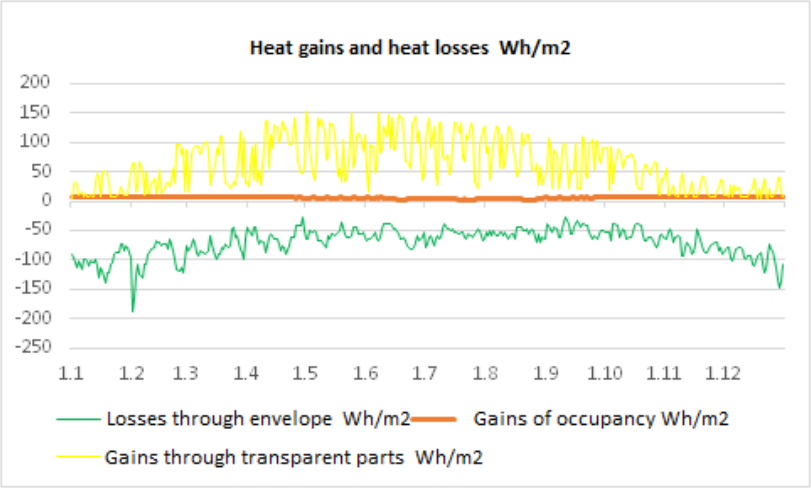

Figure 11: Heat gains and heat losses_family house B

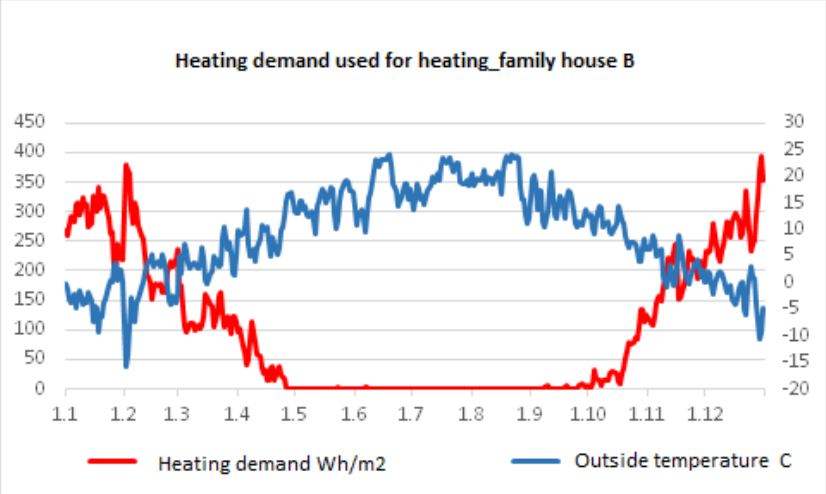

Figure 12: Heating demand throughout the simulated year_family house B

Calculation of heating demand according national standards and directives – monthly method:

Table 4: Calculated heating demand – monthly method – family house A

$Q_{h,nd,1}$
43,19 kWh/m^2.a

3.2.1 Partial conclusion

Model of the family house A was put into the dynamic simulation software DesignBuilder v4 interface with the parameters according Tab. 2.

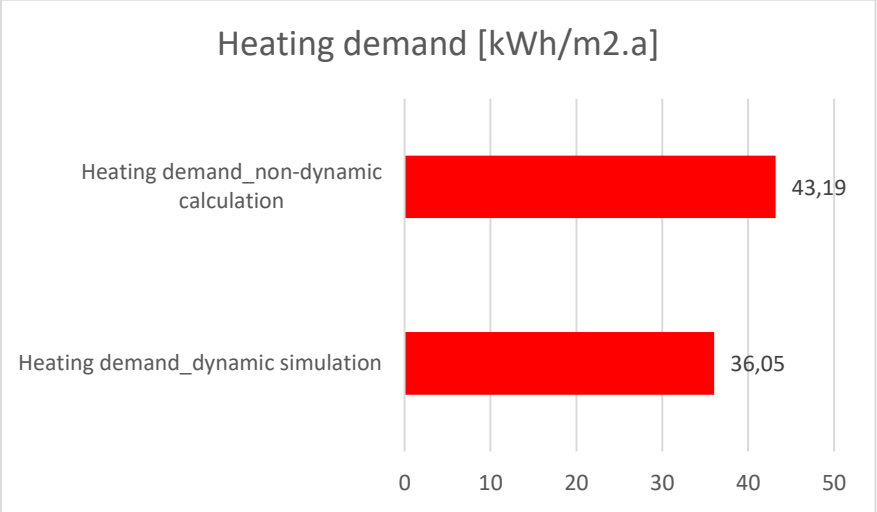

Figure 13: Difference between heating demand calculated with dynamic simulation tool and non-dynamic calculation_family house B

Yearly heating demand of the family house B, calculated according to national standards and directives with the monthly method, is 43,19 kWh/m^2.a. On the other hand, calculated heating demand using dynamic simulation software DesignBuilder v4 is 36,05 kWh/m^2.a.
As it can be seen from Fig. 13, the difference between two different types of heating demand calculation is 7,14 kWh/m^2.a, which represents the difference of 19,80%.

4 Conclusion

This paper is determining the difference between two different approaches of calculating heating demand of the family houses.

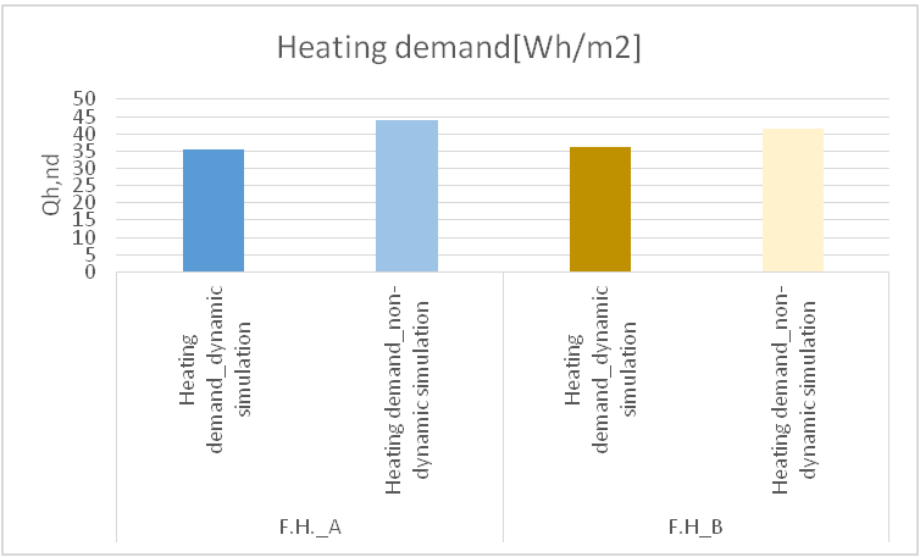

Figure 14: Difference in heating demand of assessed family houses

First method is dynamic simulation method, when dynamic data are being applied on the calculation. This method has great potential in the future as it can predict a close-to-real energy performance of the building in the pre design stage of a project. The disadvantage of this method is that simulation software is expensive and not many design companies and studios can afford it, thus most of project companies and studios are using heating demand calculation using non-dynamic calculation according national standards and directives.
This paper can help those designers, who cannot afford investing into simulation software on when calculating heating demand of a building. According to this assessment, the difference between dynamic simulation and non-dynamic calculation of the heating demand is 21,40 % /based on two family houses calculation/. To sum it all, when calculating heating demand using non-dynamic calculation method – according to national standards and directives – this 21,40% difference can be applied to calculations, to reach the close-to-real heating demand, which can be used in further energy calculations.

Acknowledgements

This work was supported by the Grant Agency of the Slovak Republic No. 1/0307/16.

References

[1] Energy Efficiency and Renewable Energy (EERE). Building Energy Software Tools Directory, U.S. Department of Energy. Available online: http://apps1.eere.energy.gov/buildings/tools_directory/(accessed on 18 January 2013).

[2] Fanger, P.O. *Thermal Comfort, Analysis and Applications in Environmental Engineering*; McGraw-Hill Book Company: New York, USA, 1970.

[3] STN EN 13790: Energetická hospodárnosť budov. Výpočet potreby energie na vykurovanie a chladenie, 2008.

[4] STN 73 0540: 2012 Tepelná ochrana. Tepelnotechnicke vlastnosti stavebných konštrukcií a budov. Časť 1 až 3. (júl 2012).

[5] Manuál energeticky úsporné architektúry. Vydavatel: Státní fond životního prostředí ve spolupráci s Českou komorou architektů. ISBN: 978-80-904577-1-3.

[6] Europe´s buildings under the microscope. A country – by – country review of the energy performance of buildings. Buildings Performance Institute Europe (BIPE). October 2011. ISBN: 9789491143014 http://www.bpie.eu/eu_buildings_under_microscope.html

[7] P TURCSANYI, P.: Výskum určujúcich parametrov energeticky efektívnych budov pomocou dynamickej simulácie. Dizertačná práca. TU Košice. 2019.

[8] HOPFE, CH.,J.: Uncertainty and sensitivity analysis in building performance simulation for decision support and design optimization. Dissertation work.

[9] SMITH, S.,T. : Modelling thermal loads for a non-domestic building stock. Associating a priori probability with building form and construction – using building control laws and regulations. Dissertation work.

DOI: 10.1515/sspjce-2019-0018

Fire resistance properties of some selected tropical timber species from South-western Nigeria after fire exposure

Oluwaseun Adedapo Adetayo[1], Bamidele Ibukunolu Olugbemi Dahunsi[2]

[1]Department of Civil Engineering, Federal University Oye Ekiti, Nigeria
[2]Department of Civil Engineering, University of Ibadan, Nigeria
email: oluwaseun.adetayo@fuoye.edu.ng; tayo.seun4real@gmail.com

Abstract

The research investigated changes in post fire density and strength properties of Nigerian wood species used for construction. The selected species are: *Terminalia superba* (Afara), *Milicia excels* (Iroko), *Nauclea diderrichii* (Opepe), *Khaya ivorensis* (Mahogany), *Mansonia altissima* (Mansonia), *Tectona grandis* (Teak). Densities and strength properties of the species were determined at Moisture Contents (MC) of 9.0, 12.0, and 15.0%. Species were exposed to fire at various temperature ranges. The results revealed that at 9, 12 and 15%MC, Opepe had the highest density values of 630±28.85kg/m³, 686±22.64kg/m³ and 752±17.22 kg/m³ respectively. At 9%MC, Mahogany had the lowest density (439±10.58kg/m³) while at 12 and 15%MC, Afara had the lowest density values of 444±4.18kg/m³ and 469±7.07kg/m³ respectively. Post fire exposure revealed that Afara had the highest percentage loss in density 29.2% and strength properties, while both Iroko and Mahogany exhibited the lowest percentage loss in both density and strength properties.

Key words: Nigeria wood, wood density, strength properties, fire resistance

1 Introduction

Many buildings and civil engineering works are at high risk of fire. Therefore, accurate prediction of behaviour of the structures subjected to fire is of primary importance for the evacuation of persons, as well as for the safety of rescue teams [1]. Timber is natural and renewable. It has a high strength to weight ratio and is easy to work with, making it especially useful where only basic technology and procedures are available [2]. The history and development of timber structures is an extensive topic. Timber has been used in the construction of buildings, bridges, machinery, war engines, civil engineering works and boats, etc., since mankind first learnt to fashion tools [3]. In many parts of Europe and North America, wood products of various types are used in framing, flooring, siding and even foundation work in single family residences, apartment, commercial and industrial buildings, farm dwellings and service buildings [4]. In Nigeria, however, the major area of structural utilization of wood is in roof construction; with the building industry alone consuming about 80% of the country's estimated 20 million cubic meters of annual lumber production (5&6). Timber as a building material has the disadvantage of being combustible. Consequently, timber structures are seen

by many as creating an environment less safe than structures built of noncombustible materials such as steel and masonry. However, experience has shown that some timber structures have a fire resistance comparable, or greater than that of many noncombustible alternatives. Contrary to many people's expectations, timber used in construction performs well in fire. It will not flake, spall, melt, buckle or explode. Steel and concrete members [7] under fire have been extensively investigated in last decades. However, far fewer investigations have been carried out on timber structures [8]. Timber burns steadily at a predictable rate called charring. In the charring process charcoal is formed on the surface of the timber, which serves to insulate and protect the core. As a result, timber is now viewed as a respectable construction material. Heavy wood members have long been recognized for their ability to maintain construction integrity while exposed to fire. Research has shown that higher density species tend to have stronger timber than lower density species [9 & 10]. Cown [11], reported that the density of wood is recognised as the key factor influencing wood strength. Indeed, according to Schniewind [12] much of the variation in wood strength, both between and within species, can be attributed to differences in wood density. The mechanical properties of wood are dependent on the density, moisture content, the amount of extractives, among other factors [13], strength of wood increases as the wood density increases. When evaluating the density of wood, the level of moisture in which its mass and volume were measured must always be known. Mechanical properties most commonly measured and represented as "Strength properties" for design include maximum stress in compression parallel to grain, compressive stress perpendicular to grain.

2 Materials

Preliminary studies were carried out to identify timber species used in the construction of structural members in Southwestern Nigeria.
Six structural timber species were taken out of the ten mostly available species. All timber samples used in this research were taken from the heartwood region of the individual tree. And they were specially ordered from the lumber market.
The six species were:

- Afara (*Terminalia superba)*
- Iroko (*Milicia excelsa)*
- Mahogany (*Khaya ivorensis)*
- Mansonia (*Mansonia altissima)*
- Opepe (*Nauclea diderrichii)*
- Teak (*Tectona grandis)*

3 Experimental Methodology

3.1 Determination of Density and Moisture content

The specimens were cut into dimensions of 60mm x 20mm x 20mm for density and moisture content determination. Five samples were taken for each species and tested. The average results were then determined. Densities were determined by dividing the mass of the specimen by the volume as per equation 1,

$$Density\ \rho, = \frac{m}{v} \quad (1)$$

Where m = the mass in gram, obtained from weighing directly using digital weighing balance,
v = the specimen volume, determined by multiplying (60 x 20 x 20) mm³.

Corresponding value of density for each specimen was converted to kilogram cubic meter (kg/m³). Density is moisture dependent, because moisture adds to the mass and may cause volume to swell.

Moisture content is defined as the ratio of the mass of removable water (m_{water}) to the dry mass of wood (m_{dry}). The dry mass is obtained by oven drying at 103 ± 2 °C for 24hours as per ASTM [14]. Moisture content can be expressed as a fraction or in percentage terms (Equation 2)

$$Moisture\ Content\ (MC) = \frac{m_{wet} - m_{dry}}{m_{dry}}\ (100\%) \quad (2)$$

3.2 Modulus of Elasticity (MOE) and Modulus of Rupture (MOR)

Test samples of 300 x 20 x 20mm were obtained from each sampling level. Thirty samples, five samples from each species were used for static bending test for MOE and MOR. The machine used for the measurements is the Hounsfield Tensiometer available in forest product development and utilization department at Forestry Research Institute of Nigeria, Ibadan. The sample was prepared so that the growth rings are parallel to one edge and the sample was tested with the growth rings parallel to direction of loading i.e. it was loaded on the radial face: load of 1 ton (10,160N or 10.16KN) was applied at a speed of 0.1mm/s.

The bending strength of these wood samples were presented as a modulus of rupture (MOR) which is the equivalent stress in the extreme fibres of the sample at the point of failure assuming that the simple theory of bending applies. The MOR is calculated in three points bending from the equation below.

$$MOR = \frac{3PL}{2bh^2} \quad (3)$$

Where, MOR is in N/mm^2
P = load in Newton (N); L = span in mm;
b = width in mm; h = height in mm

And bending strength was also presented as modulus of elasticity (MOE) which provides values of works to maximum load and total work, as well as a measure of toughness. The MOE is calculated as;

$$MOE = \frac{PL}{4bh^2\ \Delta} \quad (4)$$

Where, MOE is in N/mm^2
P = load in Newton (N); L = span in mm; b = width in mm
h = height in mm; Δ = angle of inclination derived from the graph.

The replicates of five samples from each species were used to obtain the mean values according with BS [15].

3.3 Compression parallel and perpendicular to the grain

This test deals with obtaining the maximum crushing strength of the wood sample. The samples sizes is 60mm x 20mm x 20mm and a load of 1tonne (approximately 10000N or 10KN) was applied to the piston of the cage at a rate of 0.01mm/s. One of the precautions necessary in

evaluating this property is the need to ensure that the samples do not buckle during loading, thereby subjecting it to a bending rather than a compressive stress. A special cage which ensures a uniform distribution of load over the cross-section was used. The compressive strength in (N/mm^2) was obtained by:

$$Compression = \frac{P}{Area} \quad (5)$$

P = load in Newton (N);
Area = L x b; L = Length in mm; b= thickness in mm

3.4 Fire Exposure Method

The specimens were exposed to fire in electric furnace, the furnace temperature switched on was 20°C. At time of burner ignition, the following functions were done as simultaneously as possible.

- Automatic temperature recorder was started
- Stop watches started
- Furnace temperature controller started.

Specimens were exposed to fire in three batches; first batch went for time (0- 30) minutes, second batch for (0 -30) minutes and the last batch was for full (0- 60) minutes.
The first test for exposure period 0 – 30 minutes was stopped at the time when the stop watch reached 30 minutes, temperature ranging from 20°C to 230°C. Samples exposed during the second period were subjected to higher temperature 230°C to 600° C for 30 minutes (30 – 60 minutes). The third test, for exposure period 0 – 60 minutes was terminated when the furnace temperature reached 20°C to 300°C.
When testing completed, the charred wood was scrapped away from the samples and char depth measured millimetres. Charring rates were determined by dividing char depth with the corresponding fire exposure time [16].

3.5 Post Fire Strength Properties of Wood samples

The density and compressive strength of the wood samples that had charred were tested to determine their post fire strength after 0 – 60 minutes fire exposure and temperature ranging between 20°C to 300°C inside electric furnace, the char layers were easily scrapped off. The charred portion has no residual load capacity. The wood beneath the char layer has residual load capacity, but this residual capacity is less than the load capacity prior to fire.

4 Results and Discussion

4.1 Density and Moisture Content

Figure 1 illustrated the column chart of the values of density of each species at their corresponding Moisture Contents (MC) 9, 12 and 15%. The results showed that as timber species moisture content increases, the density increases. At 9% MC, Mahogany had the lowest density value of 439 ± 10.58 kg/m³. At 12 and 15% MC, Afara had the lowest density values of 444 ± 4.18 kg/m³ and 469 ± 7.07 kg/m³ respectively. At 9, 12 and 15% MC, Opepe had the highest density values of 630 ± 28.85 kg/m³, 686 ± 22.64 kg/m³ and 752 ± 17.22 kg/m³ respectively.

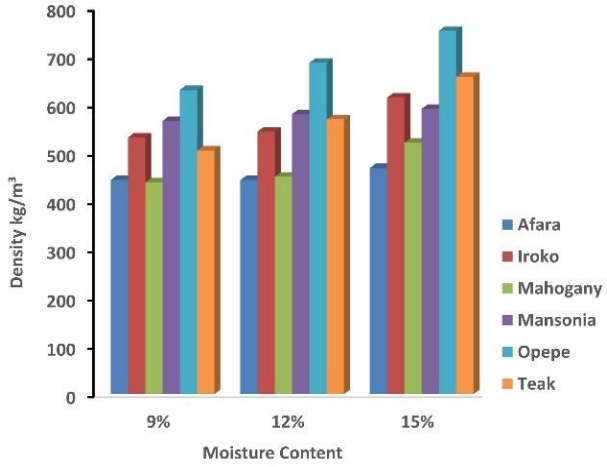

Figure 1: Density of selected Species at their corresponding Moisture Content

4.2 Modulus of Elasticity

MOE is a useful property required in designing trusses for roofing structures, dry wood is often preferred in the design of wood structures to minimize shrinkage associated with *in situ* drying in service. Figure 2 illustrated the column chart for the Modulus of Elasticity values of each species at their corresponding MC 9, 12, and 15%. It shows that MOE values increases as moisture content of wood sample reduces. At 15% MC, Teak had the lowest MOE value of 10269.20 ± 2049 N/mm^2 while Mahogany had the highest value of 15368.20 ± 904.71 N/mm^2. Afara had the lowest MOE values of 12056.00 ± 2307.71 N/mm^2 at both 9 and 12% MC. Opepe had the highest MOE value of 15557.80 ± 4718.64 N/mm^2 at 12% MC and Iroko had the highest value of 19884.80 ± 7768.79 N/mm^2 at 9% MC.

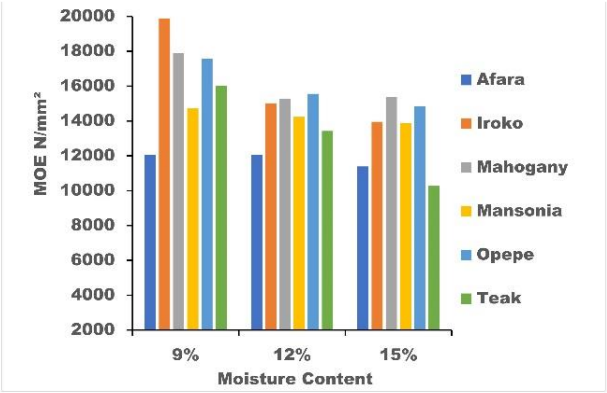

Figure 2: MOE of selected Species at their corresponding Moisture Content

4.3 Modulus of Rupture

MOR is also one of the key mechanical properties of wood measured and presented as strength property for design. It is a reflection of the maximum load carrying capacity of a member in bending and is proportional to the maximum moment borne by the specimen. Figure 3 illustrated the column chart for the Modulus of Rupture values of each species at their

corresponding 9, 12, and 15% MC moisture content. It shows that MOR values increases as moisture content of wood sample reduces. At 15% MC Opepe had the lowest MOR value of 58.50 ± 8.53 N/mm^2. At 9 and 12% MC, Afara had the lowest MOR values of 60.64 ± 2.10 N/mm^2. At 9, 12 and 15% MC, Teak had the highest MOR values of 127.14 ± 14.62 N/mm^2, 110.70 ± 12.67 N/mm^2 and 103.47 ± 10.17 N/mm^2 respectively.

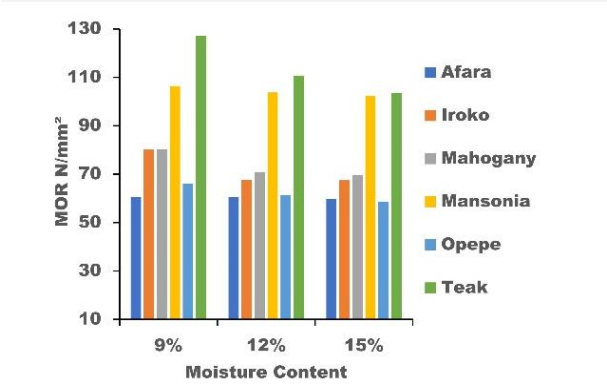

Figure 3: MOR of selected Species at their corresponding Moisture Content

4.4 Compression Results

The mean values of compression strength parallel to the grain at 9, 12, and 15% MC for each species are given in Figure 4. Compression strength parallel to the grain is higher than perpendicular to the grain and the results are similar to previous results obtained from Odom *et al*., (1994) promotion of valuable hardwood plantations in the tropics and Excerpts from the rules for materials. From the results, it showed that as timber species moisture content increases, the compressive strength parallel to the grain decreases. Afara of 9, 12 and 15% MC had the lowest Compression strength parallel to the grain values of 9.59 ± 1.08 N/mm^2, 9.59 ± 1.08 N/mm^2 and 8.13 ± 1.01 N/mm^2 respectively, while Mahogany had the highest Compression strength parallel to the grain values of 16.57 ± 0.50 N/mm^2, 15.17 ± 0.49 N/mm^2 and 12.12 ± 0.42 N/mm^2 at the three MC levels.

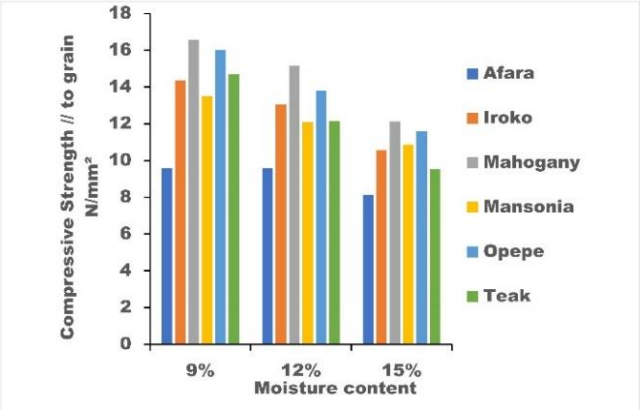

Figure 4: Compressive Strength parallel to the grain of selected Species at their corresponding MC

4.5 Post Fire Density of Samples

Table 1, showed the post fire densities values of samples. At fire exposure time of 0 - 60 minutes, 9, 12 and 15% MC, Afara had the highest percentage change in density values of 29.2, 29.1 and 28.6% respectively. At 9% MC, Iroko had the lowest percentage change in density values of 27.3%, while at 12 and 15% MC, Mahogany had the lowest percentage change in density values of 26.8 and 25.9% respectively.

Table 1: Post Fire Density of Samples and their corresponding Moisture Content (MC)

Species	MC (%)	Mean Density Before Charring test (Kg/m^3)	Mean Density After Charring test (Kg/m^3)	Percentage Loss
Afara	9	444.00	314.35	29.2%
	12	444.00	314.80	29.1%
	15	469.00	334.87	28.6%
Iroko	9	532.00	386.76	27.3%
	12	544.00	397.66	26.9%
	15	614.00	453.13	26.2%
Mahogany	9	439.00	318.71	27.4%
	12	451.00	330.13	26.8%
	15	521.00	386.06	25.9%
Mansonia	9	566.00	402.43	28.9%
	12	580.00	415.86	28.3%
	15	591.00	427.29	27.7%
Opepe	9	630.00	454.86	27.8%
	12	686.00	498.72	27.3%
	13	752.00	551.97	26.6%
Teak	9	505.00	366.13	27.5%
	12	569.20	414.94	27.1%
	15	657.00	483.55	26.4%

4.6 Post Fire Modulus of Elasticity

Tables 2, showed the post fire MOE values of samples. At fire exposure time of 0 - 60 minutes, 9 and 15% MC, Afara had the highest percentage change in MOE values of 22.6 and 19.7% respectively while at 12% MC, both Afara and Mansonia had the same percentage change in MOE value of 21.3%. At 9% MC, Iroko had the lowest percentage change in MOE value of 20.1%, while at 12% MC, Opepe had the lowest percentage change in MOE value of 19.4% and at 15% MC, both Mahogany and Teak had the lowest percentage change in MOE value of 18.6%.

Table 2: Post Fire MOE and their corresponding Moisture Content (MC)

Species	MC (%)	Mean MOE (N/mm^2) Before Charring test	Mean MOE (N/mm^2) After Charring test	Percentage Loss
Afara	9	12056.00	9331.34	22.6%
	12	12056.00	9488.07	21.3%
	15	11392.80	9148.42	19.7%
Iroko	9	19884.80	15887.96	20.1%
	12	15011.60	12009.28	20.0%
	15	13951.80	11287.01	19.1%
Mahogany	9	17883.00	14234.87	20.4%
	12	15284.40	12303.94	19.5%
	15	15368.20	12509.72	18.6%
Mansonia	9	14716.00	11478.48	22.0%
	12	14234.60	11202.63	21.3%
	15	13872.40	11084.04	20.1%
Opepe	9	17565.60	13964.65	20.5%
	12	15557.80	12539.59	19.4%
	15	14833.20	11940.73	19.5%
Teak	9	16015.80	12764.59	20.3%
	12	13429.40	10783.80	19.7%
	15	10269.20	8359.13	18.6%

4.7 Post Fire Modulus of Rupture

Table 3, showed the post fire MOR values of samples. At fire exposure time of 0 - 60 minutes, 9, 12 and 15% MC, Afara had the highest percentage change in MOR values of 35.3, 34.8 and 34.3% respectively. At 9% MC, Iroko had the lowest percentage change in MOR value of 30.6%, while at 12 and 15% MC; Opepe had the lowest percentage change in MOR values of 29.7 and 29.2% respectively.

Table 3: Post Fire MOR and their corresponding Moisture Content (MC)

Species	MC (%)	Mean MOR (N/mm^2) Before Charring test	Mean MOR (N/mm^2) After Charring test	Percentage Loss
Afara	9	60.64	39.23	35.3%
	12	60.64	39.54	34.8%
	15	59.62	39.17	34.3%
Iroko	9	80.11	55.60	30.6%
	12	67.69	47.32	30.1%
	15	67.50	47.52	29.6%
Mahogany	9	80.33	55.28	31.2%
	12	70.92	49.01	30.9%
	15	69.75	48.76	30.1%
Mansonia	9	106.39	69.79	34.4%
	12	103.78	68.70	33.8%

	15	102.38	68.70	32.9%
Opepe	9	66.13	45.70	30.9%
	12	61.34	43.12	29.7%
	15	58.50	41.42	29.2%
Teak	9	127.14	97.47	31.2%
	12	110.70	77.71	29.8%
	15	103.47	73.46	29.0%

4.8 Post Fire Compression Results

Table 4, showed the post fire Compression parallel to grain values of samples. At fire exposure time of 0 - 60 minutes, 9, 12 and 15% MC, Afara had the highest percentage change in compression parallel to grain values of 83.6 and 82 and 82.1% respectively. At 9, 12 and 15% MC, Iroko had the lowest compression parallel to grain value of 81.8, 81.1 and 80.4% respectively.

Table 4: Post Fire Compression results parallel to grain and their corresponding Moisture Content (MC)

Species	MC (%)	Mean Compression (N/mm^2) Before Charring test	Mean Compression (N/mm^2) After Charring test	Percentage Loss
Afara	9	9.59	1.57	83.6%
	12	9.59	1.65	82.8%
	15	8.13	1.45	82.1%
Iroko	9	14.35	2.61	81.8%
	12	13.05	2.47	81.1%
	15	10.56	2.07	80.4%
Mahogany	9	16.57	2.87	82.7%
	12	15.17	2.73	82.0%
	15	12.12	2.27	81.3%
Mansonia	9	13.50	2.28	83.1%
	12	12.08	2.11	82.5%
	15	10.86	1.98	81.8%
Opepe	9	16.03	2.85	82.2%
	12	13.80	2.52	81.7%
	15	11.59	2.21	80.9%
Teak	9	14.69	2.57	82.5%
	12	12.15	2.21	81.8%
	15	9.52	1.80	81.1%

5 Conclusion

In the study of the literature and laboratory tests results on material properties and external factors that influence the integrity of the timber members, the following properties and factors were found to have the largest influence:

1. Moisture content: Moisture influences in wood charring process include a greater requirement of energy to burn the wood, increasing the thermal conductivity of the wood, and delaying the rise in temperature of the wood sample's core until the moisture is evaporated. The resulting lower temperatures and slower heating rates favor the formation of char that protects the inner core of the wood to maintain its initial strength.

2. Density: Density is greatly influenced by the amount of moisture contained in timber at the time of measurement. The test results confirmed that density of wood influences significantly the charring rate, the charring rate increases with lower density, and higher density species have lower charring rate. At 9% moisture content, the highest percentage loss of density for all the selected species at 0 – 60 minutes fire exposure time (20 – 230°C) was 29% of the density before charring test. With over 70% density of the material still retained after fire exposure, the integrity of the material to continue structural functioning still intact before replacement.

3. Species of timber: The properties of timber (e.g. density, composition, permeability) vary greatly and different species will exhibit different combustion behaviour when exposed to fire. From the results Afara had the lowest density 444 kg/m3 before charring and exhibited highest percentage loss in density 29.2% after charring as compared to Opepe with highest density of 752 kg/m3 and exhibited lower percentage loss in density 26.6% after charring.

4. Grain orientation: Wood is an anisotropic material with most of its properties substantially different when considered along the grain or across the grain. Since the majority of the fire test calculations performed to evaluate the fire resistance of linear members are related to the transversal directions, little information regarding the longitudinal thermal properties of wood is available. However, it has been established that permeability for flow along the grains is 104 times that across the grains. Similarly, thermal conductivity of wood along (parallel) the grain has been reported to be in the range 1.5 to 2.8 times the conductivity across the grain, with the average value being around 2. Charring rate of wood along the grain is higher than across the grain with ratio between them ranging from 1.3 to 2.0.

5. Formation of char layer: Char layer and its fissures are important in wood charring; the layer being charred is thinner than the original thickness of the wood that has charred as a result of surface recession. The thinner insulative char layer is important in modeling of wood charring. The surface recession was due to the mechanical degradation or chemical oxidation at the surface or contraction of the char.

6. Thickness: Wood thickness influences the rate at which heat is absorbed into the surface as well as the residual section of the unburnt timber. The charring rate of timber exhibited two peaks during fire tests, during the initial exposure before char layer is developed, and towards the end of the char interface approaches the unexposed surface. Thinner specimens exhibited higher level of charring rate.

7. Thermal exposure: The low thermal conductivity of timber reduces the rate at which heat is transmitted to the interior, fire test showed that the thermal conductivity of timber is inversely proportional to the moisture content in the wood. Hence increasing moisture content (i.e. reducing thermal conductivity) will increase the rate of degradation of the wood. The charring rate increases with higher heat flux, better ventilation and more oxygen in the air.

References

[1] Bednarek, Z. (2008). Influence of Strength Reduction of Timber in Fire on Structural Resistance. *Research Gate*.

[2] Apu, S.S., (2003). Wood Structure and Construction Method for Low-cost Housing. International seminar / workshop on building materials for Low-cost housing, September 7-28, Indonesia.

[3] Kuklik, P., (2008). *Handbook 1 Timber Structure.* Leonardo da Vinci Pilot Project. Educational Materials for Designing and Testing of Timber Structures 1: pp.1-13.

[4] Breyer, D.E., Fridley, K.J., and Cobeen, K.E., (1999). *Design of wood structures.* 4th edition. McGraw-Hill, New York, U.S.A.

[5] Alade, G. A. & Lucas, E. B., (1982). Timber Connector: A Major Contributor to Structural Failure in Wooden Components in Nigeria. Paper presented at the 36th annual meeting of the Forest Products Research Society, mechanical fastening session, New Orleans, U.S.A. pp. 22.

[6] Lucas, E. B. & Olorunnisola, A. O., (2002). Wood Processing and Utilization in Nigeria: The Present Situation and Future Prospects in Agricultural Engineering in Nigeria: 30 Years of University of Ibadan Experience. Department of Agricultural Engineering, University of Ibadan, Nigeria, pp. 98-109.

[7] Bednarek, Z., (1996). Determination of the Temperature of Uncovered Steel Constructions Using Numerical Methods. *Statyba, 4(8):* 6-10.

[8] Bednarek Z., Kaliszuk-Wietecka A., and Wiśniewski T., (2002). Research on the Influence of Fire Protection Impregnation Carried out by the Vacuum -and-Pressure Method on Wood Dynamic Strength. *Building Review (Przegląd Budowlany), 10*: 12−14.

[9] Addis Tsehaye, A.H., Buchanan, A.H., and Walker, J.C.F., (1995). A Comparison of Density and Stiffness for Predicting Wood Quality. *Journal of the Institute of Wood Science 13(6):* 539-543.

[10] Walker, J.C.F., and Butterfield, B.G. (1996). The Importance of the Microfibril Angle for the processing industries. *New Zealand Forestry*, 34-40.

[11] Cown, D.J. (1992). Corewood (Juvenile Wood) in Pinusradiata- Should we be Concerned? *New Zealand Journal of Forestry Science. 22(1)*: 87-95.

[12] Schniewind, A.P. (1989). *Concise Encyclopaedia of Wood and Wood-based Materials*. Pergamon Press. pp. 248.

[13] Christoforo, A.L., Rocco, F.A.L., Morales, E.A.M., and Panzera, T.H. (2012). Influence of Displacements of Calculus of Longitudinal Modulus of Elasticity of Pinus Caribaea Structural Round Timber Beams. *International Journal of Agriculture and Forestry*, 2: 157-160.

[14] ASTM D 143-94. (2006). Standard Methods of Testing Small Clear Specimen of Timber. American Society for Testing and Materials, USA.

[15] British Standards (BS) 373. (1957). Methods of Testing Small Clear Specimens of Timber.

[16] Adetayo, O.A. and Dahunsi, B.I.O., (2018). Charring Rate Characteristics of some Selected Southern Nigeria Structural Wood Species Based on their Fire Resistance. *ACTA Technica Corviniensis – Bulletin of Engineering Tome XI. 3*, 91 – 96.

DOI: 10.1515/sspjce-2019-0019

Application of the theory of limit analysis for the study of the behavior of the ground anchor in homogeneous soil

Feriel Mekki[1], Mohamed Meksaouine [2]

[1] Department of architecture, University of Badji Mokhtar, P.B. N°12, Sidi Amar, Annaba, 23000, Algeria
[2] Department of hydraulics, University of Badji Mokhtar, P.B. N°12, Sidi Amar, Annaba, 23000, Algeria
e-mail: feriel.mekki@univ-annaba.dz, mohamed.meksaouine@univ-annaba.dz

Abstract

Ground anchors are devices used in many types of structures (on shore and offshore constructions); they can be oriented at different inclinations. Their roles are to resist tensile forces, stabilize and restrain the movement of engineered structure. The objective of this study is to propose a model which represents the mechanism of rupture of homogeneous soil (granular medium) around a single inclined ground anchor when it is tensioned and the determination of the collapse load thanks of the theory of limit analysis based on the kinematic approach in the case of criterion of Mohr-Coulomb taking into account of the mobilization of the soil in abutment in reaction to the loading.

Key words: collapse load, single ground anchor, kinematic approach, limit analysis, mechanism of rupture, Mohr-Coulomb criterion.

1 Introduction

Ground anchors also known as earth anchors or mechanical anchors have been used in the construction since the turn of the 19th century. The first application dates from 1934 in Cheurfa dam in Algeria. Their roles are to mobilize and transfer the required resisting force from the structural element to the soil. The main concern in the design and the dimensioning of the ground anchors is the determination of the capacity which they can support to prevent the rupture of the anchored structures and to ensure its stability with a high security level. The determination of the collapse load depends on several factors such as: the orientation of the ground anchors and their characteristics (the free length, the bonded length and its thickness), the type of soil (cohesionless,cohesive) and its characteristics: (angle of friction, cohesion and dilatancy), resistance of the steel, dimensions of the perforations, characteristics and quantity of the grout, irregularity of the shape of the bulb.Very few theoretical studies have been performed to determine the collapse load of ground anchors in sandy soil; empirical relationships were suggested to correlate the failure load of a single ground anchor with its geometric properties and with the characteristics of the surrounding soil [1], [2], [3], [4],

[5],[6],[7],[8]. In addition, analytical models were developed to predict the ultimate load of ground anchors [9], [10] [11], [12], [13]; but this researches did not include the effect of inclination of the ground anchor and the angle of the slope of the soil. Through this study, we propose to make a contribution to the determination of the mechanism of failure of a single inclined ground anchor at the time of tension in granular medium and to examine the effect of its inclination; the friction angle of the soil and the angle of the slope on the limit load with the use of a theoretical approach which is the theory of limit analysis using its kinematic approach.

2 The theory of limit analysis

For the study of the behavior of a single inclined ground anchor in homogeneous isotropic soil (cohesionless soil) we used a theoretical approach, which is the limit analysis in the case of the Mohr-Coulomb criterion. The theory of limit analysis is a simple method used to predict the capacity of structures to support a determined load. It relies on knowledge of the geometry of a given system, of the loading mode which is applied, resistance capacities of the constituent materials. The theory of limit analysis is based on two complementary approaches: "the static approach" and "the kinematic approach». The static approach: it stipulates that the collapse load calculated from a statically admissible stress field is a lower limit (lower bound) of the real limit load. The kinematic approach: it stipulates that the collapse load calculated from a kinematically admissible stress field is an upper limit (upper bound) of the real limit load.

3 Development of the model by the kinematic approach of limit analysis and assumptions of calculation

A single, inclined ground anchor of length (L) is placed in homogenous isotropic non-cohesive soil having a friction angle (φ) and unit weight (γ). The ground anchor is inclined at an angle (η) and the sloping surface is inclined at an angle (θ) with the horizontal. The ground anchor is subjected to a static load (F) with its point of application coinciding with the axis of the ground anchor. The anchor-soil roughness angle is higher than the friction angle ($\delta \geq \varphi$) [14].The soil mass was assumed to obey Mohr-Coulomb's failure criterion and an associated flow rule taking into account of the mobilization of the ground in abutment in reaction to the loading. The objective is to determine by the upper bound of limit analysis the failure mechanism and the collapse load during the tensioning of the ground anchor.

4 Mechanism of failure of the ground surrounding the inclined ground anchor in the plane according to Mohr- Coulomb criterion

The collapse mechanism presented in figure 1 is composed of triangular rigid block (DAB) described by the parameter (β) limited by the straight lines of rupture (AD) ,(AB) and the tilted free surface .The block (DAB) move with velocity (V_1) making an angle (φ) with the rupture lines (AD) and (AB),the ground move with the velocity (V_0) .The relative velocity (V_{01}) is also inclined at an angle (φ) with the ground anchor (AO). All the velocities can be computed in terms of (V_0) following the velocity hodograph, as shown in in figure 2.

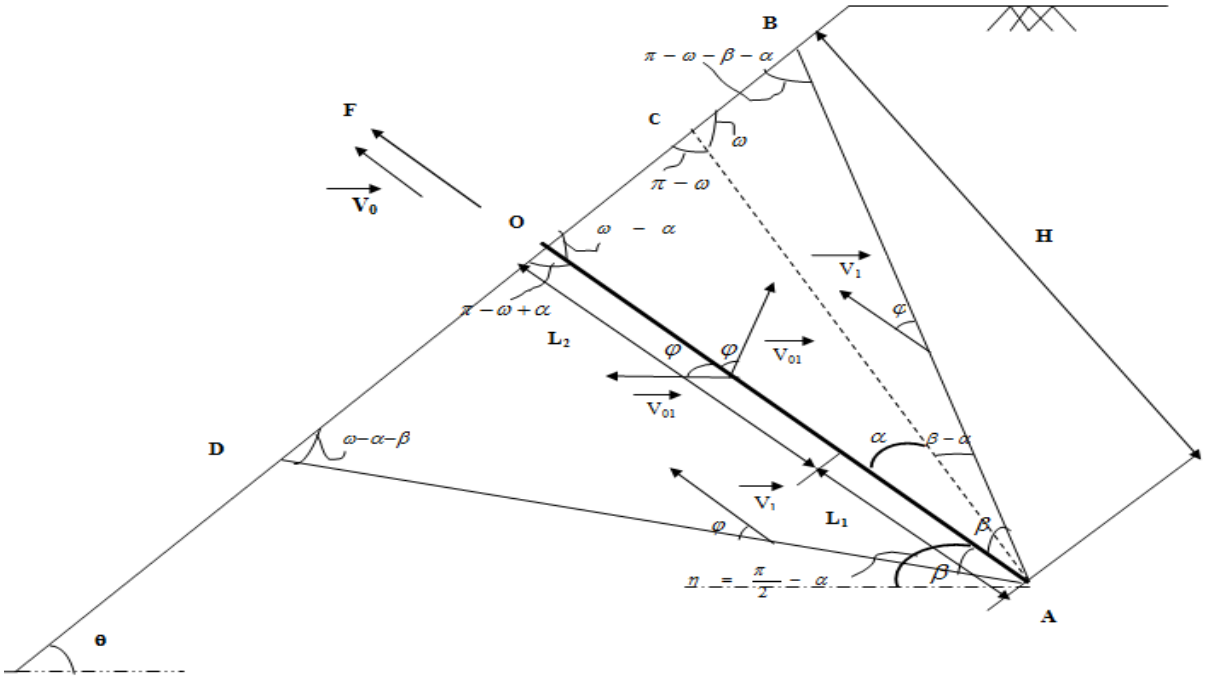

Figure 1: Mechanism of rupture of the ground surrounding the tilted ground anchor (δ≥φ) in plan according to Mohr-Coulomb criterion

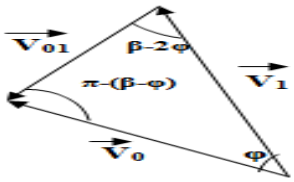

Figure 2: Velocity hodograph for failure mechanism

The velocity of the block:

$$V_1 = \frac{V_0.\sin(\beta-\varphi)}{\sin(\beta-2\varphi)} \quad (1)$$

The relative velocity ground anchor-soil:

$$V_{01} = \frac{V_0.\sin(\varphi)}{\sin(\beta-2\varphi)} \quad (2)$$

The lines of rupture:

$$L_{OA} = L_1 + L_2 = L \tag{3}$$

L: the total length of the ground anchor
L_1: the bonded length
L_2: the unbonded length
θ : the angle of inclination of sloping surface
η: the angle of inclination of the ground anchor

$$\omega = \frac{\pi}{2} + \theta \tag{4}$$

$$\alpha = \frac{\pi}{2} - \eta \tag{5}$$

$$L_{OC} = \frac{L.\sin(\alpha)}{\sin(\pi - \alpha)} \tag{6}$$

The internal dissipation of energy respectively along the lines of rupture (L_{AB}), (L_{AD}) and along the ground anchor of length (L_{OA}) is equal to:

$$E_{AB} = c.L_{AB}.V_1.\cos(\varphi) => \quad E_{AB} = \frac{c.L.\sin(\omega - \alpha).V_0.\sin(\beta - \varphi).\cos(\varphi)}{\sin(\pi - \omega - \beta + \alpha).\sin(\beta - 2\varphi)} \tag{7}$$

$$E_{AD} = c.L_{AD}.V_1.\cos(\varphi) => \quad E_{AD} = \frac{.cV_0.L.\sin(\pi - \omega + \alpha)\sin(\beta - \varphi).\cos(\varphi)}{\sin(\omega - \alpha - \beta).\sin(\beta - 2\varphi)} \tag{8}$$

$$E_{OA} = c.L_1.V_{01}.\cos(\varphi) => \quad E_{OA} = \frac{c.L_1.V_0.\sin(\varphi)\cos(\varphi)}{\sin(\beta - 2\varphi)} \tag{9}$$

For a rough ground anchor (δ≥φ), the dissipation of energy by friction of a non-cohesive soil is equal to zero.

The weight of solid masses (OAD) and (OAB) is given by following expressions:

$$W_{OAD} = \frac{\gamma.L^2.\sin(\pi - \omega + \alpha).\sin(\beta)}{2.\sin(\omega - \alpha - \beta).\sin\left(\frac{\pi}{2}\right)} \tag{10}$$

$$W_{OAB} = \frac{\gamma.L^2.\sin(\omega - \alpha).\sin(\beta)}{2.\sin(\pi - \omega - \beta + \alpha).\sin\left(\frac{\pi}{2}\right)} \tag{11}$$

c: the cohesion of the soil
γ : the unit weight of the soil

The work of the external forces:

$$T = F \times V_0 \tag{12}$$

The work of the gravitational force:

$$T_{OAB} = W_{OAB} \times V_1 \times \cos(\pi - \beta + \alpha + \varphi) \tag{13}$$

$$T_{DAO} = W_{DAO} \times .V_1 \times \cos(\pi - \beta - \alpha - \varphi) \tag{14}$$

Equating the internal rate of work done by external forces to internal dissipation of energy; the value of (F) can be obtained:

$$F = \frac{c.L.\sin(\omega-\alpha).\sin(\beta-\varphi).\cos(\varphi)}{\sin(\pi-\omega-\beta+\alpha).\sin(\beta-2\varphi)} + \frac{c.L_1.\sin(\varphi).\cos(\varphi)}{\sin(\beta-2\varphi)} + \frac{c.L.\sin(\pi-\omega+\alpha).\sin(\beta-\varphi).\cos(\varphi)}{\sin(\omega-\alpha-\beta).\sin(\beta-2\varphi)} +$$
$$\frac{\gamma.L^2.\sin(\omega-\beta).\sin(\beta).\cos(\pi-\beta+\alpha-\varphi)..\sin(\beta-\varphi)}{2.\sin(\pi-\omega-\beta+\alpha)\sin\left(\frac{\pi}{2}\right).\sin(\beta-2\varphi)} + \frac{\gamma.L^2.\sin(\beta)\sin(\pi-\omega+\alpha).\cos(\pi-\beta-\alpha-\varphi).\sin(\beta-\varphi)}{2.\sin(\omega-\alpha-\beta).\sin\left(\frac{\pi}{2}\right)\sin(\beta-2\varphi)} \quad (15)$$

The analysis of equations and results is processed by MATHCAD software.

5 The material used

To estimate the collapse load of a single inclined ground anchor placed in granular medium; we have used Hostun sand. It is sand with tight granulometry whose characteristics appear in table 1.

Table 1: Physical characteristic of the sand

Designation	Dimensions in mm		Void ratio	
	d_{min}	d_{max}	e_{min}	e_{max}
Sand	0.3	1	0.607	0.885

The relationship between the density of the sand and its friction angle is put in form of polynomial of the second degree [15].

$$\varphi = -97.0424 \times D^2 + 368.8507 \times D - 304.919 \quad (16)$$

The soil parameters used in this study: the unit weight (γ=1570 kg/m^3), the friction angle (φ=35°).

5.1 Application with software Mathcad

The model is introduced into the software MATHCAD which will allow us the visualization of the curve of the collapse load (F) as shown in figure 3.
Data:
L=12m, L_1=4m, c=0 kg/m^2, γ=1570 kg/m^3, φ=35°,V_0=1m/s, θ=25°, η=20°
Boundary condition:
β=1.7
Given
1.5<β<2
Minimization:
Minimize (F, β)=1.828
F (1.828) =2.437×10^{5}kg

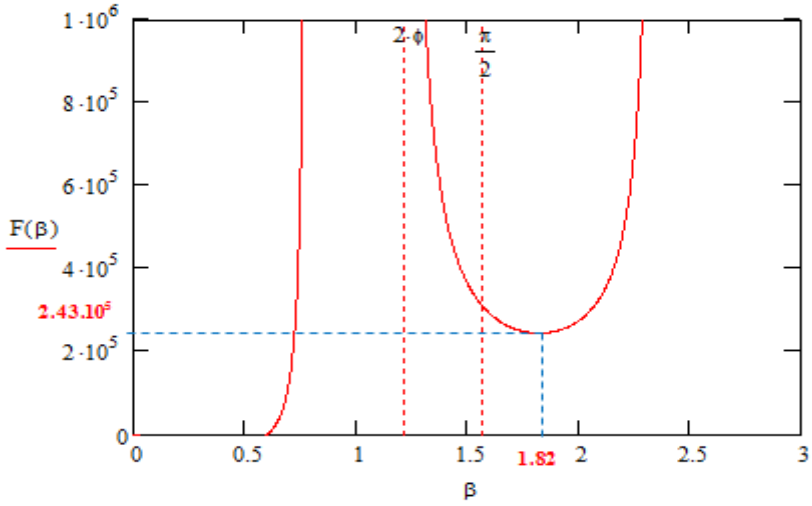

Figure 3: Visualization of the curve F (β) in the plan

The figure 3 represents the maximum effort of the model in the plan according to the parameter (β) which has a concave form indicating a minimum.

6 Mechanism of failure of the ground surrounding the inclined ground anchor in the space according to Mohr Coulomb criterion

The mechanism of failure in the space is shown in figure 4 .At collapse; it is assumed that the ground anchor and the rigid block (DAB) move as a single rigid unit in the inclined direction with a velocity (V_0).

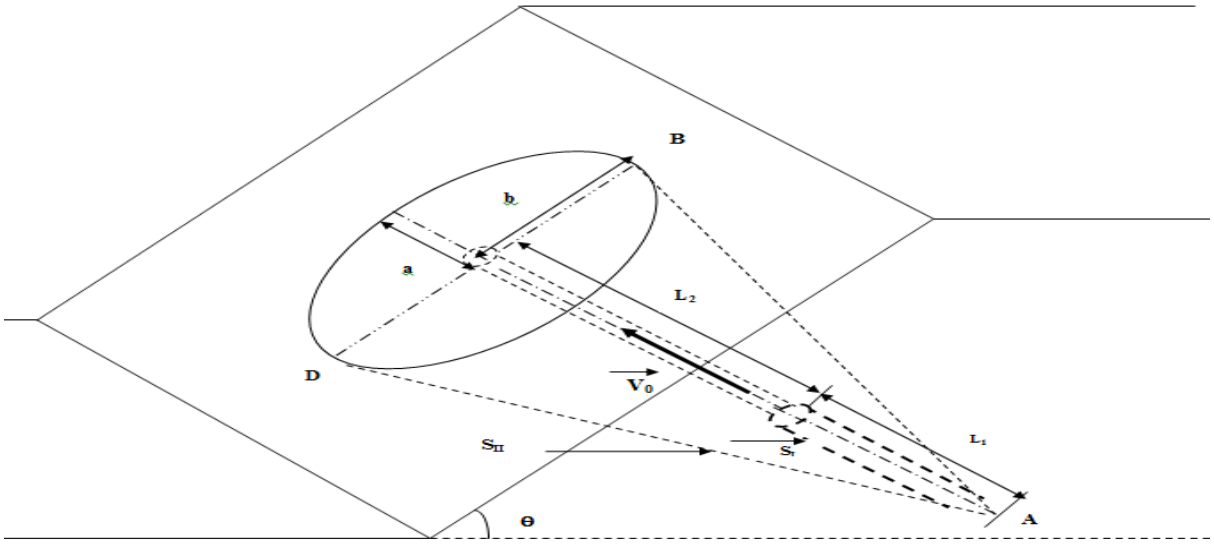

Figure 4: Mechanism of rupture of the ground surrounding the tilted anchor (δ≥φ) in space according to Mohr-Coulomb criterion

The velocities (V_{01}) and (V_1) are expressed respectively by the expressions (1) and (2).

The rupture surfaces:

S_I : Side surface of the cylinder

$$S_I = \pi.d.L_1 \tag{17}$$

d: the diameter of cylinder

S_{II} : Side surface of the cone

$$S_{II} = \pi.R.H \tag{18}$$

$$H = L\sin(\omega - \alpha) \tag{19}$$

$$L_{DB} = \frac{H.\sin(2\beta)}{\cos(\alpha+\beta).\cos(\alpha-\beta)} \tag{20}$$

$$R = \frac{L_{DB}}{2} = b = \frac{H.\sin(2\beta)}{2.\cos(\alpha+\beta).\cos(\beta-\alpha)} \tag{21}$$

$$S_{II} = \frac{\pi.H^2.\sin(2\beta)}{2.\cos(\beta-\alpha).\cos(\alpha+\beta)} \tag{22}$$

The internal dissipation of energy respectively along the rupture surfaces (S_1),(S_{II}) is equal to:

$$E_{OA} = c.S_I.V_{01}.\cos(\varphi) => E_{OA} = \frac{c.\pi.d.L_1.V_0.\sin(\varphi).\cos(\varphi)}{\sin(\beta-2\varphi)} \tag{23}$$

$$E_{DA} = c.S_{II}.V_1.\cos(\varphi) => E_{DA} = \frac{c.\pi.H^2.V_0.\sin(2\beta).\sin(\beta-\varphi)\cos(\varphi).}{2.\sin(\beta-2\varphi).\cos(\beta-\alpha).\cos(\alpha+\beta).\sin(\beta-2\varphi)} \tag{24}$$

For a rough ground anchor ($\delta \geq \varphi$), the dissipation of energy by friction of a non-cohesive soil is equal to zero.

The weight of solid masse (DAB):

$$W_{DAB} = \frac{\pi.\gamma.a.b.H}{3} \tag{25}$$

The surface of the ellipse: (26)

$$B = \pi.a.b$$

(27)

$$a = L.tg(\beta)$$

$$b = \frac{H}{2}[tg(\beta-\alpha) + tg(\alpha+\beta)] \tag{28}$$

The work of the external forces:

$$T = F \times V_0 \tag{29}$$

The work of the gravitational force:

$$T_{DAB} = W_{DAB} \times V_1 \times \cos(\pi-\alpha) \tag{30}$$

Equating the internal rate of work done by external forces to internal dissipation of energy; the value of (F) can be obtained:

$$F = \frac{c.\pi.d.L_1.\sin(\varphi).\cos(\varphi)}{\sin(\beta-2\varphi)} + \frac{c.\pi.H^2.\sin(2\beta).\sin(\beta-\varphi).\cos(\varphi)}{2.\sin(\beta-2\varphi).\cos(\beta-\alpha).\cos(\alpha+\beta).\sin(\beta-2\varphi)} + \frac{\pi.\gamma.a.b.H.\sin(\beta-\varphi).\cos(\pi-\alpha)}{3.\sin(\beta-2\varphi)} \tag{31}$$

The collapse load (F) is expressed in terms of non-dimensional uplift factor (N_γ) as defined herein:

$$F = N_\gamma . \gamma . L^3 \tag{32}$$

$$N_\gamma = \frac{F}{\gamma . L^3} \tag{33}$$

6.1 Application with software Mathcad

The model is introduced into the software MATHCAD which will allow us the visualization of the curve of the collapse load (F) as shown in figure 5.

Data:

L=12m ,L_1=4m, d=0.12m, c=0 kg/m^2,γ=1570 kg/m^3,φ=35°,V_0=1m/s,θ=25°,η=20°

Boundary condition:

β=2.4

Given

2<β<2.5

Minimization:

Minimize (F, β)=2.367

F (2.367) =6.89×10^{5}kg

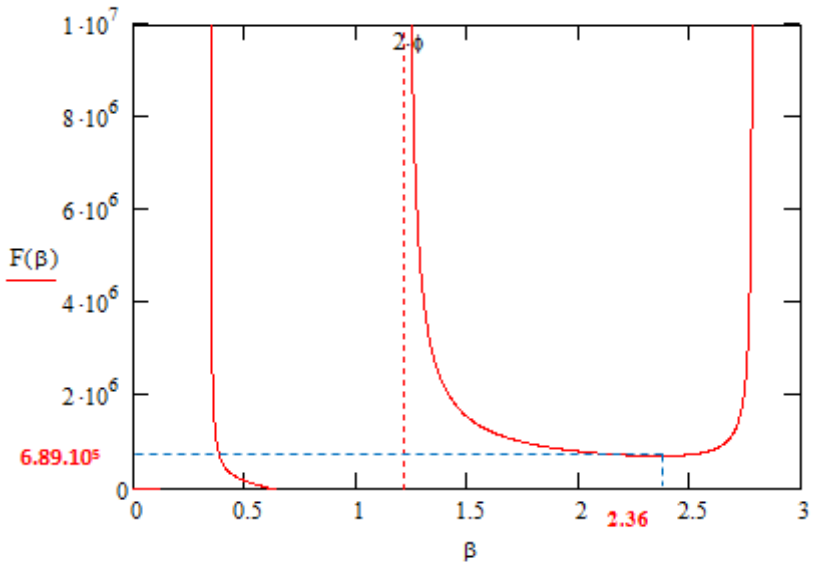

Figure 5: Visualization of the curve F (β) in space

The figure 5 represents the maximum effort of the model in the space according to the parameter (β) which has a concave form indicating a minimum.

7 Results and discussion

We studied the effect of the friction angle (φ was varied from 30 °to 40 ° with an interval of 1°), the effect of the angle of inclination of ground anchor (η was varied from 10 ° to 30 °with an interval of 5°), and the effect of the angle of inclination of sloping surface (θ was varied from 25 ° to 33 °with an interval of 4°) on the magnitude of the uplift factor (N_γ).The results obtained are shown in the figures below, from figure 6 to figure 13.

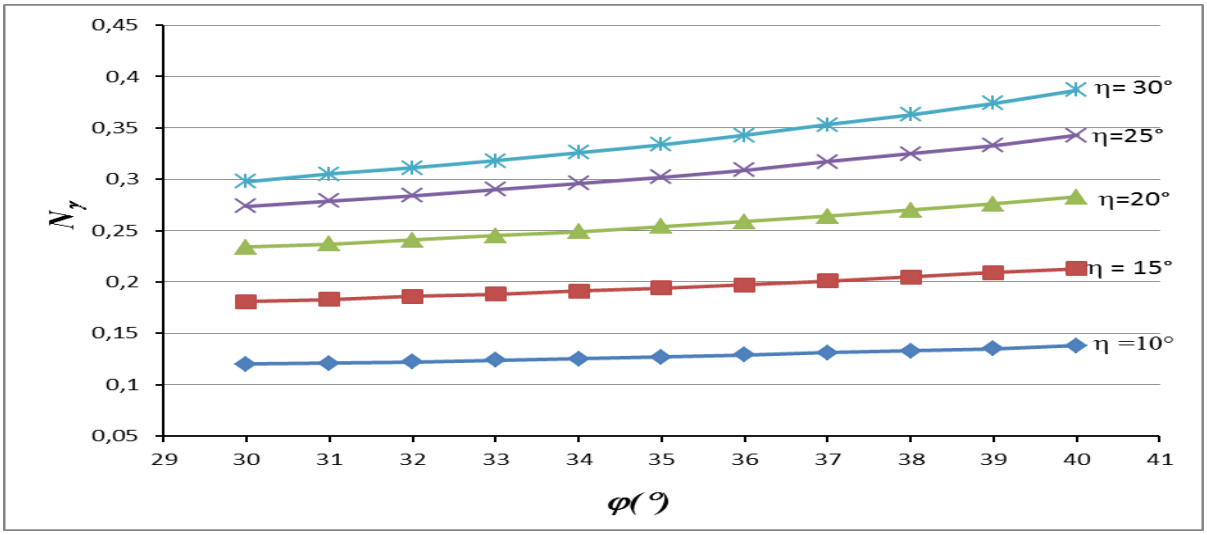

Figure 6: Evaluation of the uplift factor (N_γ) with η and φ for θ=25°

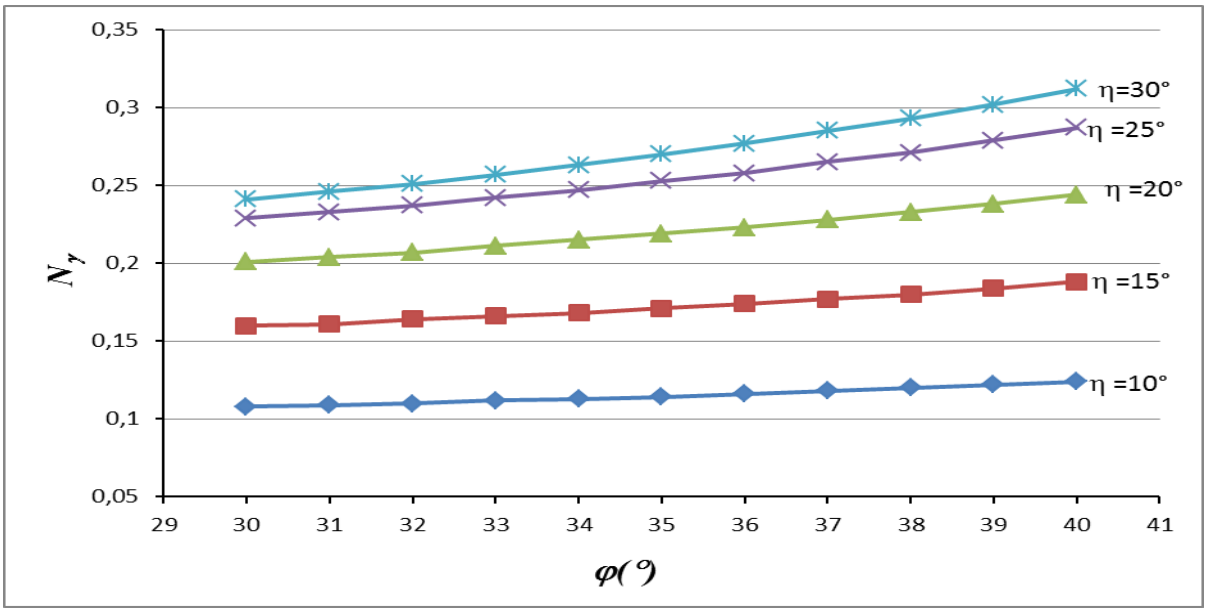

Figure 7: Evaluation of the uplift factor (N_γ) with η and φ for θ=29°

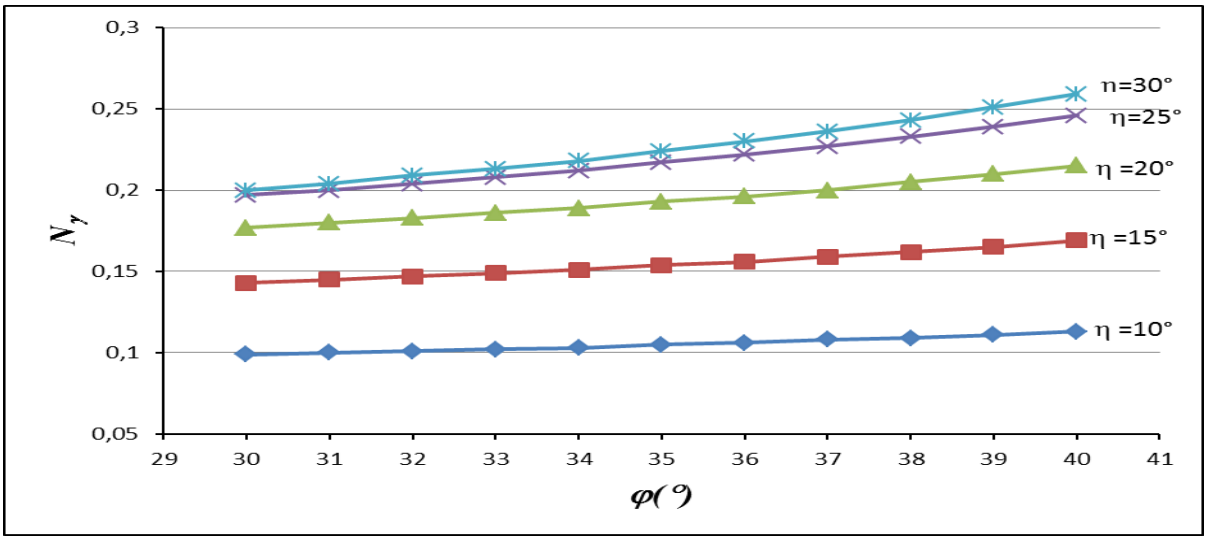

Figure 8: Evaluation of the uplift factor (N_γ) with η and φ for θ=33°

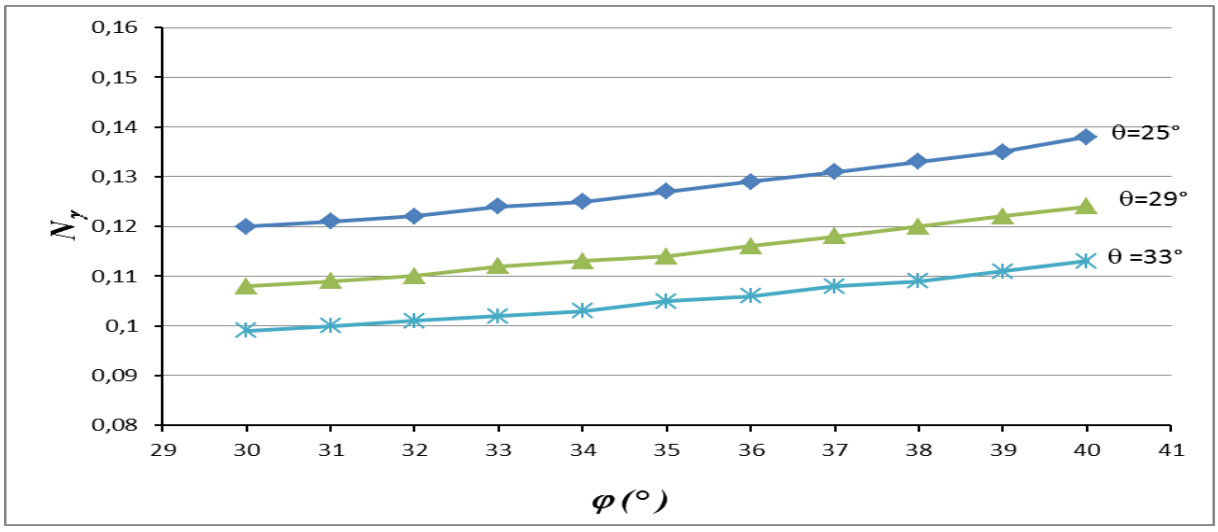

Figure 9: Evaluation of the uplift factor (N_γ) with θ and φ for η=10°

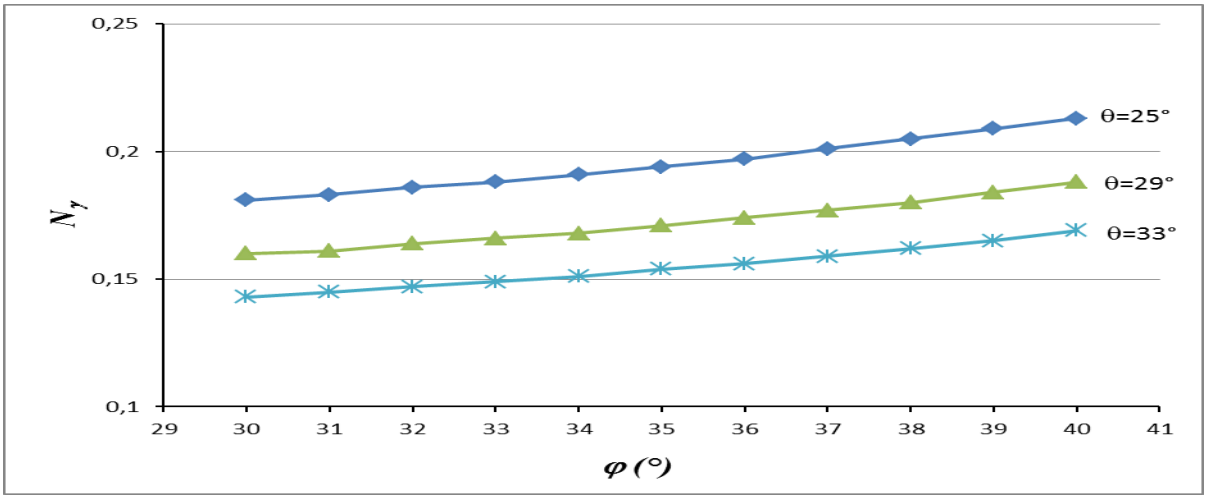

Figure 10: Evaluation of the uplift factor (N_γ) with θ and φ for η=15°

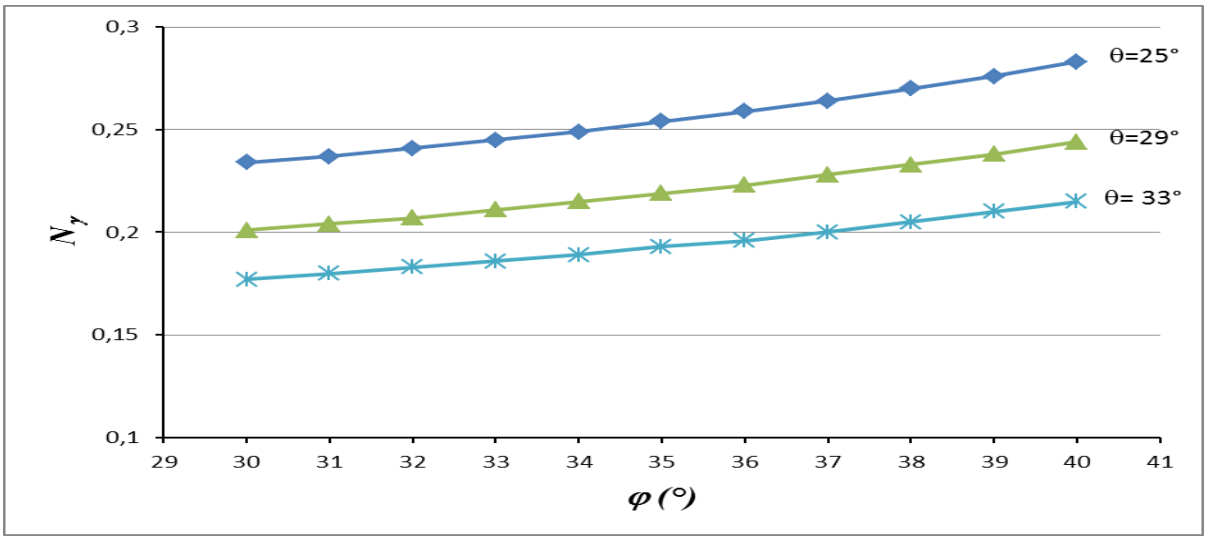

Figure 11: Evaluation of the uplift factor (N_γ) with θ and φ for η=20°

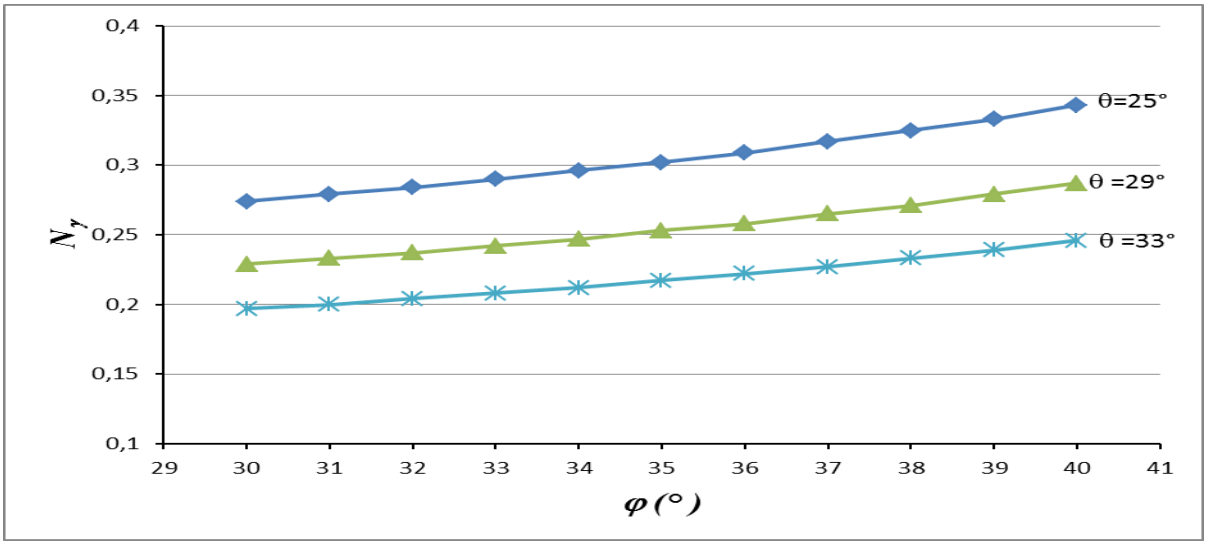

Figure 12: Evaluation of the uplift factor (N_γ) with θ and φ for η=25°

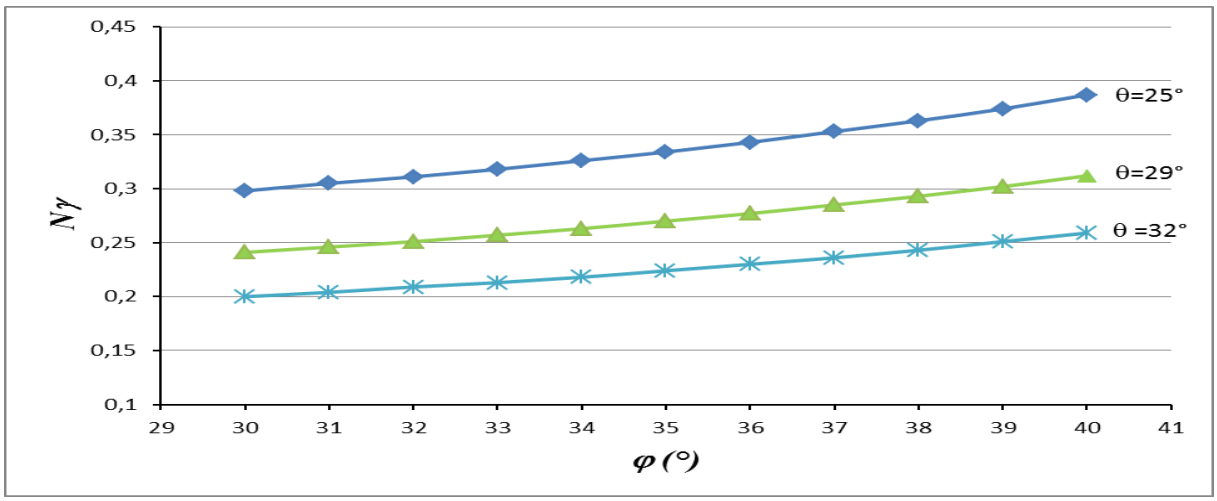

Figure 13: Evaluation of the uplift factor (N_γ) with θ and φ for η=30°

It can be observed from figures 6, 7, 8, 9, 10, 11, 12 and 13 that the value of uplift factor (Nγ) increases with the increase of the internal friction angle of the soil (φ), with the inclination of the anchor (η) and with the angle of the slope (θ). This implies that the collapse load increases with the evolution of these three parameters.
Figures 6 to 13 can be considered as abacuses for predicting the collapse load of an inclined ground anchor embedded in sloping ground composed of a cohesionless soil.

8 Conclusion

With the application of the kinematic approach of limit analysis, theoretical solutions have been generated for computing the ultimate load of a single inclined ground anchor buried in sloping ground (frictional soil) and subjected to static load for different soil friction angles

with varying the ground anchor inclinations and the slope angles. The results obtained have been presented in terms of uplift factor (N_γ) in both graphical forms to facilitate their use in solving practical design problems.

Through this study the following results are founded:

- The shape of the curve F (β) of the model in plane and space is concave indicating the existence of a minimum.
- The uplift factor (Nγ) increases with the increase of the friction angle of the soil (φ), the inclination of the ground anchor (η) and the angle of the slope (θ).
- The elaborate model proposed in a single block undoubtedly overestimates the value of the limit load; but this is still a first limit value that the real value cannot exceed.
- The solutions developed in the present study are expected to be useful for purpose of design of inclined ground anchor embedded in sloping ground (sandy soil).

This work proposes a solution to this problem in the case of frictional soil never realized with this method that can be taken by other researchers.

References

[1] Hawkes, J. M. and Evans R. H. (1951). Bond stresses in reinforced concrete columns and beams. *Structural Engineering, 29(12)*, 323-327.

[2] Phillips, S. H. E. (1970) Factors affecting design of anchorages in rock, Cementation Research Report R48/70.London, cementation research Ltd.

[3] Littlejohn, G. S. (1970). Soil anchors, Ground Engineering, Proceedings of an ICE Conference, ICE, London.

[4] Kramer. H. (1978). Determination of the carrying capacity of ground anchors with the correlation and regression analysis, *Revue Française de Géotechnique, 3*, 76-81.

[5] Hanna, T. (1982). *Foundations in tension-ground anchors*, Trans Tech Publications, Clausthal-Zellerfeld, Germany.

[6] Xanthakos, P.(1991). *Ground anchors and anchored structures*, John Wiley & Sons, Inc,

[7] Barley, A.D. (1995). Theory and practice of the Single Bore Multiple Anchor System in Proceedings of the Anchors in Theory and Practice, International Symposium on Anchors in Theory and Practice, Saltzburg, Austria.

[8] Habib, P., Logcais, L., Clément, P., Dupeuble, P .(1995). *Tirants d'ancrage (recommandations T.A.95)*, France, Eyrolles Editions.

[9] Mekki, F., Meksaouine, M. and Guenfoud, M. (2009). Theoretical study of the behaviour of anchors in homogeneous soil, *International Review on modelling and simulations, 2*, 221-226.

[10] Mekki, F., Meksaouine, M. and Guenfoud, M. (2011). Etude théorique du comportement des tirants d'ancrages dans un sol pulvérulent, *la revue Synthèse.,No. 23*, 22-30.

[11] Rong, J. Z., Jun, J. Z., Pei, Y. L., Juan Z. and Shun Y. (2012). A method for predicting mechanical behavior of HPJG-Anchors part I: Mechanical characteristics and load transfer models, *Computer and Geotechnics, 45*, 62-73.

[12] Mekki, F. (2015).*Etude théorique du comportement des tirants d'ancrages***,** Editions Universitaires Européennes.

[13] Yang, Z., Chen, J., Zhang, H., Zhao, X., Li,H.(2018).Analytical calculation on the load displacement curve of grouts soil anchor, Journal of engineering science and technology review, *11 (3)*, 31-41.

[14] Chen, W.F. (1975). *Limit Analysis and Soil Plasticity*, Elsevier, Amesterdam, Netherland.

[15] Bourdeau, Y. (1977). *Pushed non-cohesive soils. Influence characteristics of the grounds and model of test*, PhD Thesis, I.N.S.A, Civil engineering.

DOI: 10.1515/sspjce-2019-0020

Assessment of ecological stability of the built environment in relation to sustainable construction

Natalia Junakova, Jozef Junak, Eva Šelingova

Technical University of Košice, Slovakia
Faculty of Civil Engineering, Institute of Environmental Engineering
e-mail: natalia.junakova@tuke.sk, jozef.junak@tuke.sk

Abstract

When placing buildings in a landscape environment, the urban and architectural design of the building must be in harmony with the surrounding environment. The environmental criterion in assessing the sustainability of buildings and the subsequent environmental certification of buildings is the construction site selection in terms of its ecological importance. The way to determine the ecological value of a territory is through the determination of the landscape's ecological stability, which can be considered as a basis for assessing all conditions and assumptions of land use. Maintaining ecological stability on Earth is a prerequisite for sustainable development and is of long-term strategic importance for the development of society.

The contribution is focused on the evaluation of ecological stability in relation to sustainable construction in the cadastral area of the village Vajkovce, located in the district of Košice-okolie (surrounding). The ecological stability of the territory is evaluated by several methods used in the assessment of the landscape ecological stability and their modifications expressed by the coefficient of ecological stability. The results indicate that the territory of the municipality of Vajkovce is one of the ecologically unstable areas and therefore appropriate measures were proposed to increase its ecological stability.

Key words: sustainable construction, environmental assessment method, coefficient of ecological stability

1 Introduction

The development of each society takes place in the landscape and is significantly influenced by its characteristics. An essential condition for the development of society is that the country in which it takes place is a sustainable and safe environment for it. The most visible activity of man in the landscape is the construction activity which is directly related to the use of natural resources [1], to the transformation of the human environment, to the conservation or, conversely, to the deterioration or degradation of the natural or cultural heritage [2].

In order to the landscape to be able to fulfill its production and non-production functions on a permanent basis, it is necessary to know the limit value to which it can be loaded without

compromising its functionality [3,4]. In this case, we can speak of determining its ecological stability. It expresses the ecosystem's ability to apply self-regulating mechanisms so as to return to a steady state after an external disturbance and to preserve its natural properties and functions [5]. A prerequisite for sustainable development is to maintain ecological stability on Earth, which is of long-term strategic importance for the development of society [6]. The key priorities of ecological stability are maintaining the landscape's resilience to human interventions and maintaining biodiversity [7].

Several methodological tools have been developed to determine the landscape ecological stability. Most of them are based on the calculation of the ecological stability coefficient (CES), which assesses the degree of the landscape stability as a whole, through the degree of cultural transformation (i.e by expressing the degree of anthropic pressure on the landscape [8]. By applying a uniform method of calculating the landscape ecological stability coefficient in our conditions in practice, data and spatial compatibility will be ensured.

2 Material and methods

The aim of the paper is to evaluate the ecological stability in the cadastral area of the village Vajkovce by various methodological tools and to propose appropriate measures to increase its ecological stability.

2.1 Study area

Vajkovce village lies in the Košice basin (Košická kotlina) about 10 km northeast of Košice and about 20 km southeast of Prešov in the southern part of the valley of the Torysa River. It is connected to these cities by a motorway. The Torysa River flows through the cadastral territory of Vajkovce, to which the Vajkovský creek merges from the right side and the Chrastianský creek merges from the left side [9]. There is an inundation area around the Torysa River. At high flow rates, the Torysa River floods a wide plain of up to 1 km. Inundation area also extends to the built-up area of Vajkovce. The riverbed of the Torysa River isn't artificially channeled. Already the Q_5 discharge causes local overflow and a relatively extensive inundation in the riverbed valley. The river overflows mainly to the left side of the territory [10].

The cadastral area of the municipality covers an area of 388.8 hectares [9]. The relief of the village and its surroundings is mostly flat, at the edges there is a slightly hilly surface of deforested soil. In the central part of the northern edge of the cadastre there is a forest-like ground cover on the agricultural land. Non-forest woody vegetation is relatively well represented, concentrated mainly around watercourses and in their floodplains, on steep balks where is spatially and species-structured. Permanent grasslands are concentrated in the floodplain of the Torysa River and in the valley of the Chrastianský creek (Fig. 1).

Figure 1: Cadastral area of the Vajkovce village

The assessed area was included in the relevant Regional Territorial System of Ecological Stability. However, there are no real elements of the territorial system of ecological stability in the territory. In the Regional Territorial System of Ecological Stability, only the areas declared within the framework of preventive measures of nature protection are mentioned, from which the Torysa River and the Chrastianský creek stretches into the territory.

2.2 Methods used for determination of ecological stability

The ecological stability of the landscape was expressed using the coefficient of ecological stability. The determination of the CES as a relatively simple indicator of the state of landscape ecological quality was carried out using the three methods set out below. In calculations, it is considered to express the area ratio of stabilizing and non-stabilizing landscape elements, covering the all area of interest without detailed localization.

2.2.1 Calculation of CES by Míchal (1985)

The basic methodology for the CES determination is based on the determination of the ratio of areas of stable and unstable landscape-forming elements in the surveyed area [11] according to formula (1):

$$CES_1 = \frac{stable\ elements}{unstable\ elements} \tag{1}$$

where ecologically significant elements are interpreted as the landscape-forming ones with a positive (stabilizing) effect on the surrounding landscape like woody vegetation, grassland, orchards, vineyards, gardens, urban vegetation, recreational and leisure areas, water bodies and ecologically relatively unstable land use categories are arable land annually ploughed, built-up areas without green urban areas and leisure areas.

2.2.2 Calculation of CES by Löw et al. (1984)

In this methodology [12], the determination of CES is based on the percentage of areas with different (five) degrees of ecological quality and can be calculated according to (2):

$$CES_2 = \frac{1{,}5A+B+0{,}5C}{0{,}2D+0{,}8E} = \frac{1{,}5*17.6+0{,}5*(19.7+24.9+21.9)}{0{,}2*242.5+0{,}8*(42.5+19.7)} = 0.61 \quad (2)$$

where A is percentage of surfaces with 5th degree of environmental quality (forests, water elements); B is percentage of surfaces with 4th degree of environmental quality (riparian vegetation, game refuges); C is percentage of surfaces with 3th degree of environmental quality (permanent grassland, pastures); D is percentage of surfaces with 2th degree of environmental quality (arable land) and E is percentage of surfaces with 1th degree of environmental quality (built-up areas).

2.2.3 Calculation of CES by Miklós (1986)

According to Miklos [13], the areas with the highest proportion of high landscape value elements are considered as ecologically the best quality. Therefore, instead of the simplest division of areas into relatively stable and unstable areas, the calculation includes differentiation of their ecological significance. The ecological stability coefficient can then be calculated according to equation (3):

$$CES_3 = \sum_{i=1}^{n} \frac{p_n * k_{pn}}{p} \quad (3)$$

where p_n is the area of individual elements, k_{pn} is coefficients of ecological significance of individual elements (arable land = 0.14, build-up areas = 0, other areas = 0.1, gardens = 0.5, permanent grassland = 0.62, pastures = 0.68, water areas = 0.79) and p is the total area of elements (ha).

3 Results and discussion

Calculation methodology is based on the assumptions of a uniform land inventory within the cadastral areas. The representation of individual landscape-forming elements in the cadastral area is given in Table 1.

Table 1: Land-use of the Vajkovce cadastral territory

Land-use	Area (ha)
Arable land (OP)	242.5
Build-up areas (AP)	42.5
Other areas (OA)	19.7
Gardens (Za)	21.9
Permanent grassland (TTP)	19.7
Pastures (Pa)	24.9
Water areas (VP)	17.6

3.1 Ecological stability of Vajkovce cadaster

According to described methods, the coefficient of ecological stability in the cadastral area of Vajkovce village was calculated using formulas (1) – (3) and the landscape was classified. CES calculations using individual methods in Vajkovce cadastre were compared and are given in Tab. 2.

$$CES_1 = \frac{stable\ elements}{unstable\ elements} = \frac{VP + Za + TTP + Pa}{OP + OA + AP} = \frac{21.9 + 19.7 + 24.9 + 17.6}{242.5 + 42.5 + 19.7} = 0.28 \quad (4)$$

$$CES_2 = \frac{1,5A + B + 0,5C}{0,2D + 0,8E} = \frac{1,5 * 17.6 + 0,5 * (19.7 + 24.9 + 21.9)}{0,2 * 242.5 + 0,8 * (42.5 + 19.7)} = 0.61 \quad (5)$$

$$CES_3 = \sum_{i=1}^{n} \frac{242.5 * 0.14 + 42.5 * 0 + 19.7 * 0.1 + 21.9 * 0.5 + 19.7 * 0.62 + 24.9 * 0.68 + 17.6 * 0.79}{388.8} = 0.23 \quad (6)$$

Table 2: Comparison of individual methods of determination of ecological stability of Vajkovce area and landscape classification

Method	Calculated value of CES	Classification	
Míchal (1985)	0.28	0.11 – 0.30	over-exploited territory with a distinct disruption of natural structures
Löw et al. (1984)	0.61	0.10 – 1.00	disturbed landscape capable of autoregulation
Miklós (1986)	0.23	< 0.33	ecologically unstable landscape

On the basis of the results (formulas (1) – (3) and Tab. 2) it can be stated that the landscape is composed of unstable landscape-forming elements and the existing structure of the territory is significantly negatively affected by anthropogenic activity. In order to increase the ecological stability of the assessed landscape, measures should be proposed to improve its ecological stability.

3.2 Measures to improve ecological stability

For improving the current state of the area (Fig. 2a) with respect to ecological stability, the following measures have been proposed in the area (Fig. 2b): (i) in the inundation area of the Torysa River, a change of land use of 91 ha from arable land to permanent grassland is proposed; (ii) park with an area of 1.82 ha is designed for recreation in the newly built residential area.

It is also necessary to create (in a less stable part of cadaster, northeast of the village) conditions for the restoration of the agricultural landscape by planting greenery along field roads to ensure ecological stability and increase biodiversity in the territory.

Some measures of a technical character are needed to improve the quality of the environment and protect the health of the population (construction and completing of infrastructure,

improvement of the existing energy resources use) so as to avoid pollution and degradation of natural resources related to human health. However, some negative impacts can be eliminated by relatively common measures, namely by planting greenery within the territory of the village (build-up area), on its edge and especially around agricultural buildings.

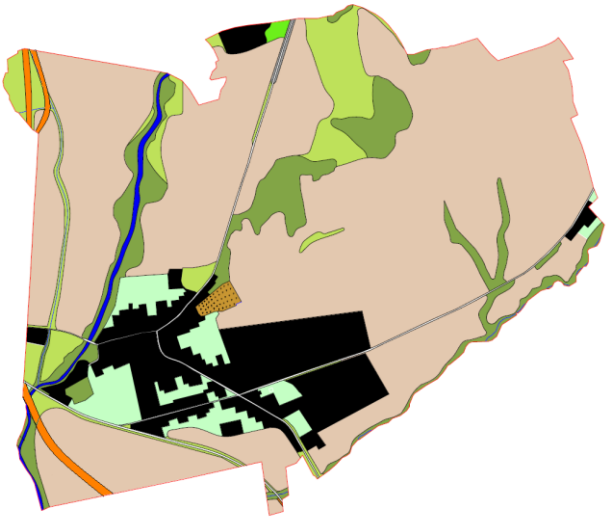

Figure 2a)

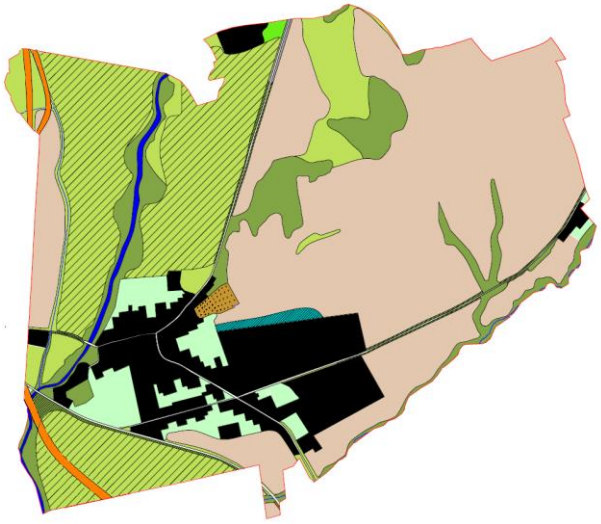

Figure 2b)

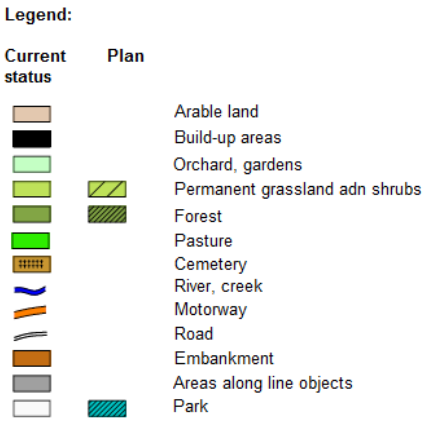

Unsuitable plantings of non-native poplar cultivars need to be gradually transformed into species-natural and richer structured line stands of trees. The pastures must be kept in their current state, or it is necessary to ensure their gradual conversion into species-rich communities with a higher proportion of flowering plants by sowing natural grass mixtures.

In particular, it is necessary to consider technical and biological measures in connection with the newly built motorway, the route of which runs through the entire western edge of the cadastral area. It is mainly the integration of the motorway into the landscape and the elimination of its adverse effects. When greening areas around the motorway, native non-forest woody species should be used that meet the site conditions. Other measures that may be proposed include the preservation of natural bank vegetation along the watercourses flowing through the cadastral area and the planting of linear greenery along the roads.

4 Conclusion

Ecological stability quantitatively expresses the extent to which the landscape is affected by anthropic activities. Accompanying features of intensive land use are changes not only in the landscape structure, characterized mainly by the loss of natural and semi-natural elements (forests, permanent grassland, gardens), but also by the simultaneous growth of negative impacts such as air or water pollution. The assessment of ecological stability represents a rather complicated methodological process, which can be simply expressed in such a way that the higher the area of greenery representation in municipalities, the higher the ecological stability of the landscape. Therefore, by proposing appropriate measures and changing the land-use, it is possible to mitigate the negative impact of human on landscape.

Acknowledgements

This research has been supported by the Slovak Grant Agency for Science (Grant No. 1/0419/19) and by the Slovak Cultural and Education Grant Agency (Grant No. 073TUKE-4/2018).

References

[1] Junakova N. & Junak J. (2017) Recycling of reservoir sediment material as a binder in concrete. *Procedia Engineering. Volume 180,* 1292-1297.

[2] The Ministry of the Environment of Slovak Republic (2001). *National Sustainable Development Strategy* (in Slovak). Bratislava: The Ministry of the Environment of Slovak Republic.

[3] Petříček V. & Plesník J. (2012). Significant landscape features and ecological stability (in Slovak). *Ochrana přírody. Volume 67*, 41-44.

[4] Junakova N. & Balintova M. (2011). Model for predicting the nutrient content in reservoir bottom sediments. In 11th International Multidisciplinary Scientific Geoconference and EXPO - Modern Management of Mine Producing, Geology and Environmental Protection, SGEM 2011, Volume 3, 20. June 2011 – 25. June 2011 (475-482). Varna, Bulgaria: STEF92 Technology Ltd, Sofia, Bulgaria.

[5] Act No. 17/1992 Coll. on the Environment (1992). Bratislava.

[6] Ližbetinová M. (2014). Ecological stability of the landscape of catastral territory in Tatranska Lomnica from 1953 and now (in 2013) (in Slovak). *Acta Universitatis Matthiae Belii series Environmentálne manažérstvo*. *Volume XVI. (1),* 67-76.

[7] Izakovičová Z., Miklós L. & Drdoš, J. (1997). Landscape ecological conditions of sustainable development (in Slovak). Bratislava: VEDA.

[8] The Ministry of the Environment of Slovak Republic (1993). *Methodological guidelines for the preparation of documents of the territorial system of ecological stability* (in Slovak). Bratislava: The Ministry of the Environment of Slovak Republic.

[9] Municipality of Vajkovce. Official website of the municipality (in Slovak). (12.2.2020) http://www.obecvajkovce.sk/-zakladne-informacie.

[10] National Motorway Company (2016). *Motorway D1 Budimír - Bidovce, Notification of change of proposed activity* (in Slovak). Bratislava: National Motorway Company.

[11] Míchal I. (1982). Principles of landscape assessment (in Slovak). *Architektúra a urbanizmus. Volume XVI(Z),* 65-87.

[12] Löw J. et al. (1984). *Principles for defining and designing territorial systems of ecological stability in land-use planning practice* (in Czech). Brno: Agroprojekt.

[13] Miklós L. (1986). Stability of landscape in ecological general plan of SSR (in Slovak). *Životné prostredie. Volume 20(2),* 87-93.

DOI: 10.1515/sspjce-2019-0021

Improvement of cement stabilized structural lateritic with pulverized snail shell

Oluwaseun Adetayo, Olugbenga Amu, Sunday Alabi

Federal University Oye Ekiti, Ekiti State Nigeria
Faculty of Engineering Department of Civil Engineering
email: oluwaseun.adetayo@fuoye.edu.ng; tayo.seun4real@gmail.com

Abstract

This study investigated the suitability of pulverized snail shell (PSS) as partial replacement of cement stabilized soil in foundation constructions. Preliminary and engineering tests were carried out on the soil samples. The optimum cement content fixed at 11% in correlation to Unified Soil Classification System, the PSS was introduced at varying percentages of 2%, 4%, 6%, 8% and 10%. Results revealed that, addition of PSS and 11% cement to lateritic soil caused a reduction in both liquid limits and plasticity index and an increased in plastic limits for all samples. Engineering tests showed the maximum dry density at optimum cement increased from 1493.34 ± 103.58 kg.m^{-3} to 1632 ± 435.81 kg.m^{-3} for sample A; 1476.77 ± 367.51 kg.m^{-3} to 1668 ± 202.58 kg.m^{-3} for sample B; 1460.77 ± 623.58 kg.m^{-3} to 1651 ± 135.45 kg.m^{-3} for sample C. The CBR recorded highest value at 4%PSS optimum cement for all samples. The addition of pulverized snail shell increased the strength of cement stabilized lateritic soil for structural foundation construction.

Keywords: pulverized snail shell, cement stabilization, lateritic soil, structural foundation

1 Introduction

The problems with foundation on soils have included cracking, heaving and break up of pavements, building foundation, slab members, etc. as a result of these problems associated with poor soils, various methods are being developed worldwide to treat these soils is known as soil stabilization. Weak soils usually are attributed to excess ingression of groundwater, high shrinkage and swelling potential, high liquid limit and plasticity index and lack of strength. All these defects are usually associated to deformable properties of the soil. Murthy [1], observed that, treatment of weak soils can be done by preventing ingress of ground water flow or removing it from the site in question, or improving soil strength through a mechanical medium or chemical medium on the other hands. Cuneyt [2], similarly states that, if such soil cannot be removed, then its engineering behavior properties can be enhanced by suitable method of ground treatment. Das [3], states that soils with low strength are highly deformable, lack of strength leads to soil failure if overloaded. However, this has been frequent in occurrence in

civil engineering construction work due to some act of negligence being put up by some engineer when such problems are being encountered.

The various methods used to alter or improve soil properties such as their strength, settlement and bearing capacity are generally called soil stabilization techniques, which objectives are to improve on the volume stability, strength and stress-strain properties, permeability and durability. The concept of soil improvement or modification through stabilization with the use of additives has been around for several thousands of years. Although this process of improving the engineering properties of soils has been practiced for centuries, soil stabilization did not gain significance until after World War II [4]. Thousands of years ago, soils have already been stabilized with lime and other relevant available pozzolans. It has been proven that the benefits of using pozzolans materials in soil stabilization are both economic and technical. Several studies have been made on soil stabilization using different stabilizing agents. Pyne [5], showed the effectiveness of addition of calcium chloride to soil treatment. Lopez and Castano [6] used calcium oxide as a stabilization technique clay soils in order to inhibit its expansion contraction properties. Ghafoori and Cai [7], used coal combustion by-products in roller compacted concrete, roadway and parking lots. Muntohar and Gendut [8] and Muntohar [9], investigated the effect of fly ash and pozzolanic material on soil improvement. The use of pulverized snail shell as a soil stabilizer is not a common practice worldwide but research findings have shown the immense benefit and potential of using snail shell powder as pozzolans in soil.

However, much researches have not been done on the performance of pulverized snail shell on cement stabilized soil. Snail shell gotten from the consumption of fleshy edible part of snail is a waste product that can lead to land population if not effectively managed. The shell comes in form of V-shaped spiral shell found in many coastal regions, especially here in Nigeria. The shells are a strong, hard and brittle material. The shells constitute waste and its disposal is posing problems in areas where they have no use for it [10]. It is in this light that this experimental study seeks to investigate into the suitability of pulverized snail shell as a complement for cement in soil stabilization by way of considering the effects of pulverized snail shell on cement-stabilized lateritic soil.

1.1 Lateritic Soils

Lateritic soils, one of the least fertile soil types, are found in wetter and hotter climates [11]. Lateritic soils may contain clay minerals but they tend to be silica-poor, for silica is leached out by waters passing through the soil. Typical laterite is porous and claylike. It contains the iron oxide minerals goethite FeO(OH), lepidocrocite $FeHO_2$, and hematite Fe_2O_3. It also contains titanium oxides and hydrated oxides of aluminum, the most common and abundant of which is gibbsite $Al(OH)_3$. The aluminum-rich representative of laterite is bauxite. Laterite is frequently pisolitic (pealike). Exposed surfaces are blackish-brown to reddish and commonly have a slaggy, or scoriaceous, lavalike appearance. Commonly lighter in colour (red, yellow, and brown) where freshly broken, it is generally soft when freshly quarried but hardens on exposure. Laterite is not uniquely identified with any particular parent rock, geologic age, single method of formation, climate per se, or geographic location. It is a rock product that is a response to a set of physiochemical conditions, which include an iron-containing parent rock, a well-drained terrain, and abundant moisture for hydrolysis during weathering, relatively high oxidation potential, and persistence of these conditions over thousands of years.

Laterite is a very widespread soil group. Lateritic soils occur in all wet tropical regions, e.g. East, West and Central Africa, Indonesia, Thailand, Brazil and various island such as Hawaii and Cuba Lateritic soils are residual soils formed in hot, wet tropical regions with an annual rainfall between 750mm and 3000mm or more. The main soil forming process consists of intensive weathering with leaching of bases and silica resulting in a relative accumulation of iron and aluminum oxides and formation of kaolinitic clays. Intensive weathering producing deep Laterite profile occurs on flat slopes in the terrain where runoff is limited.

Laterite mainly occurs as:

- Surface deposits of unhardened, clayey soils
- Massive rock- like hardpans
- Gravel consisting of concretionary nodules in a soil matrix.

1.2 Soil Improvement

In foundation engineering practice the soils at a given site are often less than ideal for the intended purpose. They may be weak, highly compressible, or have a higher permeability than desirable from an engineering or economic point of view. It would seem reasonable in such instances to simply relocate the structure or facility. However, considerations other than geotechnical often govern the location of a structure, and the engineer is forced to design for the site at hand. One possibility is to adapt the foundation to the geotechnical conditions at hand or otherwise to try to stabilize or improve the engineering properties of the soils at the site. Depending on the circumstances, this second approach may be the most economical solution to the problem. Stabilization is the process of blending and mixing materials with a soil to improve the pertinent properties of the soil. The process may include the blending of soils to achieve a desired gradation or the mixing of commercially available additives that may alter the gradation, change certain properties, or act as a binder for cementation of the soil. Stabilization is usually mechanical or chemical, thermal and electrical stabilization have occasionally been used or considered.

Mechanical stabilization or densification is also called compaction. Chemical stabilization includes the mixing or injecting of chemical substances into the soil. Portland cement, lime, asphalt, calcium chloride, sodium chloride and paper mill waste are common chemical stabilization agents. Other methods of stabilizing unsuitable foundation soils include dewatering which is the removal or reduction of unwanted excess ground water pressure, and preloading, in which the foundation soil are surcharged with a temporary overload so as increase the strength and decrease anticipated settlement [12].

1.3 Pozzolanic Reaction

Pozzolans are siliceous or siliceous and aluminous materials which in themselves do not possess any cementitious value but in finely divided form and in the presence of moisture will chemically react with calcium hydroxide (CH) to form a compound with cementitious value according to this general equation:

$$Ca(OH)_2 + H_4SiO_4 \rightarrow Ca^{2+} + H_2SiO_4^{2-} + 2\,H_2O \rightarrow CaH_2SiO_4 \cdot 2H_2O \quad (1)$$

Which can be summarized in abbreviated notation of silicate chemists;

$$\text{Pozzolans} + \text{CH} \rightarrow \text{C-S-H} \quad (2)$$

Calcium silicate hydrates (C-S-H) is the strength-forming products of cement hydration. Pozzolans can be classified as artificial if firing (or calcination) is required to induce pozzolanicity and natural if no calcination is required. The product of general formula ($CaH_2SiO_4 \cdot 2H_2O$) formed is a calcium silicate hydrate, also abbreviated as CSH in cement chemist notation. The ratio Ca/Si, or C/S, and the number of water molecules can vary and the above mentioned stoichiometry may differ. As the density of CSH is lower than that of portlandite and pure silica, a consequence of this reaction is a swelling of the reaction products. This reaction may also occur with time in concrete between alkaline cement pore water and poorly-crystalline silica aggregates. This delayed process is also known as alkali silica reaction, or alkali-aggregate reaction, and may seriously damage concrete structures because the resulting volumetric expansion is also responsible for spalling and decrease of the concrete strength. The pozzolanic reaction may be slower than the rest of the reactions that occur during cement hydration, and thus the short-term strength of concrete made with pozzolans may not be as high as concrete made with purely cementitious materials; conversely, highly reactive pozzolans, such as silica fume and high reactivity metakaolin can produce "high early strength" concrete that increase the rate at which concrete gains strength.

2 Materials and Methods

The materials used include lateritic soil samples, Ordinary Portland cement, pulverized snail shell and water. The lateritic soil samples were collected from burrow pits within Obafemi Awolowo University along Road 7, Ile-Ife in Osun State Nigeria. These were designated as samples A, B and C. The soil samples pre-treatment was ensured before the commencement of the study. For easy identification of the soil samples, tags were placed on them to describe their dates of excavation, depths of excavation from the source and locations. The soil samples were spread on sacks in the laboratory to air-dry them for a minimum of two weeks, preventing water contamination and direct sunlight contact and local drying was prevented by frequently turning of the sacks of soil samples. This was later sieved with sieve No. 4 (4.76mm opening) to obtain the final soil sample. The required quantity of Ordinary Portland cement manufactured by West African Portland Cement Plc (WAPCO) Ota, Ogun State was obtained locally, and kept in a safe platform to prevent any contact with moisture and any other external affection of its properties. Portable mixing water was obtained from treated water available in the laboratory. The pulverized snail shells were obtained from snail shells (fig. 1.) collected from different locations in Ibadan area. The fleshy parts were removed from the shell, then the empty shells were thoroughly washed, air-dried for one week and calcined in an electric muffle furnace at 850° C. It was then grounded into fine powder particles form with the aid of ball milling machine. The ash obtained was later sieved through 75μm and kept in a sack bag to prevent it from moisture and any other external influences that can affect its properties as specified in both BS:1924 [13] and ASTM C618-93 [14] requirements.

Figure 1: Snail Shells (Locally sourced)

Preliminary tests such as the natural moisture content, specific gravity, particle size analysis and Atterberg's limits were carried out on three unstabilized soil samples to determine their index properties. The cement being the major stabilizing material, was thoroughly mixed with the soil samples at a fixed dosage of 11% with respect to the soil classification and varying percentages of (2, 4, 6, 8 & 10%) of the pulverized snail shell by weight of the soil samples. This was done in conjunction with the liquid limit and the determined plasticity index (PI) from Atterberg's limit test. The point of lowest PI gives the optimum amount of cement required. Hence, engineering properties of cement stabilized soil was determined. These engineering properties are used as the control against which the engineering properties of cement stabilized lateritic soil modified with pulverized snail shell are compared. The main objective of the study is to determine the change in the engineering properties of the stabilized soil sample modified with pulverized snail shell.

Engineering tests such as compaction, California bearing ratio (CBR) and undrained traixial were also performed on soil samples at their natural states, when stabilized with optimum cement and when pulverized snail shell (PSS) was introduced as pozollan to the samples. The various tests were carried out with standard procedures stipulated in BS 1377: [15].

3 Results and Discussion

The results from the preliminary tests (grain size analysis, natural moisture contents, specific gravity, and Atterberg's limits test) as well as the engineering test (compaction test, California Bearing Ratio test and triaxial test) are presented and discussed below.

3.1 Preliminary Test

The summary of the preliminary test results for soil samples A, B, C are shown in Table 1. The natural moisture content of the selected soil samples A, B and C are 7.06%, 7.87% and 7.68% respectively. The result showed that sample B has the highest natural moisture content and sample A the lowest. Lambe and Whiteman [16] stated that the moisture content of a soil

depends largely on void ratio, thus the results could be attributed largely to the void and the specific gravity. Sample A probably has a largest void ratio compared to the others. These also show that the soil samples still contain some appreciable amount of moisture, which is largely affected by the climatic condition. The specific gravity of samples A, B and C are 2.684, 2.500 and 2.273 respectively. These values ranges within what Das [3] stated, that for most clay minerals, there specific gravity fall within a general range (1.6-3.2), a Halloysite (1.60-2.55) and Biotite (2.8-3.2) which indicated that the soils are Halloysites. AASHTO soil classification system was used in the classification of the soil samples, the particle size analysis showed values of 67.4%, 51.2% and 61.2% passing the No. 200 sieves for Samples A, B and C respectively. Fajobi [17], classified soil into seven major groups A-1 to A-7, soil classified under groups A-l, A-2, A-3 are granular materials while soil classified under groups A-4, A-5, A-6 and A-7 is mostly silt and clay-type materials. Soil samples A, B and C classified as A-5 to A-7 according to the AASHTO table for classification [18] and the subgrade rating is rated as fair to poor and therefore will require stabilization as established by Sobhan and Das, [19].

Table 1: Summary of preliminary test for soil samples

Sample	Natural Moisture Content (%)	Specific Gravity	Percent retained (%)	Liquid Limit (LL) (%)	Plastic Limit (PL) (%)	Plastic Index (PI) (%)
A	7.06	2.684	67.40	73.88	27.27	46.61
B	7.87	2.500	51.20	65.95	33.72	32.23
C	7.68	2.273	61.20	60.40	30.83	29.57

3.2 Cement stabilization

The liquid limits, plastic and plasticity index of 73.88%, 27.27% and 46.61% for sample A, 65.95%, 33.72% and 32.23% for sample B, 60.40%, 30.83% and 29.57% for sample C respectively without any additives. Gidigasu [20], stated that liquid limit less than 35% indicates low plasticity, between 35% and 50% indicates intermediate or medium plasticity, between 50% and 70% high plasticity and between 70% and 90% very high plasticity. On this note, the three samples have high plasticity. There was overall improvement in the plasticity of the samples as the variation in results of the Atterberg's limits tests for the soil samples on addition of the optimum cement dosage of 11% based on the Unified Soil Classification System showed significant reduction in both liquid limits and plasticity index and increase in plastic limits for all the soil samples as shown in Figures 2 to 4 for samples A, B and C respectively, further improvement observed in both samples as there were further reduction in both the plastic limit and plasticity index on addition of 11% cement and 6% pulverized snail shell (PSS).

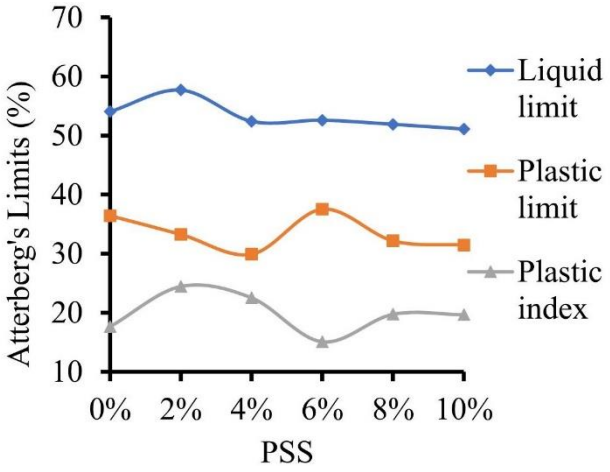

Figure 2: Variation of Atterberg limits with varying PSS at fixed 11% cement dosage for Sample A

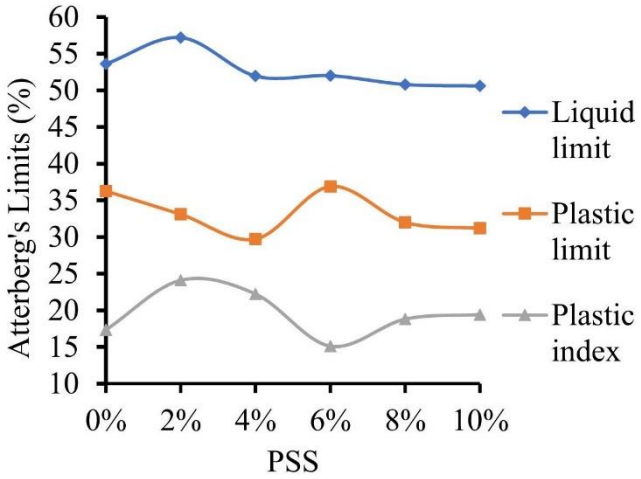

Figure 3: Variation of Atterberg limits with varying PSS at fixed 11% cement dosage for Sample B

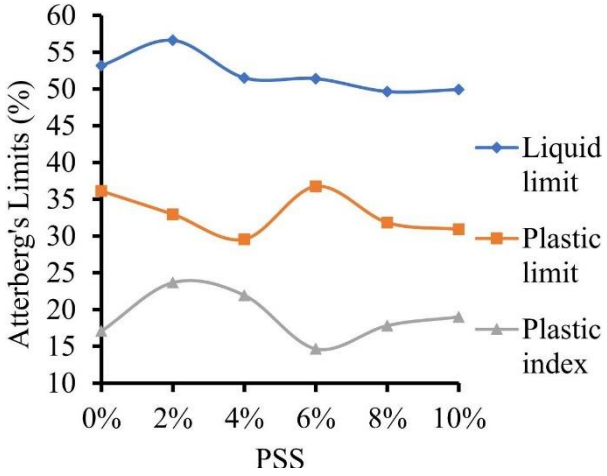

Figure 4: Variation of Atterberg limits with varying PSS at fixed 11% cement dosage for Sample C

The reduction in plasticity index exhibited by all the three samples shows the effect of addition of 11% cement and 6% PSS for all the soil samples. Das [21] explained that cement can be used to stabilize sandy and clayey soils. As in the case of lime, cement helps decrease the liquid limit and increase the plasticity index and workability of clayey soils. Which is effective for clayey soils when the liquid limit is less than 45 to 50 and the index is less than about 25.

3.3 Engineering Strength Tests

The compaction test was carried out to determine the optimum moisture content (OMC) and the maximum dry density (MDD) of the three soil sample at the natural state, stabilization with optimum cement dosages and addition of the pulverized snail shell (PSS).

The natural soil sample has an OMC of 24.07%, 24.5%, 25.67% and an MDD of 1493.34kg/m^3, 1476.77kg/m^3, 1460.77kg/m^3 for sample A, B and C respectively. Stabilization with 11% cement reduced the OMC to 22.33% and increased the MDD to 1632kg/m^3 for sample A, reduced the OMC to 22.5% and increased the MDD to 1668kg/m^3; for sample B, reduced the OMC to 21.27% and increased the MDD to 1651kg/m^3 for sample C. The increase in the MDD can be attributed to the replacement of the soil by the cement particles which have lower specific gravity compared to that of the soil. It may also be attributed to coating of the soil by the powdery cement which result to large particles with larger voids and hence less density [22]. Lambe and Whiteman [16] stated that, for good soil, the lower the OMC, the better its workability and an increase in dry density is an indicator of soil improvement. The decrease in OMC with addition of cement can be attributed to increasing demand for water by various cations and the clay mineral particles to undergo hydration reaction. The addition of PSS at (2%, 4%, 6%, 8%, and 10%) and 11% cement to the soil samples caused a decrease in the MDD and an increase in OMC of all the soil samples. The increase in the OMC confirmed the pozzolanic behavior of PSS with an increasing demand for water to react and form aggregate molecules in the soil. Table 2 showed the result of MDD and OMC of the variation in mix percentage of PSS at optimum cement dosage.

Table 2: Summary of Compaction test on cement stabilized samples and varying pulverized snail shell (PSS)

Samples	Percentage Stabilization (% PSS)	Optimum Moisture Content (%)	Maximum Dry Density ($kg.m^{-3}$)
A	0	22.33	1632 ± 435.81
	2	25.04	1621 ± 411.43
	4	26.70	1627 ± 409.86
	6	25.04	1650 ± 399.45
	8	25.75	1611 ± 409.82
	10	30.52	1541 ± 422.63
B	0	22.50	1668 ± 202.58
	2	25.01	1655 ± 186.97
	4	25.68	1612 ± 309.34
	6	25.03	1634 ± 278.65
	8	24.52	1638 ± 266.69
	10	31.49	1525 ± 213.24
C	0	21.27	1651 ± 135.45
	2	26.99	1642 ± 198.23
	4	25.66	1595 ± 200.61
	6	26.01	1611 ± 166.03
	8	23.51	1621 ± 133.05
	10	32.50	1510 ± 176.52

The unsoaked CBR values for the natural and cement-stabilized soil samples is shown in Figure 5. The CBR test were conducted at OMC of the soil, soil-cement or soil cement-PSS as determined from the compaction test. The CBR tests were performed immediately after compaction. The unsoaked CBR values for the natural soil were found to be 3% for samples A and C and 2% for sample B. Stabilization with 11% cement increased the CBR value of sample A to 12%, sample B to 13% and 11% for sample C. Results of the unsoaked CBR fluctuated when addition of PSS at (2%, 4%, 6%, 8%, 10%) and 11% optimum cement were introduced to the three soil samples with 4% PSS and 11% cement shows the highest value CBR value for all the samples.

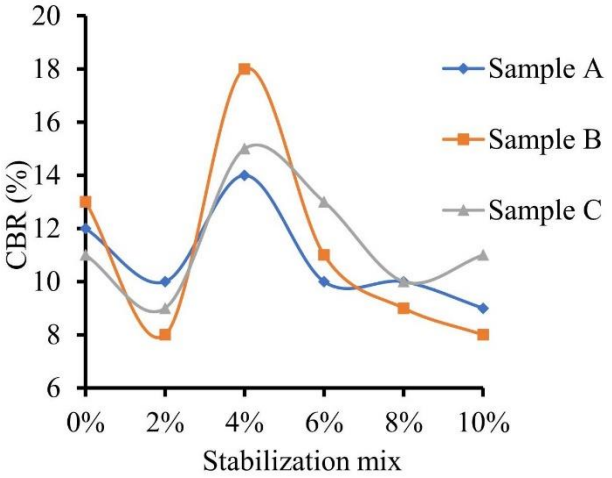

Figure 5: Variation of California bearing ratio with increasing PSS at 11% cement dosage

Figure 6 shows the variation of the shear strength with increasing PSS content. The shear strength values of samples are 56.48kPa, 51.45kPa and 48.05kPa, at natural state and 85.81kPa, 75.17kPa and 72.31kPa when stabilized at optimum cement of 11% for samples A, B, and C respectively. The addition of 2% SSP decreased the shear strength to 59.98kPa sample A, 66.72kPa sample B and increased to 80.89kPa for sample C. For sample A, the addition of 4% PSS, increased the shear strength but later decreased on addition of 6%, 8%, 10% PSS. For sample B, the addition of PSS at 4% and 6% PSS increased the shear strength but decreased on addition of 8%, 10% PSS. For sample C, the addition of PSS at 4%, 6% and 8% increased the shear strength values but and later decreased on addition of 10%.

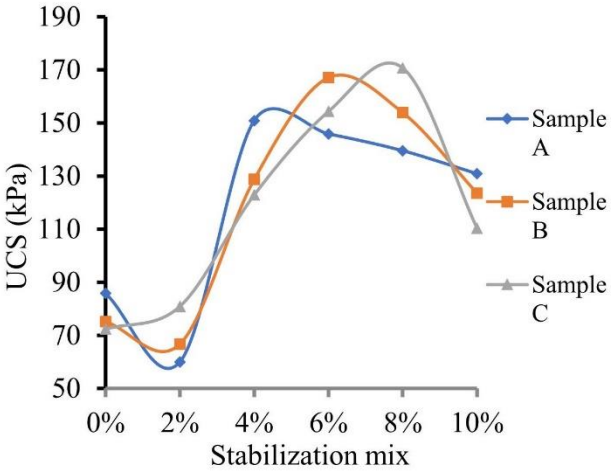

Figure 6: Variation of unconfined compressive strength with increasing PSS at 11% cement dosage

4 Conclusion

The cement stabilized with pulverized snail shell to subsoil showed significant improvement in the properties of the soil generally. The addition of 11% optimum cement reduced the liquid limit of soil samples A, B and C and a further reduction were noticed when PSS at 4%, 6%, 8% and 10% were added for all samples. Stabilization with 11% cement reduced the optimum moisture content and increased the maximum dry density of soil samples, for most soils, the lower the OMC, the better its workability and an increase in dry density is an indicator of soil improvement.

The unsoaked CBR values for the cement stabilized soil samples increased with the addition of optimum percentage of 11%. The CBR values for the cement-stabilized soil samples A and B further increased with addition 4% PSS, for sample C, the increase was at both 4% and 6% PSS. There was substantial increase in shear strengths for the cement stabilized soil samples and addition of PSS on the cement stabilized soil samples at all percentages, the highest shear strengths being observed at 4%, 6% and 8% PSS for all soil samples. The optimum stabilization value ranges between 4% to 8% pulverized snail shells for cement stabilized samples. In summary, this study has shown through literature review and experimental work that pulverized snail shell is a good complement for cement stabilization in lateritic soils.

References

[1] Murthy, V.N.S., (2002). *Geotechnical Engineering.* Marcel Dekker, Inc, New York.

[2] Cuneyt, T., (2000). Synthesis of Biomimetic Ca-Hydroxyapatite Powders at 37°C in Synthetic Body Fluids. *Biomaterials 21*:1429-1438.

[3] Das, B. M., (2000). *Fundamentals of Geotechnical Engineering.* Thompson Learning California.

[4] Ingles, O. G., and Metcalf, J. B., (2002). *Soil Stabilization Principles and Practice*. Butterworth's Publishers Boston.

[5] Pyne, A. L., (1995). *Comparative Biochemistry and Physiology Volume 29* (Issue 2), May 2001, Pages 611-620.

[6] Lopez, E. D., and Castano, P. K., (2001). *Foundation Design and Construction, 7th ed*. Pearson Educational Limited. Harlow, England.

[7] Ghafoori, R., and Cai, W., (1997). *Introduction to Geotechnical Engineering,* Prentice-Hall, Inc Englewood Cliffs, New Jersey.

[8] Muntohar, G. D., and Gendut, K. A., (2000). *Soil Mechanics in Engineering Practice 3rd Ed.,* John Wiley & Sons, Inc.

[9] Muntohar, G. D., (1999). *Soil Mechanics in Engineering Practice 3rd Ed.,* John Wiley & Sons, Inc.

[10] Zaid, S. T., and Ghorpade, V. G. (2014a). Experimental Investigation of Snail Shell Ash as Partial Replacement of Ordinary Portland Cement in Concrete. *International Journal of Engineering Research and Technology (IJERT) Vol. 3* (Issue 10).

[11] Microsoft® Student, (2009). DVD, Snail, Redmond, WA: Microsoft Corporation.

[12] Kovacs, W.D., and Holtz, R.D., (1981). *Introduction to Geotechnical Engineering. 2nd ed.* Prentice-Hall, Pearson Educational Limited.

[13] British Standards (BS) 1924. (1990a). Methods of Test for Stabilized Soils. British Standards Institutions. London, U. K.

[14] ASTM C618-93 Specification (1992). Fly Ash and Raw or Calcined Natural Pozzolan for Use as mineral Admixture in Portland Cement Concrete. Washington, D.C.

[15] British Standards (BS) 1377-1 (2016). Methods of test for soils for civil engineering purposes. General requirements and sample preparation.

[16] Lambe, T. W., and Whiteman, R. V., (1979). *Soil Mechanics,* John Wiley and Sons Inc, USA.

[17] Fajobi, A.B., (2008). *Unpublished Lecture Notes on Geotechnical Engineering I,* Department of Civil Engineering, Faculty of Technology, Obafemi Awolowo University, Ile-Ife.

[18] AASHTO, (1986). Soil Classification System (from AASHTO M 145 or ASTM D3282)

[19] Sobhan, K., and Das, B. M. (2007) Durability of Soil-Cements against Fatigue Fracture. *Journal Materials in Civil Eng., 19*(1): 26-32.

[20] Gidigasu, M.D., (1973). Degree of Weathering in the Identification of Laterite Materials for Engineering Purposes, *Journal of Engineering Geology, Vol. 8,* No. 3: 213-266.

[21] Das, B. M., (2008). *Advanced Soil Mechanics, 3rd Edition*, CRC Press, New York, Emmanuel, Visual Inspection of Concrete, http://www.montrealhomeinspectorpro.ca/en/home-inspection-articles/view/560/Visual-Inspection-of-Concrete

[22] Guyer, J. P., Guyer, P. E., and Guyer, R. A., (2011). *An Introduction to Soil Stabilization for Pavements.* Continuing Education and Development, Inc, New York.

DOI: 10.1515/sspjce-2019-0022

Degradation model of turnout wear according to frog material

Ján Urda, Ján Mandula

Technical University of Košice, Slovakia
Civil Engineering Faculty, Institute of Structural Engineering
e-mail: urda.jan@zsr.sk, jan.mandula@tuke.sk

Abstract

This paper describes the evaluation of the measured data from the turnout wear in relation to material from which the frogs are made. The evaluation consists in comparing the measured results with the data provided by the manager of these turnouts.

Key words: turnouts, rail, vertical wear, correlation analysis, regression analysis

1 Introduction

The basic and important condition for efficient management and maintenance of the railway infrastructure is to know its real condition. The way to this knowledge is the system of measurement, monitoring and diagnostics of the railway infrastructure.
One of the method of turnout diagnostics is also measuring the wear of mobile components, especially tongues and frogs. Excessive wear of frogs, especially on modernized sections of ŽSR lines is becoming an increasing problem. ŽSR Research and Development Institute of Railways in Žilina, within the framework of research and development tasks, monitors the frogs of 40 turnouts on the ŽSR network in the district of the Regional Directorate Trnava.

2 Scope of monitoring

Within the monitoring, 40 pieces of frogs were selected in the railway stations: Veľké Kostoľany (6 pcs), Piešťany (7 pcs), Nové Mesto nad Váhom (6 pcs), Leopoldov (8 pcs), Brestovany (4 pcs) and Trnava (9 pcs).
Due to the limited scope of the paper, only measurements of frog wear in relation to the material from which frogs are made are evaluated here. CONTOUR laser device (Figure 1) was used to measure wear.

Figure 1: CONTOUR device

The following parameters were measured on turnouts:
– horizontal wear,
– vertical wear,
– wing rail wear,
– wear of crossing nose,
– flangeway width,
– flangeway depth.

According to the ŽSR valid Regulation "TS 3 Railway superstructure", it is allowed during operation the greatest vertical wear of the frog at the place where the nose width is 40 mm and more, at the permitted speed:
– $V \geq 100$ km/h, not more than 6 mm,
– 40 km/h $< V <$ 100 km/h, not more than 9 mm,
– $V \leq 40$ km/h, not more than 12 mm.

The values of frog vertical wear are measured in the longitudinal direction as the difference between the top of the point rail and point of measurement at the crossing nose where its width is 40 mm (Figure 2).

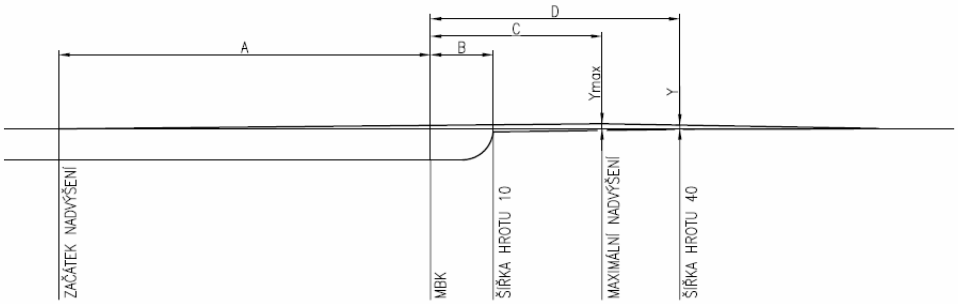

Figure 2: Longitudinal section of frog

In the next section, we will focus on the evaluation of wear of the monitored set of frogs depending on material from which they are made according to Table 1.

Table 1: Classification of measured turnouts according to frog material

Order	Railway station	Number of turnouts	Turnout type	Frog´s steel		
				Rail	Manganese	Bainitic
1.	Veľké Kostoľany	4	J 60 1:9 300		x	
2.	Veľké Kostoľany	5	J 60 1:9 300		x	
3.	Veľké Kostoľany	11	J 60 1:9 300		x	
4.	Veľké Kostoľany	13	J 60 1:14 760		x	
5.	Veľké Kostoľany	16	J 60 1:14 760		x	
6.	Veľké Kostoľany	15	J 60 1:14 760		x	
7.	Piešťany	4	J 60 1:18,5 1200		x	
8.	Piešťany	6	J 60 1:14 760		x	
9.	Piešťany	15	J 60 1:14 760		x	
10.	Piešťany	11	J 60 1:14 760		x	
11.	Piešťany	1	J 60 1:18,5 1200			x
12.	Piešťany	18	J 60 1:14 760		x	
13.	Piešťany	20	J 60 1:12-500		x	
14.	Nové Mesto n. V.	16	J 60 1:9 300		x	
15.	Nové Mesto n. V.	1	J 60 1:18,5 1200		x	
16.	Nové Mesto n. V.	4	J 60 1:9 300		x	
17.	Nové Mesto n. V.	5	J 60 1:18,5 1200		x	
18.	Nové Mesto n. V.	50	J 60 1:18,5 1200		x	
19.	Nové Mesto n. V.	43	J 60 1:11 300		x	
20.	Leopoldov	4	J 60 1:18,5 1200			x
21.	Leopoldov	22	J S49 1:9 300	x		
22.	Leopoldov	23	J S49 1:14 760	x		
23.	Leopoldov	6	J S49 1:9 300	x		
24.	Leopoldov	11	J 60 1:14 760			x
25.	Leopoldov	15	Ob 60 1:14 760			x
26.	Leopoldov	17	Ob 60 1:14 760			x
27.	Leopoldov	13	J 60 1:14 760			x
28.	Brestovany	1	J 60 1:18,5 1200		x	
29.	Brestovany	2	J 60 1:18,5 1200		x	
30.	Brestovany	3	J 60 1:18,5 1200		x	
31.	Brestovany	4	J 60 1:18,5 1200		x	
32.	Trnava	81	J 60 1:9 300			x
33.	Trnava	82	J 60 1:12 500			x
34.	Trnava	96	J 60 1:18,5 1200			x
35.	Trnava	92	J 60 1:18,5 1200			x
36.	Trnava	97	J 60 1:18,5 1200			x
37.	Trnava	87	J 60 1:11 300			x
38.	Trnava	86	J 60 1:12 500			x
39.	Trnava	78	J 60 1:12 500			x
40.	Trnava	69	J S49 1:12 500	x		

Based on material analysis, according to Table 2, the frogs are divided into three groups of steel:

– rail,
– manganese,
– bainitic.

Table 2: Division of the sample according to the frog material

Type of steel	rail	manganese	bainitic
Number	4	22	14

3 Evaluation according to material from which the frog is made

The high demands are placed on steels for the manufacture of mobile turnout components, mainly on impact resistance, toughness, abrasion, adhesion and corrosion wear resistance. Most often, frogs are made of classic rail steel, austenitic manganese steel, perlitized steel and bainitic steel.

3.1 Evaluation of turnouts with rail steel frogs

To determine the regression equation of dependence of the maximum value of the determining quantity and the time, 24 measurements are included for this turnout shape.
A graphical representation of the relations of correlation and regression analyses according to criterion of frog material h_v/t is shown in Figure 3. The calculation of the shortest frog degradation time is described by a linear equation (1).

$$t = \frac{|h_v|_{lim} + 0{,}0305}{0{,}0145} \ (months) \tag{1}$$

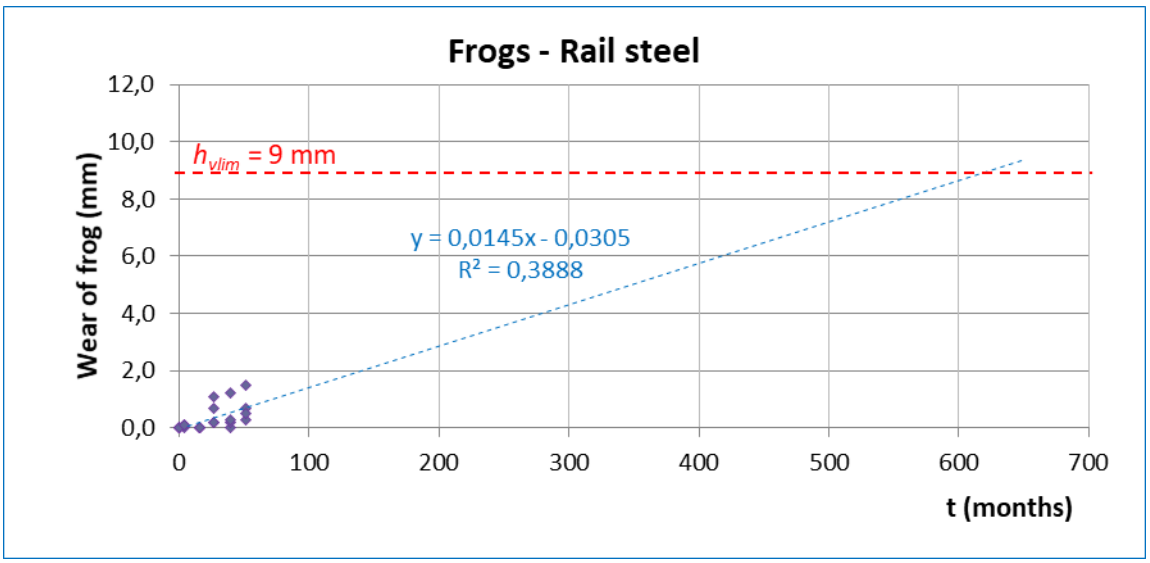

Figure 3: Graphical representation of relations of correlation and regression analyses $|h_v|_{lim}/t$ of turnouts with rail steel frogs

Table 3: Linear course of wear of turnouts with rail steel frogs

Type of steel	*n*	*a*	*b*	*c*	$R_{\alpha 0,05}$	*R*	Complies?	Course
rail	24	0,0305	0,0145	-	0,4044	0,624	yes	linear

Based on the results of the regression and correlation analyses of the relationship between the absolute value of the maximum determining quantity (vertical wear) and time, it can be assumed that the evaluated quantity will reach in time the limit value according to Regulation [1] over 52 years, provided that the current state of the 3rd-order operating load and maintenance, i.e. regular grinding, inter alia, with a period of once a year, is maintained, while the lifetime of turnouts on the ŽSR network is expected to be 20-30 years.
The accuracy of the prediction of the time to reach the determined degradation level $|h_v|_{lim}$ can currently be denoted as lower (R^2 = 0.3888) but it can be assumed that it will increase by adding data from future measurements.

3.2 Evaluation of turnouts with manganese steel frogs

To determine the regression equation of dependence of the maximum value of the determining quantity and the time, 132 measurements are included for this turnout shape.
A graphical representation of the relations of correlation and regression analyses according to criterion of frog material h_v/t is shown in Figure 4. The calculation of the shortest frog degradation time is described by the linear equation (2).

$$t = \frac{|h_v|_{lim} + 0{,}0782}{0{,}0333} \ (months) \tag{2}$$

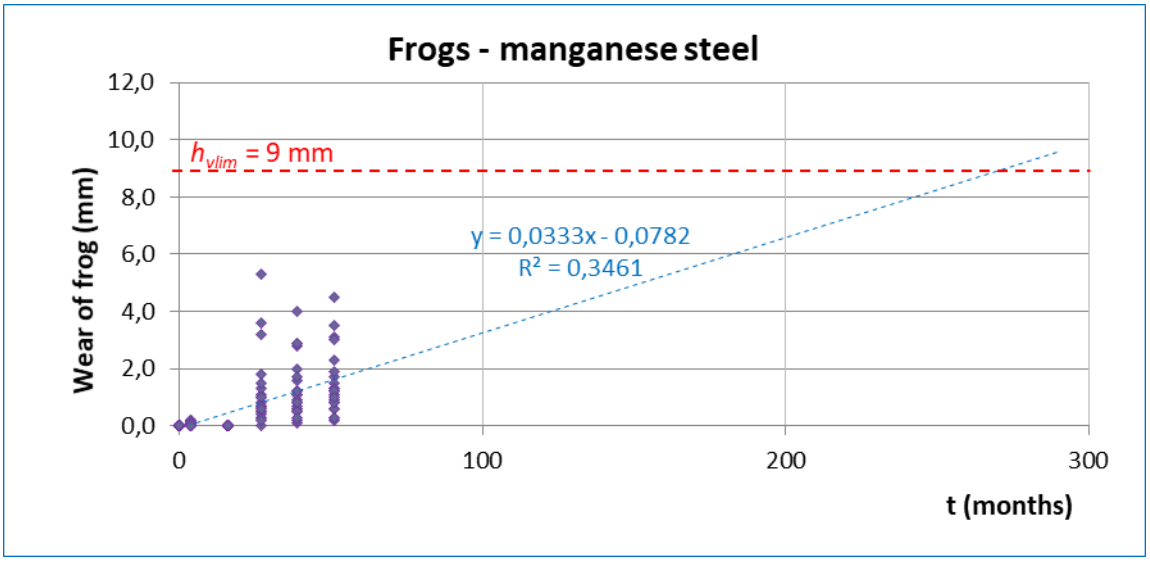

Figure 4: Graphical representation of relations of correlation and regression analyses $|h_v|_{lim}/t$ of turnouts with manganese steel frogs

Table 4: Linear course of wear of turnouts with manganese steel frogs

Type of steel	*n*	*a*	*b*	*c*	$R_{\alpha 0,05}$	*R*	Complies?	Course
manganese	132	0,0782	0,0333	-	0,1627	0,588	yes	linear

Based on the results of the regression and correlation analyses of the relationship between the absolute value of the maximum determining quantity (vertical wear) and time, it can be assumed that the evaluated quantity will reach in time the limit value according to Regulation [1] over a period of 23 years, provided that the current state of the 3rd-order operating load and maintenance, i.e. regular grinding, inter alia, with a period of once a year, is maintained, while the lifetime of turnouts on the ŽSR network is expected to be 20-30 years.
The accuracy of the prediction of the time to reach the determined degradation level $|h_v|_{\text{lim}}$ can currently be denoted as lower (R^2 = 0.3461) but it can be assumed that it will increase by adding data from future measurements.

3.3 Evaluation of turnouts with bainitic steel frogs

To determine the regression equation of dependence of the maximum value of the determining quantity and the time, 84 measurements are included for this turnout shape.
A graphical representation of the relations of correlation and regression analyses according to criterion of frog material h_v/t is shown in Figure 5. The calculation of the shortest frog degradation time is described by the linear equation (3).

$$t = \frac{|h_v|_{lim} + 0{,}038}{0{,}0175}\ (months) \tag{3}$$

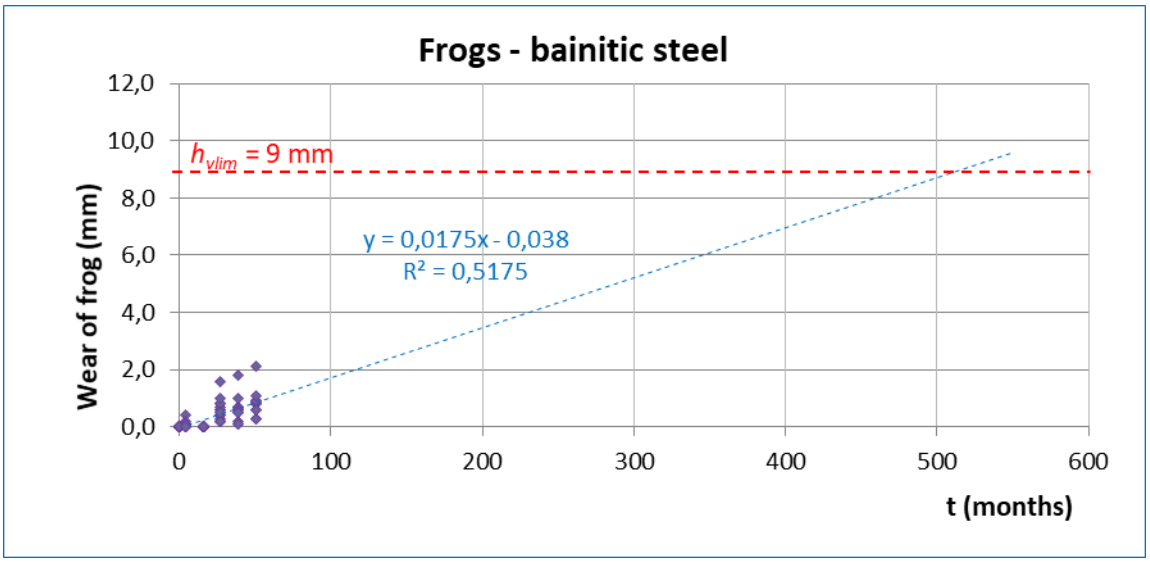

Figure 5: Graphical representation of relations of correlation and regression analyses $|h_v|_{\text{lim}}/t$ of turnouts with bainitic steel frogs

Table 5: Linear course of wear of turnouts with bainitic steel frogs

Type of steel	*n*	*a*	*b*	*c*	$R_{\alpha 0,05}$	*R*	Complies?	Course
bainitic	84	0,038	0,0175	-	0,2148	0,719	yes	linear

Based on the results of the regression and correlation analyses of the relationship between the absolute value of the maximum determining quantity (vertical wear) and time, it can be assumed that the evaluated quantity will reach in time the limit value according to Regulation [1] over a period of 43 years, provided that the current state of the 3rd-order operating load and maintenance, i.e. regular grinding, inter alia, with a period of once a year, is maintained, while the lifetime of turnouts on the ŽSR network is expected to be 20-30 years.
The accuracy of the prediction of the time to reach the determined degradation level $|h_v|_{\text{lim}}$ can currently be denoted as intermediate ($R^2 = 0.5175$) but it can be assumed that it will increase by adding data from future measurements.

4 Evaluation

When comparing the impact of grinding or non-grinding of frogs in relation to material from which the frog is made, the manganese steel frogs were achieved the greatest wear (5.3 mm) and the lowest values were achieved by rail steel frogs (1.5 mm) (Figure 6). The limit value of wear would achieve first the manganese steel frogs in 23 years and at latest the rail steel frogs in 52 years.

Table 6: Evaluation according to frog material

Frog´s steel	R^2	Reaching limit value of wear according to Regulation [1] [year]	Lifetime order	
			evaluated	manager
rail	0,3888	52	3.	3.
bainitic	0,5175	43	2.	2.
manganese	0,3461	23	1.	1.

When comparing the results obtained with the data from the manager, we can conclude that these results coincide since he declared that the frogs of manganese steel withstand them the least, then the bainitic steel frogs and finally the rail steel frogs (Table 6).
In the case of manganese frogs it is also necessary to take into account the fact that ŽSR has not yet ground the decaburized layers, which need to be grind after the frog has been run in operation, therefore they have a low lifetime.

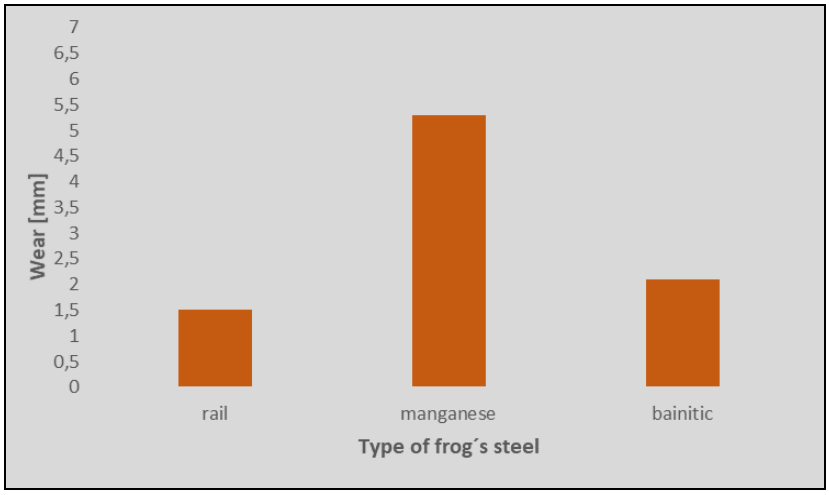

Figure 6: Graphical representation of measured maximum wear according to frog material

5 Conclusion

When evaluating the results in relation to the material from which the frog is made, it can be concluded that the manganese steel frogs achieved the greatest wear ant the lowest values were achieved by the rail steel frogs. The limit value of wear would achieve first the manganese steel frogs and at latest the rail steel frogs. When comparing the results with the data from the manager, we can conclude that these results coincide since he declared that the frogs of manganese steel withstand them the least, then the bainitic steel frogs and finally the rail steel frogs (Table 6).

References

[1] Regulation ŽSR TS 3 Railway superstructure

[2] Urda, J., Mandula, J., Urdová, A. Degradation model of wear frogs switches on the tracks ŽSR. XXIV R-S-P seminar, Theoretical Foundation of Civil Engineering. 24.-28. August 2015, Samara, Russia

[3] Urda, J., Mandula, J. Príspevok k modelovaniu opotrebovania srdcoviek výhybiek. 7. Medzinárodná vedecká konferencia pozemného staviteľstva a architektúry „Mladý vedec 2015“, 08.-10.04.2015, Jasná

[4] Urda, J., Klučka, M. Novelizácia predpisov ŽSR o meraní výhybiek a brúsení. 18. seminár traťového hospodárstva STRAHOS 2018, 19. – 20. apríl 2018, Banská Bystrica

[5] Urda, J., Mandula, J.: Degradation model of wear of frogs switches on the track. International journal of interdisciplinary in theory and practise. Nr.: 8 Year: 2015, Romania, ISSN: 2344 – 2409, ISSN-L: 2344 – 2409

DOI: 10.1515/sspjce-2019-0023

Theoretical background of ideal glazing based on adaptive thermal-optical parameters

Silvia Bizoňová

Technical University of Košice, Slovakia
Faculty of Civil Engineering, Institute of Architectural Engineering
e-mail: silvia.bizonova@tuke.sk

Abstract

The theoretical overview serves as a basis for the design of a separate adaptive glass system. An overview of current directions is processed, which reflects the actual user requirements in relation to the thermal comfort. The concept is based on knowledge and practical experience in the field of progressive glass systems today. It uses formulated shortcomings as a tool for their elimination in the further development of the future concept. It is based on the customization of the glass system as a means of achieving the optimal temperature state of the indoor environment in order to eliminate the additional need for cooling and heat for heating buildings.

Key words: U-factor, visible transmittance, total solar energy transmittance

1 Introduction

As a result of increasing demands on the heat-insulating ability of window structures, emphasis has been placed in the first place on the reduction of the U-factor, which is one of the main evaluation parameters of the window structure. One of the tools to achieve a reduction in the heat transfer coefficient has been and is to increase the heat-insulating ability of the sash, but this only affects the area by which it contributes to the overall window area. At the same time, glass systems were improved from single to double, and later triple with the use of low-emissivity layers. Further development of glass improvement is main aspect in different directions. One of them is to increase the number of glasses with the intention of increasing the total thickness of the insulating gas in the glass system in the form of four to six glasses [1, 2, 3, 4], which can achieve U_g up to 0.26 W/(m^2.K) in the center of the glass system without the use of low-emissivity layers [4]. However, this solution has not proved to be successful as the gas leakage due to sealant stress is too high [4] and the standard permits an annual gas leakage of 1% [5] and such glass systems are therefore not produced in series.

In general, sunlight falling on any structure is released, absorbed and reflected to some extent. This ratio is determined by the optical parameters of the structure. A sun radiation consists of a visible and invisible component of different wavelengths. By design, these components penetrate differently into interiors. In the case of a glass system, the quantity of the permeated component is defined by its thermal-optical parameters, which are the result of taking into account all layers of the glass system (declared by the manufacturer), but consisting of partial permeability of the individual layers (glass, low-E layer, gas gap). The invisible component represents approximately 50% of total solar energy [6]. By targeted selection of the composition of the glass system in the range of kinds of panes and low-emissivity layers, it is possible to regulate the heat gains in the desired manner.

In addition to the U-value (heat transfer coefficient), the thermal-optical properties of the glass system also contribute to g-value (total solar energy transmittance), τ_V (visible transmittance) and emissivity. g-value is calculated as the direct solar energy transmittance (T_{sol}) times the inward heat transfer coefficient of the glazing, which later results in heat transfer by convection and long-wave IR radiation of this energy from the incident solar radiation absorbed by the glazing [7,8].

2 Glazing species with constant thermal-optical properties

2.1 Single, double (multiple) glazing

The thermal-optical properties of insulating double and multiple insulating glass unit without the use of low-emissivity layers depend on the glass and insulating gas used as well as on the window angle closest to the horizontal. In all cases, we consider a 90° angle for the relevance of the information. Common 4 mm float glass has approximate parameters: U = 5.880 W/(m^2.K), τ_{vis} = 0.988(-), g = 0.868(-) (see Table 1), which may vary depending on the product. The results were obtained using Window 7.4.14 software from Lawrence Berkley University [9].

Table 1: Thermal–optical properties of multiple glass units

Glass unit	**Specification**	**Gas filling**	U_g **[W/(m^2.K)]**	τ_{VIS} **[-]**	g **[-]**
Single	4mm Float glass	-	5.880	0.988	0.868
Double	2x4mm Float	Air/Ar	2.591	0.813	0.774
Double	2x4mm Float	Air/Kr	2.554	0.813	0.774
Triple	3x4mm Float	Air/Ar	1.617	0.739	0.698
Triple	3x4mm Float	Air/Kr	1.590	0.739	0.698
Quadruple	4x4mm Float	Air/Ar	1.171	0.675	0.634
Quadruple	4x4mm Float	Air/Kr	1.114	0.675	0.635
Quintuple	5x4mm Float	Air/Ar	0.918	0.618	0.580
Quintuple	5x4mm Float	Air/Kr	0.890	0.618	0.581
Sixfold	6x4mm Float	Air/Ar	0.757	0.567	0.534
Sixfold	6x4mm Float	Air/Kr	0.726	0.567	0.535

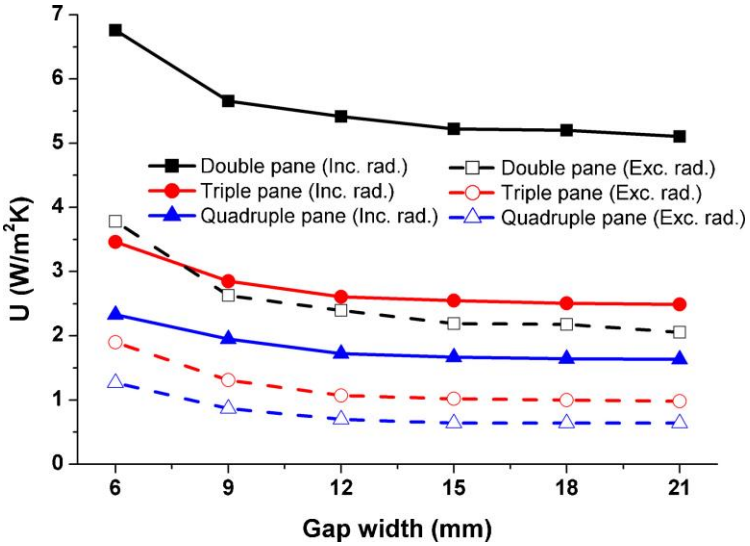

Figure 1: The effect of radiative heat transfer on the overall heat transfer coefficient (T_0=-25°C) [10].

Figure 1 presents the dependency between the thickness of the gas layer and the U-factor, with and without radiation considered. The graph shows that the greatest influence on U-factor is first of all the number of glass panes; the second most important is the emissivity of the surface and third is the thickness of the gas gap. Significant improvement of the U-factor can be achieved by forming a high-reflection layer on the glass surface. At a gas layer thickness of 9 mm, it is thus possible to achieve a U-factor change from 5.66 to 2.63 W/(m2.K). The thickness of the gas layer in terms of its impact on U-factor is only significant up to a thickness of 15 mm, for larger thicknesses the difference is negligible. Transmittance and reflectance of clear glass is demonstrated in Figure 2.

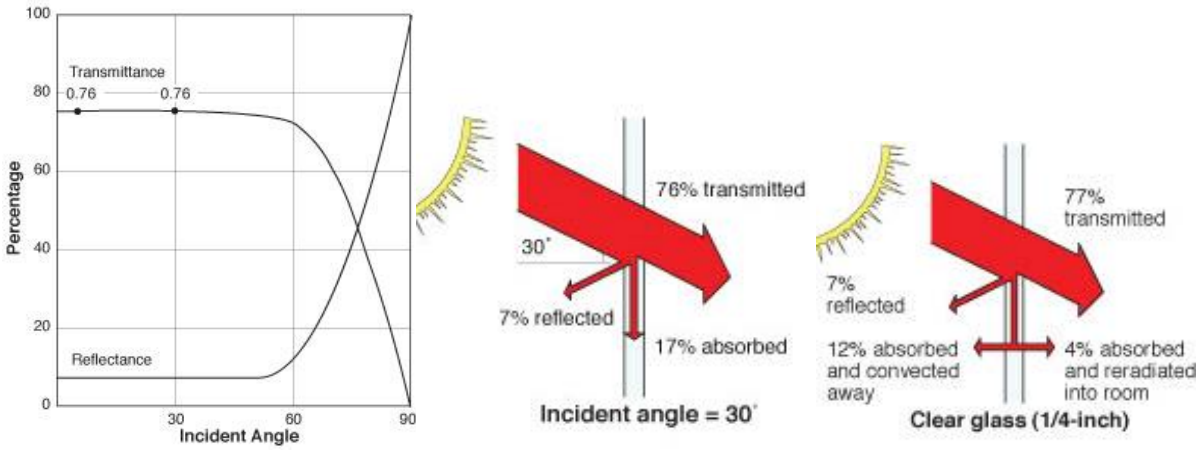

Figure 2: a) Sunlight transmitted and reflected by 6.35mm clear glass as a function of the incident angle, b) Solar energy transmission through the glass after standard ASHRAE conditions [11].

2.2 Low emissivity coated (double) glass unit

Metal layer between dielectric layers together forming transparent heat reflective coating is nowadays known as Low–E coating. Silver as an element which infrared reflectivity is high and absorption in visible part of spectra is low were chosen as a part of most metal compounds of low-emissivity coatings. However, since silver compounds have a moisture resistance problem resulting in, for example, white dots, aluminum is added to the compound to reduce such internal stresses [12]. Spectral properties of glazing of various low-E compounds are shown in Figures 3, 4. Film thickness were determined to obtain a peak transmittance of about 46% in the visible range, Figure 3.

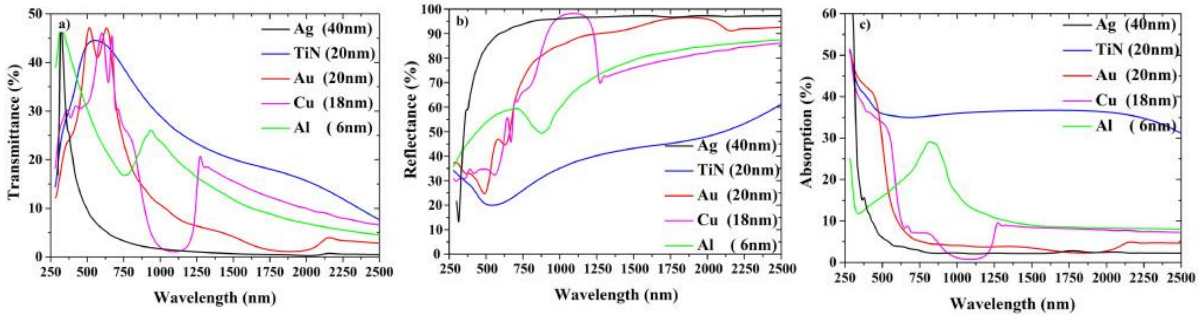

Figure 3: a) Transmittance b) Reflectance and c) Absorbance of Ag (40 nm), TiN (20 nm), Au (20 nm), Cu (18 nm) and Al (6 nm) for the UV-IR wavelength range [13].

A low-emissivity coating known as hard multilayer metal coatings can be applied to the exterior of the glass surface, but the soft coatings are positioned at position 2 from the exterior, i.e. on the exterior glass pane, on the surface in contact with the insulating gas due to atmospheric reactions. Abundiz-Cisneros [13] and his team are working on replacing silver in the compound with other elements to eliminate the problems associated with silver.

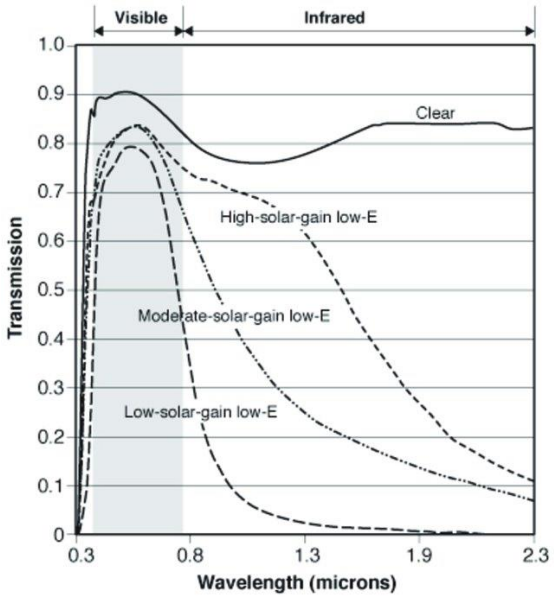

Figure 4: Spectral transmittance curves for glazing with three different types of low-emittance coatings. Image Credit: Lawrence Berkeley National Laboratory [14].

2.3 Water flow glazing

In case of water-filled prismatic louver which is designed to absorb solar infrared and ultraviolet radiation for harvesting energy, visible light pass for daylighting. The absorption spectrum of pure water shows that water has a low absorption coefficient at shorter wavelengths that increases over the visible light spectrum until the near infrared region and slighlitly depends on the thickness L, see Figure 5, [15]. Transmittance of water at room temperature is shown in Figure 6.

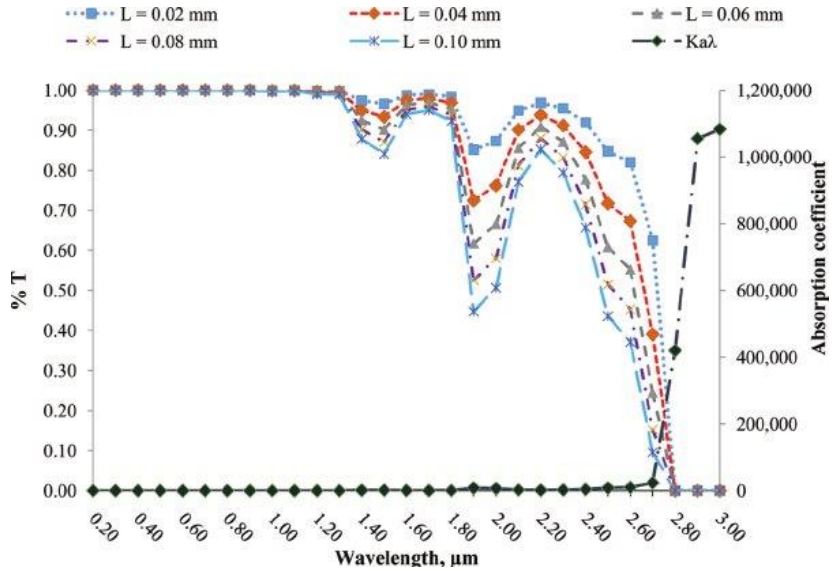

Figure 5: Transmissivity and absorption coefficient of pure water at various wavelengths [15]

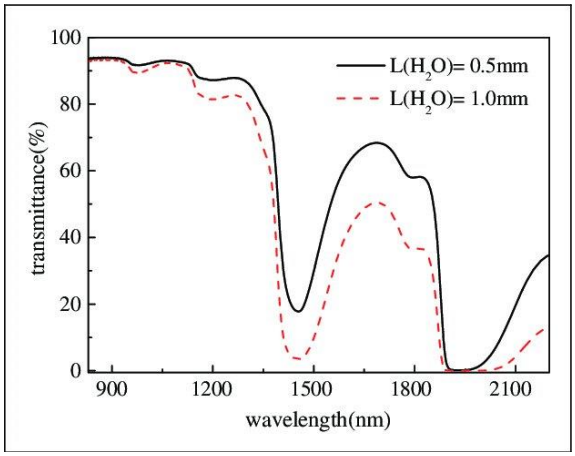

Figure 6: Measured transmittance spectra of water at room temperature [16].

2.4 Aerogel glazing

Due to the small size of material pores, the aerogels have a thermal conductivity in the range of 0.01 - 0.02 W/m.K, as a result of a well balanced relationship between low solid conductivity, low gaseous conductivity and low radiation infrared transmission. This balanced relationship between the different heat transfer modes is difficult to achieve because each heat transfer mode is firmly linked to the other [17]. Various glass systems based on the aerogel

layer were measured and evaluated [18]. Comparison of transmission coefficient of aerogel pane is shown in Figures 7, 8.

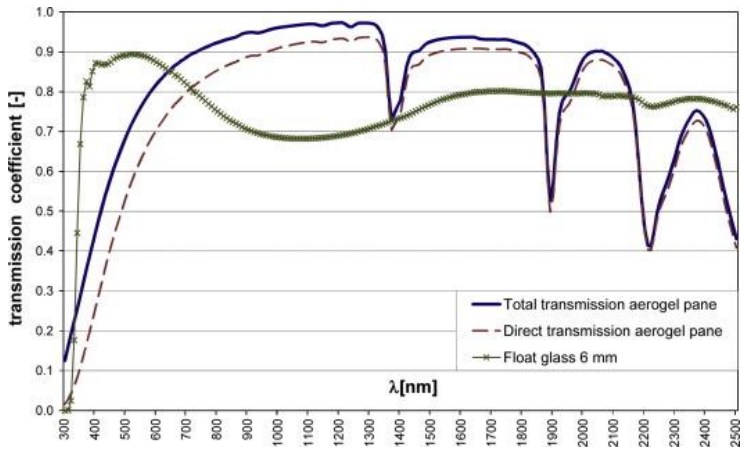

Figure 7: Comparison of solar spectral transmission of aerogel and float glass pane [19].

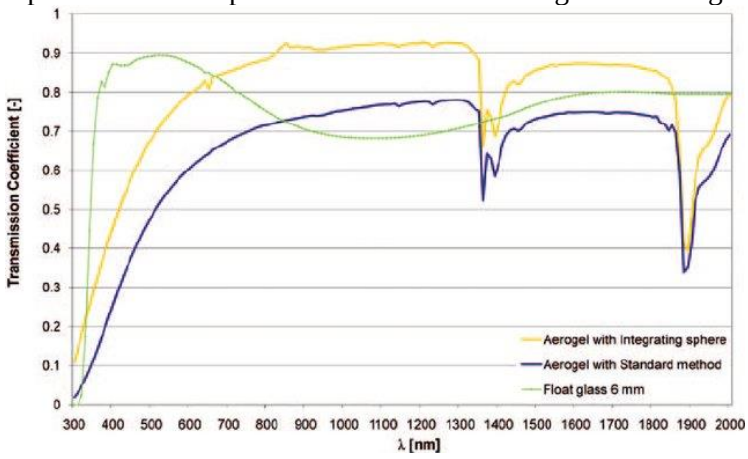

Figure 8: Transmission coefficient vs. wavelength of pane aerogel measured without the integrating sphere (standard method) and with the integrating sphere compared to a 6 mm float glass [18].

2.5 Thermochromic glazing

Thermochromic glass simply uses the heat of direct sunlight to color the windows as needed. The more direct and intense the sunlight, the darker it will be on the glass. This allows windows to significantly reduce the thermal load coming into the building, and because the glass permeability constantly adjusts over the temperature range, a natural balance and maximum use of daylight is achieved.

Thermochromic windows consist of a common safety interlayer which is produced by extruding special thermochromic materials into polyvinylbutyral (PVB), laminated between two pieces of heat-strengthened or tempered glass and placed in an insulated glass unit (IGU) with a low emissivity coating.

Figure 9 presents the normal-hemispherical transmittance measurements of a thermochromic complex based on a lactone dye. A significant decrease in transmittance can be observed with increasing temperature. The decrease in transmittance is due to a significant increase in absorption and is effective in the visible range of solar radiation. This is not associated with increased reflection of incident solar radiation. The effect of molecular switching between different structures cannot contribute to the reflection control. The reduction of the transmittance in the visible wavelength range of 27% is only accompanied by a 6% reduction in solar transmittance [20].

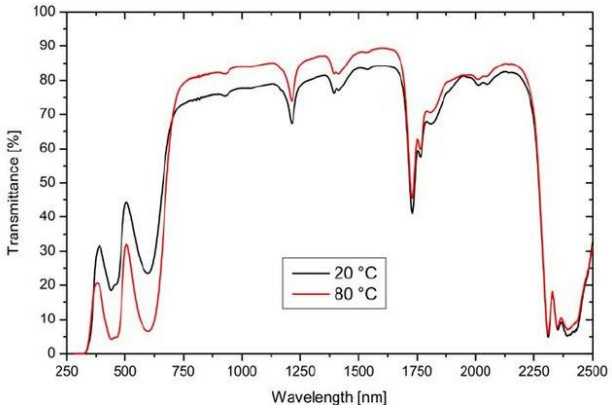

Figure 9: Normal-hemispherical transmittance of a thermochromic film with a green dye at different temperatures [21].

2.6 Electrochromic glazing

The unit consists of ceramic metal oxide coatings with three electrochromic layers sandwiched between two transparent electrical conductors. When a voltage is applied between the transparent electrical conductors, a distributed electrical field is set up. This field moves various coloration ions (most commonly lithium or hydrogen) reversibly between the ion storage film through the ion conductor (electrolyte) and into the electrochromic film.

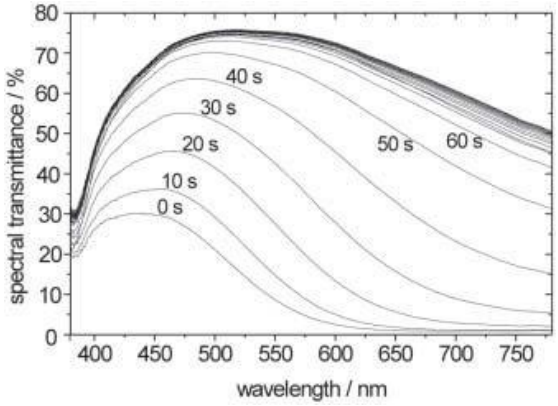

Figure 10: Change of the transmittance of an electrochromic glass with ion conducting PVB interlayer between 380 and 780 nm during bleaching [22].

Typical electrochromic windows have an upper visible transmittance range of 0.50–0.70 and a lower range of 0.02–0.25 (see Fig. 10). The g-factor (total solar energy transmittance) ranges

from 0.10-0.50. A low transmission is desirable for privacy during the day and for control of direct sun and glare, potentially eliminating the need for interior shading. A high transmission is desirable for admitting daylight during the time of the day that the sun is not shining directly into the space, during overcast periods and for passive solar heating in winter.

2.7 Suspended particle device

This electrically controlled film utilizes a thin, liquid-like layer in which numerous microscopic particles are suspended. In its unpowered state the particles are randomly oriented and partially block sunlight transmission and view. Transparent electrical conductors allow an electric field to be applied to the dispersed particle film, aligning the particles and raising the transmittance. Typical visible transmittance and total solar energy transmittance ranges for the film alone are τ_V = 0.22 – 0.005 or 0.57 – 0.12 and g = 0.56 – 0.41 or 0.70 – 0.50, respectively, with near instant switching times (less than one second), see Figure 11. The SHGC switching range is more limited than electrochromic windows.

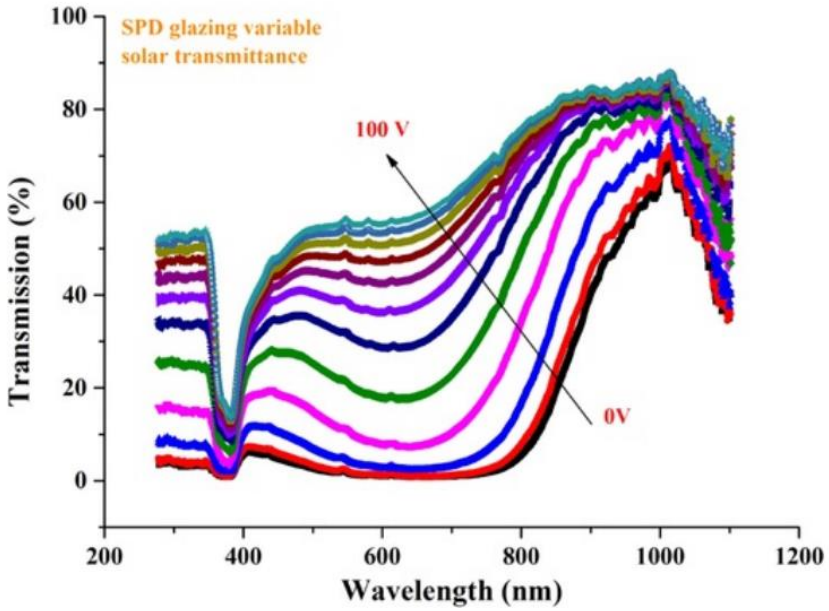

Figure 11: Solar transmittance for SPD glazing after exposure at variable voltage [23].

2.8 Liquid crystal

A very thin layer of liquid crystal is sandwiched between two transparent electrical conductors on thin plastic films, and the entire emulsion or PDLC or polymer dispersed liquid crystal device, is laminated between two layers of glass. When the power is turned off, the liquid crystals are in a random and unaligned state. They scatter light and glass appears as a translucent layer that obscures direct view and provides privacy. The material transmits most of the incident solar radiation in the diffuse mode so that its heat gain coefficient of solar energy remains high. When energy is applied, the electrical field in the device aligns the liquid crystals and the glazing becomes transparent in a fraction of a second, allowing viewing in both directions. Most such devices have only two states, clear and diffuse, and the

power (about 0.5 W, operation between 24 and 100V AC) must be continuously applied to keep the glazing clear. The visible transmittance range is typically 50-80% and the total solar energy transmittance (g-factor) is 0.55-0.69 [24], see Figure 12.

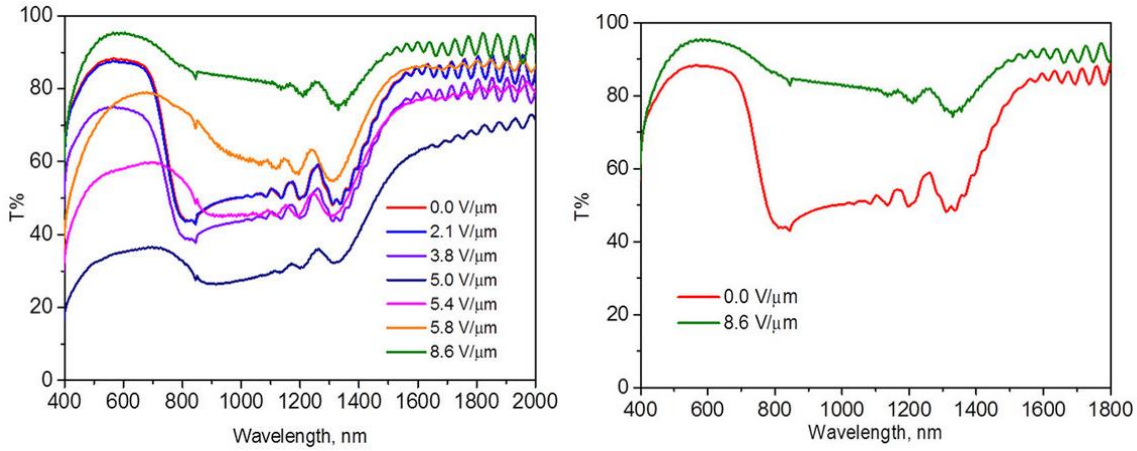

Figure 12: Transmission spectrum. a) The IR reflector on varying the applied voltage from 0 V/µm to 8.6 V/µm b) Transmission spectrum of cholesteric gel in reflective and transmissive states at 0 V/µm and 8.6 V/µm [25]

3 Idea base of ideal glazing

The idea of an ideal glass system arises from the current state of the issue of fenestration and the development of various directions as well as in construction or material range. A structurally oriented direction is an increase in the number of glasses in the glass system, which, even for float glass, represents a significant improvement in the thermal properties of the glass system. The disadvantage of this idea is the high weight increase of the structure, which is associated with additional transport and assembly problems as well as the need for more robust and stronger fittings. The high weight of the system thus implies a certain dimensional limitation in the case of opening structures. In the case of fully glazed facades this problem disappears and ventilation is solved by smaller window segments, or natural ventilation is fully replaced by controlled ventilation. An improvement in the heat transfer coefficient is thus possible to approximately 0.7 W/(m^2.K), and if low-emissivity coatings were used, this improvement would be even more noticeable. The g-value of multi-insulating glass systems is in the range of 0.87 - 0.54 and the visible transmittance in the range of 0.99 - 0.57. These thermal and optical properties are mainly due to the number of glasses in the glass system, the gas filling used has almost no effect on it. In the case of glass systems using low-emissivity coatings or separate films, these values are significantly lower due to the emissivity of the film used. There are several types of films on the market that can be applied to the glass system according to its future location (cardinal orientation). The films are customized for specific orientation according to the climate and desired heat gains or unwanted heat losses respectively. In addition to low-emissivity coatings and films, other materials and technologies are used to improve thermal insulation properties. Water is a suitable absorbent of near infrared and ultraviolet radiation while maintaining excellent transmission of the visible part of spectrum. Aerogel is a progressive to a certain thickness transparent thermal insulator based on nanoparticles of various sizes. Thermochromic and electrochromic glazing

based on materials changing the structure of their structure when a certain temperature is reached or a voltage is applied into the glass system. On the principle of the voltage application functioning liquid crystals and SPD systems, together with the electro and thermochromic ones, the idea of an autonomous adaptive glass system, which regulates heat losses and gains according to current needs (see Fig. 13), has been approached so far.

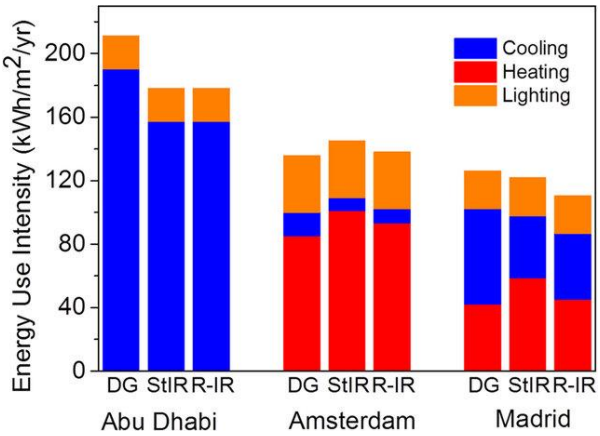

Figure 13: Comparison of annual energy use for a normal double glazed window, static IR reflector and the switchable (responsive) infrared reflector for three different climates [25].

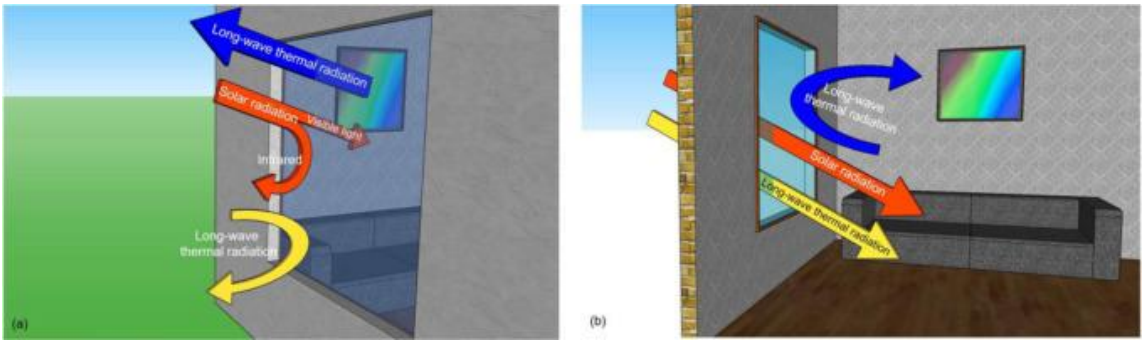

Figure 14: Model of operation of the ideal glass system. a) Summer situation. b) Winter situation [26].

An ideal fully autonomous glass system should reflect the climate conditions in which it is installed, including customization within the cardinal points. In a hot climate, a glass system that reflects all infrared radiation (from the sun and surrounding surfaces) as well as all UV radiation is suitable. At the same time, it is able to transmit all infrared radiation from the interior to the exterior and at the same time maintain the transparency and allow the visible component of light to penetrate. In cold climates, it would be able to transmit radiation of all wavelengths except UV into the interior while reflecting all infrared radiation is backed to the interior [26], see Figure 14. So far, the glass system has to reach minimum parameters depending on the climate, see Table 2.

Table 2: Required parameters of the glass system for a specific climate [27]

Climate	τ_V	SHGC (g)	U (W/(m^2.K)
Cool climate (prevailing heating loads)	> 0.70	> 0.60	< 2
Temperate climate (prevailing heating loads)	> 0.70	> 0.50	< 2.5
Hot climate (prevailing cooling loads)	> 0.60	< 0.40	< 4

4 Conclusion

Increasing the thermal insulation properties of glass systems was one of the first tools to achieve the goal of eliminating the window structure as a thermal bridge in the building envelope. Gradually, however, more emphasis has also been placed on the other thermal-optical parameters of the glass system, which have become a tool to reduce the need for heating and cooling energy due to heat losses in winter and gains in summer. The next step is to create the concept of an adaptive glass system whose properties will vary depending on the immediate environmental conditions in relation to indoor thermal comfort. Its concept is customized for a specific climate and orientation towards cardinal points. An adaptable glass system capable of operation should be able to regulate its properties while maintaining a high level of transparency, which is currently a major disadvantage of other adaptive glass systems on the principle of power supply or reaching a temperature limit.

Acknowledgements

This paper was created and realized with support of research project VEGA 1/0389/17 “Transparent construction in interaction of the contemporary architecture and on the human health”.

References

[1] Chmúrny, I. (2016) Triple or Quadruple Glazing? Applied Mechanics and Materials. Trans Tech Publications, Switzerland. Vol. 820, pp 242-247.

[2] Chmúrny, I. (2014) Ultra Thin Glass Membranes for Advanced Glazing of nZEB. Advanced Materials Research. Trans Tech Publications, Switzerland. Vol. 899, pp 470-473.

[3] Tükel, M. et al. (2019) Analysis of fluid flow and heat transfer characteristics in multiple glazing roofs with a special emphasis on the thermal performance. Applied Thermal Engineering. Vol. 148, pp 694-703.

[4] Kralj, A. et al. (2019) Investigations of 6-pane glazing: Properties and possibilities. Energy and Buildings. Vol. 190, pp 61-68.

[5] STN EN 1279-6 (2019) Glass in building - Insulating glass units - Part 6: Factory production control and periodic tests.

[6] Alghamedi, R. et al. (2014) Spectrally-selective all-inorganic scattering luminophores for solar energy-harvesting clear glass windows. Scientific Reports 4.

[7] European Standard CEN EN 410 (2013) Glass in Building—Determination of Luminous and Solar Characteristics of Glazing.

[8] Jelle, B. P. (2013) Solar radiation glazing factors for window panes, glass structures and electrochromic windows in buildings—Measurement and calculation. Solar Energy Materials and Solar Cells. Vol. 116, pp 291-323.

[9] Window 7.4.14. (2017) NFRC Simulation manual. Lawrence Berkley laboratory.

[10] Arici, M. et al. (2015). Flow and heat transfer in double, triple and quadruple pane windows. Energy and Buildings. Vol. 86, pp 394-402.

[11] Efficient Windows Collaborative. Windows for high-performance commercial buildings. Available on site: https://www.commercialwindows.org/transmittance.php.

[12] Miyazaki, M. et al. (1994) Durability improvement of Ag-based low-emissivity coatings. Journal of Non-Crystalline Solids. Vol. 178, pp 245-249.

[13] Abundiz-Cisneros, N. et al. (2020) Novel Low-E filter for architectural glass pane. Energy and Buildings. Vol. 206, 109558.

[14] Konis. K. et al. (2017) Innovative Daylighting Systems. Green Energy and Technology. In book: Effective Daylighting with High-Performance Facades.

[15] Saidur, R. et al. (2012) Evaluation of the Effectof Nanofluid-Based Absorbers on Direct Solar Collector. International Journal of Heat and Mass Transfer. Vol. 55, Issues 21–22, pp 5899-5907.

[16] Ai, Q. et al. (2017) Near Infrared Spectral Radiation Properties of Different Liquid Hydrocarbon Fuels. Journal of Near Infrared Spectroscopy 26(1):096703351774437.

[17] Baetens, R. et al. (2011) Aerogel insulation for building applications: A state–of–the–art review, Energy and Buildings. Vol. 43, pp 761–769.

[18] Buratti, C. et al. (2011) Lighting and Energetic Characteristics of Transparent Insulating Materials: Experimental Data and Calculation. Indoor and Built Environment 20(4), pp 400-411.

[19] Buratti, C. et al. (2012) Experimental performance evaluation of aerogel glazing systems. Applied Energy. Vol. 97, pp 430-437.

[20] Seeboth, A. et al. (2010) Thermotropic and Thermochromic Polymer Based Materials for Adaptive Solar Control. Materials (Basel); 3(12), pp 5143-5168.

[21] Ruhmann, R. et al. (2008) Development of Thermochromic Polymer Films for the Sun Protection in Buildings. Final report to the German Federal Ministry of Economics and Technology: Bonn, Germany.

[22] Stenzel, H. et al. (2003) Electrochromic Glazing with an Ion-Conducting PVB Interlayer. Conference: GPD Glass Processing Days 2003. Tampere, Finland. Vol.: Conference Proceedings Book, pp 423-426.

[23] Ghosh, A. et al. (2017) Durability of switching behavior after outdoor exposure for a suspended particle device switchable glazing. Solar Energy Materials and Solar Cells, Vol. 163, pp. 178-184.

[24] Dakheel, J. A. et al. (2017) Building Applications, Opportunities and Challenges of Active Shading Systems: A State-of-the-Art Review. Energies 10(10):1672.

[25] Khandelwal, H. et al. (2015) Electrically switchable polymer stabilized broadband infrared reflectors and their potential as smart windows for energy saving in buildings. Scientific Reports 5:11773.

[26] Long, L. et al. (2014) How To Be Smart and Energy Efficient: a General Discussion on Thermochromic Windows. Scientific Reports 4 :6427.

[27] Piccolo, A. et al. (2015) Performance Requirements for Electrochromic Smart Window. Journal of Building Engineering. Vol. 3, pp 94-103.

DOI: 10.1515/sspjce-2019-0024

Research of building structures in extreme climate conditions

Dušan Katunský, Lenka Kabošová, Erika Dolníková, Marek Zozulák

Technical University of Košice, Slovakia
Faculty of Civil Engineering, Institute of Architectural Engineering
e-mail: dusan.katunsky@tuke.sk

Abstract

The paper provides information on the solution of project supported by the Scientific Grant Agency of VEGA of the Ministry of Education, Science, Research and Sports of Slovak Republic and of the Slovak Academy of Sciences of Slovak Republic. There is project: VEGA 1/0674/18. This research project is programmed for the years 2018 to 2021. In this paper are presented information on the results obtained in 2019, solution of this project objectives and project solution. The results are presented in realized publications. We focused mainly on the presentation of major publications, articles in domestic and foreign journals, articles in conference proceedings with an emphasis on publications that are indexed in the WOS and SCOPUS databases.

Key words: building structures, architecture, envelope structures, thermo-moisture properties, light-technical properties, constructional-architectural shapes,

1 Introduction

The content of the project is theoretical analysis and experimental research of architectural-structural shapes of buildings, fragments and details of building envelope, their physical properties, i.e. (aerodynamic, thermal, humidity, energy) as well as material parameters, their packaging structures designed for extreme external climate conditions (wind, snow, rain, temperature differences). The research is carried out under real conditions (in situ) and laboratory research in the construction of experimental models. The project builds on the results obtained so far. In real terms, the effects of wind, temperature, external climate humidity, as well as energy flows through cladding are characterized by non-stationary processes. The task of the project is therefore to analyze these impacts, in particular the aerodynamic, thermal, humidity and energy impacts on the building as a whole, as well as these effects on the packaging structures, exposed to extreme external climate conditions (both experimental and real in situ measurements).

2 Content of the project and research

The project aims to meet three basic objectives:

I. The first objective is laboratory measurements and calculations of selected aerodynamic parameters of building envelope structures, architectural and structural shapes of buildings that determine the behavior of building structures and the building as a whole under extreme wind conditions.

II. The second objective is to monitor selected parameters (physical quantities) of fragments and details of cladding (temperature and humidity changes).
   a) exposed to laboratory conditions (indoor stand),
   b) exposed to real conditions (experimental chambers).
   c) exposed to real conditions in situ (on site, in a building).

III. The third objective is laboratory measurements of physical parameters of building materials that are exposed to extreme conditions in building envelope structures. Inputs: Experience gained on the basis of long - term measurements of material and physical characteristics of fragments and construction details in real conditions of exploitation of the construction work - in situ, further knowledge from research in the given area (projects solved so far).

IV. General conclusions outputs:
   a) Models of architectural and structural shapes of buildings,
   b) Packaging structures, e. j. building fragments in extreme external climate conditions as a reliable tool for optimizing the structural detail of a building.
   c) Parameters (physical quantities) – verification model for numerical simulations.

Table 1: Description of the content of the members of the team to solve the project in. 2019/2020

č	Team		
	name	**position**	**function**
1	Katunský Dušan, prof. Ing. CSc.	professor	project leader
2	Vertaľ Marián, doc. Ing. PhD	assoc-prof	deputy head, hygro-thermal properties
3	Lopušniak Martin, doc. Ing. PhD	assoc-prof	coordination between projects
4	Bullová Iveta, Ing. PhD	assist prof.	aerodynamic properties
5	Dolníková Erika, Ing. PhD	assist prof.	light-technical properties
6	Katunská Jana, Ing. PhD	assist prof.	thermal and energy properties
7	Tóth Stanislav, Ing. PhD	assist prof.	packaging constructions
8	Zozulák Marek, Ing. PhD	assist prof.	thermo-moisture properties, laboratory research
9	Szénay Martin, Ing. PhD.	PhD-studet	fire lifts (completed PhD in August 2019)
10	Kabošová Lenka, Ing. arch.	PhD-studet	structural and architectural shapes of buildings
11	Špaková Miroslava, Ing. (MD)	PhD-studet	research of wood structures
12	Karľa Viktor, Ing. arch.	PhD-studet	transparent wood, static properties
13	Jaroš Pavol, Ing.	PhD-studet	hygro-thermic properties of sandstone
14	Tomková Želmíra, Ing. arch.	PhD-studet	LCA (life cycle assessment)
15	Baroš Tomáš, Ing.	PhD-studet	parazitic architekture

The project is solved by a team consisting of colleagues from the Institute, members are one professor, two associate professors, five lecturers and seven doctoral students, which together

make 15 researchers. Each member of the team has its own role and content, which is devoted to.
Methods: Theoretical analysis, synthesis, confrontation, simulation, experiment. In experimental facilities realization of measurements on test models using monitoring elements in cooperation with a device for monitoring changes of conditions of demanding external climate:

a) Calculations, simulations, mathematical modeling, obtaining boundary conditions,
b) Production of models of architectural and structural shapes of buildings, fragments,
c) Measurements, data analysis, confrontation of measurements and calculations.

3 Project results

The project was solved in the previous year by the team, which is shown in Table 1. Individual researchers published their results in journals, proceedings and presented at conferences. Individual publications touched on the main points, which are the basic objectives and subjects of observation:

1) Designs of structural and architectural shapes
2) Aerodynamic properties
3) Lighting properties
4) Energy assessment of buildings
5) Heat-moisture properties
6) Properties of materials, sandstone, transparent wood
7) LCA method

Individual points are filled with publications in which it is stated what has been achieved. The following points can be mentioned for individual points:

3.1 Design of structural and architectural shapes

Ing. arch. Lenka Kabošová was most active doctoral student at this point [1], [2]. She deals with extreme wind influence on the creation of architectural and structural shapes of buildings in dissertation thesis. She has prepared a number of publications that have been published or are ready for publication in journals and proceedings under the guidance of a specialist consultant Professor Kmeť. In 2019 these were the following publications:

1) Digitally Designed Airport Terminal Using Wind Performance Analysis / Kabosova, Kmet, Katunsky – 2019, In: Buildings (CH)
2) Hybrid Design Method for Wind-Adaptive Architecture / Kabosova [et al.] – 2019, In: International Journal of Architectural Computing – SAGE Publications London (GB)
3) Building Envelope Adapting from / to the Wind Flow / Kabosova [et al.] – 2019, In: Architecture in the Age of 4th Industrial Revolution Volume 2 Education and Research in Computer Aided Architectural Design in Europe – Porto (PT)
4) The interactions of wind and architectural shape / Kabosova – 2019, In: Seminar of PhD students 2019: in field: PS – TUKE Košice (SK)

5) The search for an optimal architectural shape using wind performance analysis / Kabosova – 2019, In: YS2019 – Young Scientist 2019: Proceedings of the 11th International Scientific Conference on Civil and Environmental Engineering for PhD. Students and Young Scientists – IOP Publishing, Bristol (GB)

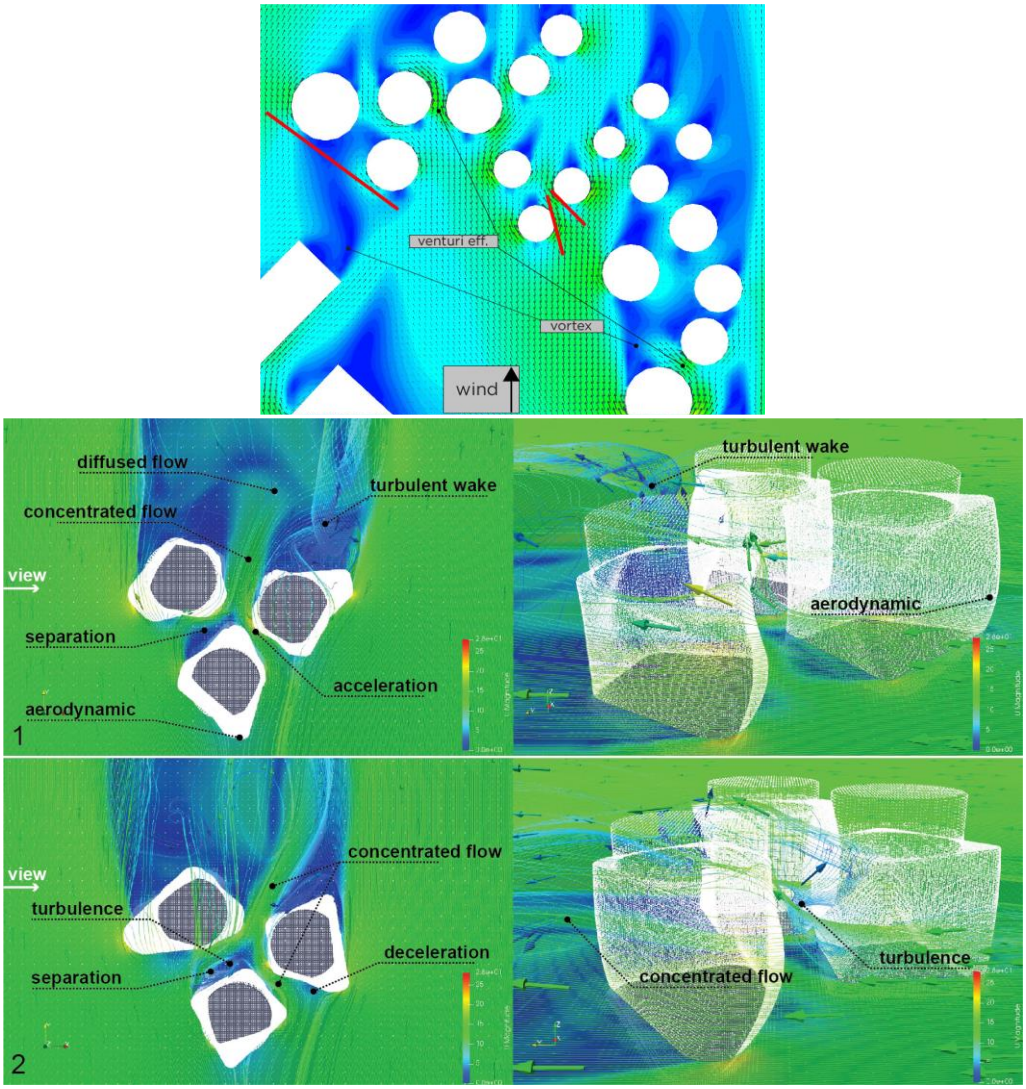

Figure 1: Southern wind in Loudden docks (focus area is in circle) - two shape modifications, FlowBrane (author: L. Kabosova)

3.2 Aerodynamic properties

Aerodynamic properties also fill the first point, which is briefly described.
The influence of air flow as well as the effect of air exchange in the interiors of buildings was the responsibility of Ing. Bullová, who published in 2019 on this research point:

1) Impact of air permeability in selected reference room / Bullová – 2019, In: Design of energy efficient buildings 2019: Proceedings of Scientific Papers. – TUKE Košice (SK):

3.3 Lighting properties

The impact of light on the working environment was addressed by Ing. Erika Dolnikova, PhD., [3], [4], [5]. In 2019, several publications were published:

1) Evaluation of Daylighting in Selected Office Rooom: Case Study / Dolníková – 2019, In: SSP – Journal of Civil Engineering, TUKE, Kosice (SK)
2) Visual Assessment in Industrial Environment: A Case Study / Dolníková, Katunský – 2019, In: Environments (CH)
3) Assessment of Daylight in a Selected Office through Simulation Programs: A case study / Dolníková – 2019, In: e-GFOS: Electronic Journal of the Faculty of Civil Engineering Osijek (HR)
4) Visual Comfort Assistant in the Office: A Case Study / Dolnikova, Katunsky – 2019, In: SGEM 2019 conference proceedings, Nano, Bio and Green – Technologies for a Sustainable Future: Green Buildings Technologies and Materials, Green Design and Sustainable Architecture, Space Technologies and Planetary Science. – Sofia (BG)
5) Assessment of Working Environment in Terms of Visual Perception / Katunský, Dolníková – 2020, In: Proceedings of CEE 2019, Cham, Springer, (CH)

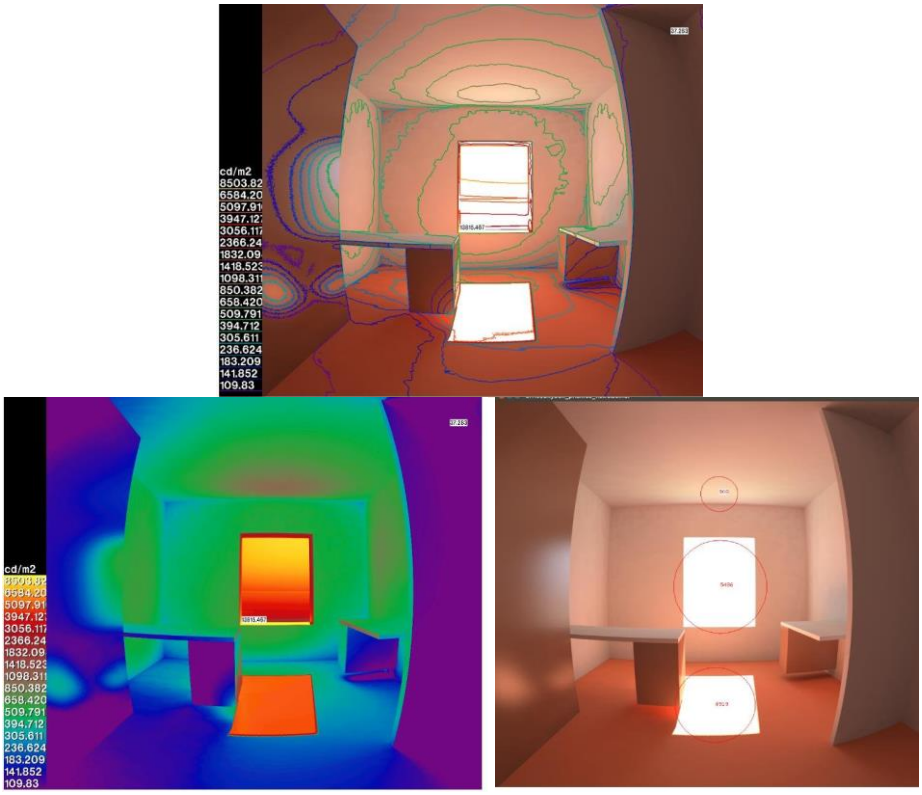

Figure 2: Evaluation of luminous intensity, potential glare (dazzling eyes) by Radiance program (author: E. Dolníková)

3.4 Energy assessment of buildings

Published contributions resulted from the solution of the previous grant, which was followed by this project [6]. In 2019 the following publications were concerned:

1) The Impact of Various Factors on the Energy Efficiency of Selected Types of Family Houses / Katunský, Farárik – 2019, In: Proceedings of the 12th International EnviBUILD Conference, Bratislava (SK)
2) Comparison of Energy Efficiency Properties of Individual Houses / Katunský, Farárik – 2019, In: Proceedings of SGEM 2019. 2.6 Nano, Bio and Green – Technologies for Sustainable Future: Technologies and Materials for Green Buildings, Eco–Design and Sustainable Architecture, space technology and planetary science. – Sofia (BG)

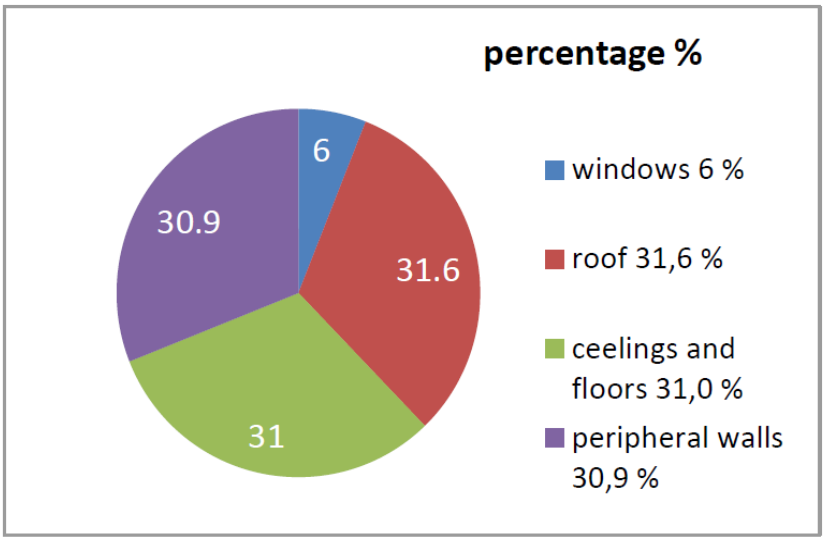

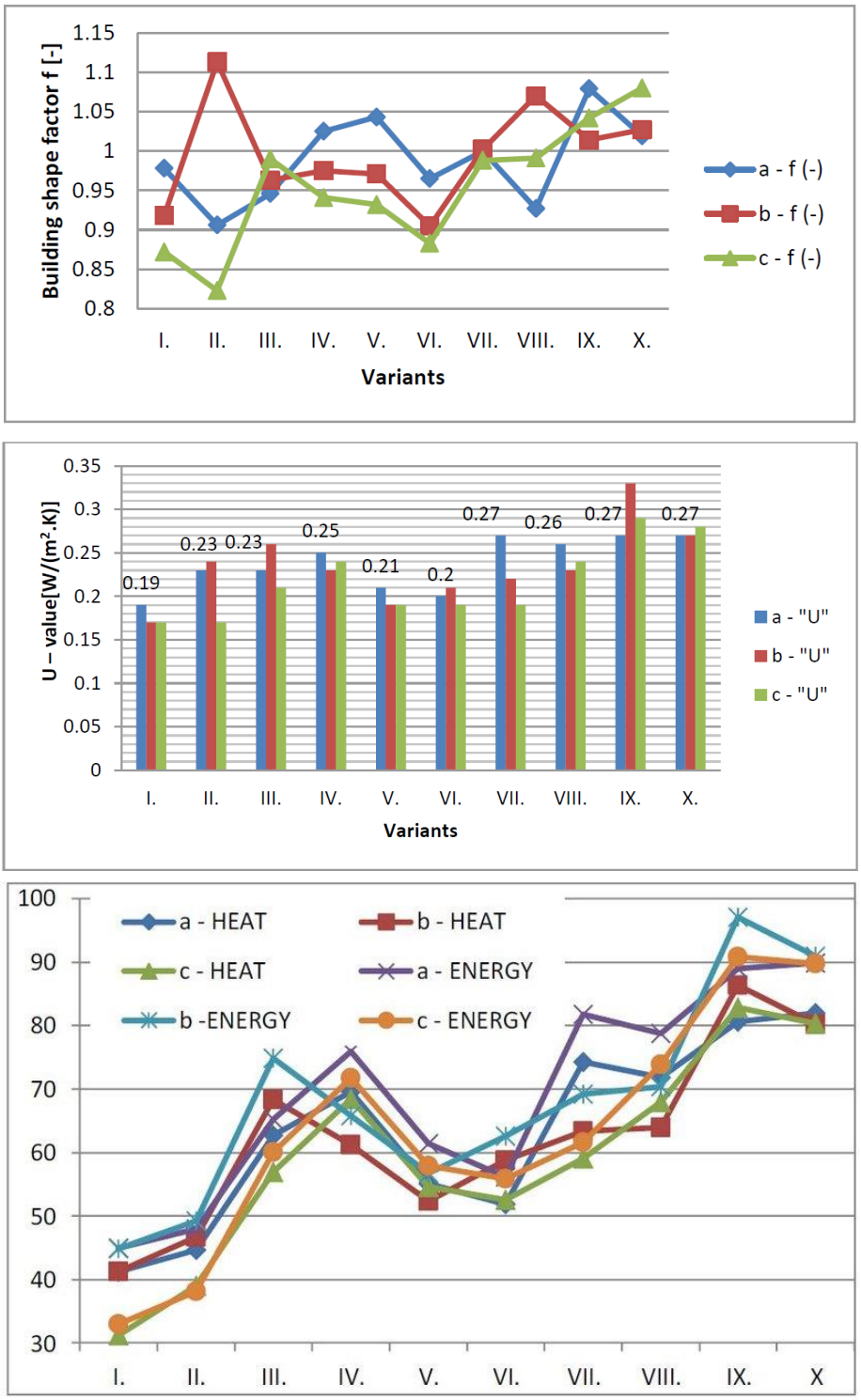

Figure 3: Assessment of heating demand (HEAT) and heating energy (ENERGY) kWh/(m^{2}a.), Part of heat losses in individual parts of single-store houses according to Katunský/Farárik

3.5 Heat-moisture properties

The evaluation of thermal-moisture properties was carried out by several researchers [7], [8], [9], but mainly by Ing. Marek Zozulak, PhD, [10]. In 2019 these were the publications:

1) Simulation of window connection joint using ham model and temperature field model / Zozulák, Katunský – 2019, In: Thermal Protection of Buildings 2019: Designing of Building Structures and Buildings: Proceedings of 20th International Conference. - Bratislava (SK)
2) The influence of the initial condition in the transient thermal field simulation inside / wall / Zozulák, Vertaľ, Katunský – 2019, In: Buildings, (CH)
3) Selected Problems of Thermal Insulation of Historical Buildings / Katunská, Katunský, Labovská – 2019, in Selected Scientific Papers / Journal of Civil Engineering (SK)

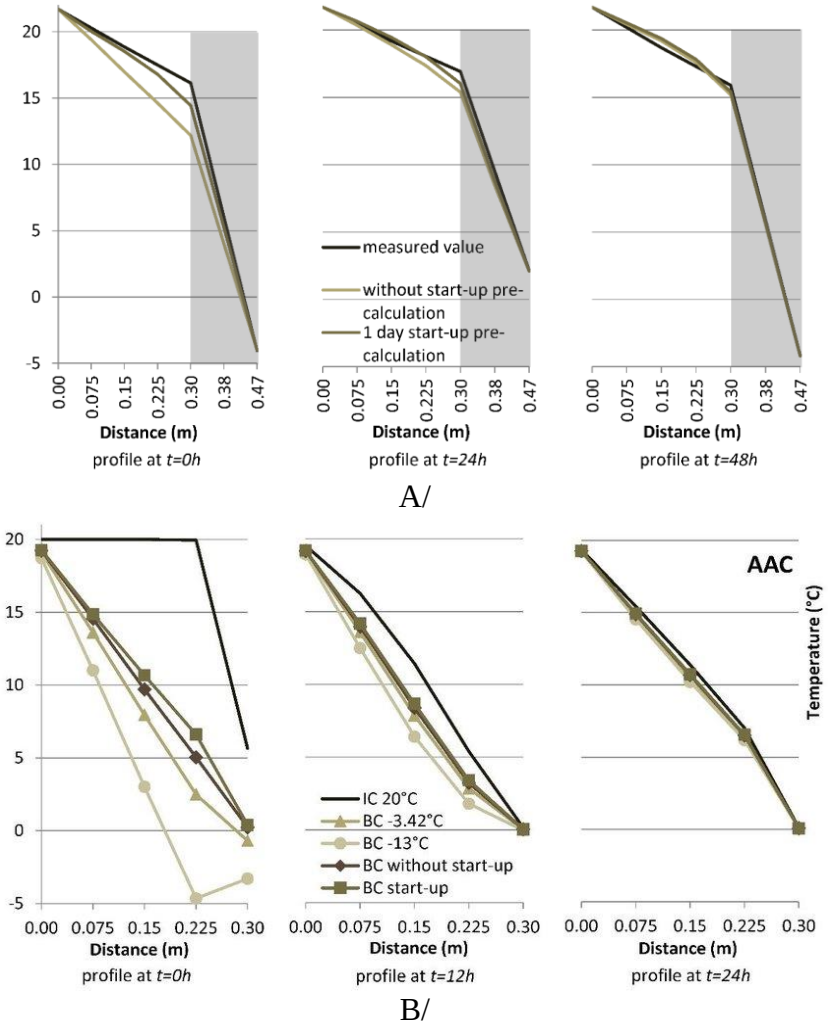

Figure 5: A / Temperature profile across the cell wall at t = 0, 24 and 48 h, with and without preliminary calculations
B / Temperature profile through a single AAC test wall at t = 0 h, t = 12 h and = 24 h for five cases under initial conditions (author M. Zozulák)

3.6 Properties of materials, sandstone, transparent wood

Material properties, especially transparent wood and sandstone, were studied by PhD students Ing. arch. Viktor Karľa [11], and Ing. Pavol Jaroš. In 2019 these were the following publications:

1) Structural elements of transparent wood in architecture / Karľa – 2019, In: PhD student seminar 2019: in the field: Building construction – Košice (SK)
2) Update on Research on Transparent Wood / Karla – 2019, In: YS2019 – Young Scientist 2019: Proceedings of the 11th International Scientific Conference on Civil and Environmental Engineering for PhD. Students and Young Scientists – Bristol (GB)
3) Sandstone as Building Material in Eastern Slovakia / Jaroš, Vertaľ – 2019, In: PhD Seminar 2019: in the field: PS – TUKE Košice (SK)
4) Water transport in historical buildings / Jaroš, Vertaľ 2019, In: YS2019 – Young Scientist 2019: proceedings of the 11th International Scientific Conference on Civil and Environmental Engineering for PhD. Students and Young Scientists, IOP Publishing – Bristol (GB)

3.7 LCA method

Life Cycle Assessment was solved in 2019 besides previous topics. Associated professor Vilčeková from the Institute of Environmental Engineering was as the tutor for doctoral student Ing. arch Tomková. They published together some articles:

1) Analysis of the life cycle of family houses in terms of sustainability in construction / Moňoková, Vilčeková, Tomková – 2019, In: Sustainability and digitization in construction – TUKE Košice (SK)
2) Primary and recycled materials from the perspective of LCA analysis / Tomková, Moňoková, Vilčeková – 2019, In: Cassotherm 2019: Non–Conference Proceedings of Scientific Papers. – TUKE Košice (SK)
3) Analysis of the current situation in the field of LCA / Tomková, Vilčeková – 2019, In: YS2019 – Young Scientist 2019: Proceedings of the 11th International Scientific Conference on Civil and Environmental Engineering for PhD. Students and Young Scientists – IOP Publishing Bristol (GB)
4) Analysis of the current situation in LCA (Life Cycle Assesment) / Tomková – 2019, In: PhD Seminar 2019: in field: PS – TUKE Košice (SK)
5) Primary and Recycled Materials from LCA Analysis / Tomková, Moňoková, and Vilčeková – 2019, In: Indoor Climate of Buildings 2019: Energy Management for a better Indoor Environment – Slovak Society for Environmental Engineering Bratislava (SK)

4 Conclusion

The paper presents the results of the previous research project VEGA 1/0674/18 "Theoretical and Experimental Analysis of Architectural and Structural Shapes and Fragments of Building Structures for Demanding Climate Conditions", which is planned for 2018–2021. Especially to the change of the research team, this also influenced the overall work on individual tasks.

With regard to the staffing of the researchers and the acceptance of new PhD students, some of the objectives and / or methodology were modified so that the status of the solution could be realistic. As it was presented, most of the activities were carried out in areas where the researchers are specialized or professionally oriented [12]. The main task is to solve constructional details of buildings from the point of view of physical aspects under difficult conditions. This can be seen in the outputs of the second year of the solution. It was the effect of difficult conditions, whether it affected the effect of wind, temperature differences, but also the effect of sun rays, glare, etc.

Acknowledgements

The paper presents partial research results of project VEGA 1/0674/18

References

[1] Kabošová, L., Foged, I., Kmeť, S., & Katunský, D. (2019). Hybrid design method for wind-adaptive architecture. *International Journal of Architectural Computing, 17*(4), 307-322.

[2] Kabošová, L., Kmeť, S., & Katunský, D. (2019). Digitally designed airport terminal using wind performance analysis. *Buildings*, 9(3), 59.

[3] Dolnikova, E., & Katunsky, D. (2019). Visual Comfort Assessment in an Industrial Environment: A Case Study. *Environments*, 6(5), 54

[4] Dolnikova, E. (2019). Assessment of Daylight in the Selected Office through Simulation Programs: a case study. *e-Gfos*, 10(18), 82-92.

[5] Katunsky, D., & Dolnikova, E. (2019), Assessment of the Working Environment in Terms of Visual Perception. In *International Conference Current Issues of Civil and Environmental Engineering Lviv–Košice–Rzeszów* (pp. 145-152). Springer, Cham

[6] Katunský, D. & Farárik, M. (2019), The Impact of Various Factors on the Energy Performance of Selected Types of Family Houses. In: *Applied Mechanics and Materials* (Vol. 887, pp. 109-116). Trans Tech Publications

[7] Tudiwer, D., Vertal', M., Korjenic, A., & Čakyová, K. (2019), Abbildung der Wärmedämmenden Wirkung eines Fassadengebundenen Begrünungssystems in einem Simulationsmodell, *Bauphysik*, 41(3), 155-161.

[8] Richard Baláž, R. & Tóth, S. (2019) Green roofs and its measurement in: *Advances and Trends in Engieneering Sciences and Technologies III.*, Londýn (Veľká Británia): CRC Press, s. 293-298

[9] Katunská, J., Katunský, D., & Labovská, V. (2019), Selected problems of thermal insulation of historical buildings. *Selected Scientific Papers-Journal of Civil Engineering*, 14 (1), 67-74.

[10] Zozulák, M., Vertaľ, M., & Katunský, D. (2019), The Influence of the Initial Condition in the Transient Thermal Field Simulation Inside a Wall, *Buildings*, 9 (8), 178.

[11] Karl'a, V. (2019, June). Update on Research on Transparent Wood. In *IOP Conference Series*: Materials Science and Engineering (Vol. 566, No. 1, p. 012015). IOP Publishing.

[12] Katunský, D. (2020), Výskum budov v náročných klimatických podmienkach a výskum priamej zložky D.O. v architektonickom a interiérovom prostredí budov (súčasný stav riešenia). In: 12. ročník Seminár doktorandov ÚPS Zborník príspevkov ISBN 978-80-553-3519-3 (Vol. 12, pp. 53-60). TUKE Košice